UNIVERSITA' DEGLI STUDI DI MESSINA

Dipartimento di Scienze Chimiche, Biologiche, Farmaceutiche ed Ambientali
Dottorato di Ricerca in Scienze Chimiche
Curriculum Progettazione, sintesi, analisi e proprietà di sistemi molecolari funzionali

---

Noble metal nanoparticles as active materials for solar energy conversion and chemical sensing

Sara GULLACE

Supervisor:

Dott. Giuseppe CALOGERO

Co-Tutor:

Prof. Paolo SAMORI'

XXXIII ciclo (2017-2020)

Table of contents

List of figures

List of abbreviations

NP	Nanoparticles
PLD	Pulsed laser deposition
DSSC	Dye-sensitized solar cell
PCE	Power conversion efficiency
PE	Photoelectrode
CE	Counter electrode
TCO	Transparent conductive oxide
ITO	Indium tin oxide
FTO	Fluorine-doped tin oxide
HOMO	Highest occupied molecular orbital
LUMO	Lowest unoccupied molecular orbital
N3	*cis*-bis(isothiocyanato)bis(2,2'-bipyridyl-4,4'-dicarboxylato ruthenium(II)
N719	Di-tetrabutylammonium-*cis*-bis(isothiocyanato)bis(2,2'-bipyridyl-4,4'-dicarboxylato)ruthenium(II)
Z907	cis-Bis(isothiocyanato)(2,2'-bipyridyl-4,4'-dicarboxylato)(4,4'-di-nonyl-2'-bipyridyl)ruthenium(II)
FoM	Figure of merit
Jsc	Short-circuit current
Voc	Open circuit voltage
FF	Fill factor
η (PCE)	solar-to-electric power conversion efficiency
PV	photovoltaic
EQE	external quantum efficiency
IPCE	incident photon conversion efficiency
λ	wavelength
HTM	Hole transporting material
ICT	Internal charge transfer
D-π-A	Donor-π bridge-Acceptor
CB	Conduction band
ACN	acetonitrile
VN	valeronitrile
MPN	3-methoxypropionitrile
TBP	4-*tert*-butylpyridine
CVD	Chemical vapour deposition
GR	graphene
PEDOT	poly(3,4-propylenedioxythiophene)
LH	Light harvesting

E_g	Energy band gap
μ_e	Electron mobility
LASiS	Laser ablation synthesis in solution
SDS	sodium dodecyl sulfate
PLD or PLA	Pulsed laser deposition or ablation
LSP	Localized surface plasmon
LSPR	Localized surface plasmon resonance
EM	electromagnetic
E	Dielectric function
SERS	Surface enhanced Raman spectroscopy
CM	chemical
LbL	Layer-by-Layer
BL	Blocking layer
TL	Transparent titania layer
SL	Scattering layer
D	Diffusion coefficient
J_{lim}	Limiting current density
R_S	Series resistance
R_{Sh}	Shunt resistance
TA	Tannic acid
SC	Sodium citrate
OFET	Organic field effect transistor

Abstract

The aim of this thesis is to assess the possible applications of noble metal nanoparticles (NPs) in the fields of solar energy production and chemical sensing. The research project arises directly from the well-known extraordinary properties of noble metal NPs, namely the optical and electrical properties, high surface area, high catalytic activity and surface enhanced Raman scattering effect.

More specifically, concerning the energy production field, the first part of the thesis will deal with the application of Au NPs as counter electrode material in dye sensitized solar cells (DSSCs). This study was conducted in the S.O.L.A.R.E. laboratory at the Istituto per i Processi Chimico-Fisici of the Italian National Research Council (IPCF-CNR) in Messina, under the supervision of Dr. Giuseppe Calogero.

To the best of our knowledge, the role of noble metal NPs as exclusive counter electrode material in DSSCs has not been explored yet, despite their catalytic activity (i.e. applications in water purification) and electron conductivity have been massively studied. On the other hand, gold mirror thin films were used in combination with graphene nanoplatelets for the fabrication of the counter electrode in the most efficient DSSC reported in literature. For this reason, the work conducted towards the realisation of this thesis has been focused on the development of an efficient and reproducible method for the fabrication of Au based counter electrodes for DSSCs. Two different methods have been proposed, namely the thermal decomposition of $HAuCl_4$ as bottom-up method and the pulsed laser ablation of a gold target as top-down method. They were compared on the basis of the counter-electrodes optical properties, surface morphology, catalytic activity and performance both in dummy cells and fully assembled DSSCs. In the latter case, the adequate photoanode configuration has been studied, in order to

reduce the electron recombination and maximize the solar-to-electric power conversion efficiency. In addition, the fabricated gold counter-electrodes were compared to standard platinum ones.

In the second part of the thesis, the use of Ag NPs for the fabrication of multiresponsive plasmonic sensing platforms for surface enhanced Raman scattering (SERS) and chemiresistive sensing will be presented. This work has been conducted in the Nanochimie laboratory at the Institut de Science et d'Ingénierie Supramoléculaires (ISIS) in Strasbourg, under the supervision of Prof. Paolo Samorì.

The development of SERS based sensors has experienced an enormous growth in the last decades, as a consequence of their high versatility, high sensitivity, ease of fabrication and low cost. However, despite the inherently higher SERS activity of Ag compared to Au, sensing platforms based on Au NPs are already commercially available, while Ag NPs are mainly employed as colloidal dispersions, due to their lower chemical stability arising from oxidation. On the other hand, the extraordinary electrical properties of noble metal NPs made them suitable as active conductive materials in chemiresistors. Within this context, different synthetic procedures have been used to obtain citrate stabilized Ag NPs, tannic acid stabilized Ag NPs and Au@Ag core@shell NPs. Besides the study of their optical properties in colloidal solutions, they were compared by means of their ability to give rise to uniform thin films on chemiresistive devices, using both the cross-linking with dithiols and the electrostatic layer-by-layer deposition. The best results were obtained with the electrostatic layer-by-layer deposition of tannic acid stabilized Ag NPs, so that the optical properties, surface morphology, SERS and chemiresistive activity of these devices was largely studied. Furthermore, the possibility to use the fabricated sensing platforms for the

sensing of mercury ions in water by both indirect SERS and resistance variation was explored.

1 Introduction

1.1 Noble metal nanoparticles

Since their first use as decorative pigments, noble metal nanoparticles (NPs) demonstrated to have very unique and fascinating properties. Nowadays, it is still possible to admire the Lycurgus cup, dated IV century BC, whose unique optical properties can be ascribed to the presence in the glass matrix of small metal crystals containing Ag and Au with a molar ratio of about 14:1 and a diameter of ~70 nm. For this reason, the glass cup appears green when illuminated from the outside and observed in reflected light (Figure 1-1A), while it looks ruby red when the light comes from the inside and is transmitted through the glass (Figure 1-1B).[1] The Romans were thus able to use colloidal NPs to represent Lycurgus myth: in the Iliad, Homer depicts Lycurgus as a strong, mighty king, who was punished with blindness when he dared to challenge “mad Bacchus”, heavenly God of grape-harvest and wine.[2] However, the famous cup represents another version of the myth, showing Lycurgus being tangled up by the Greek nymph and disciple of Bacchus, Ambrosia, who is disguised as a vine.[3] The synthetic route used by the Romans is not clear yet, but several studies conducted on the Lycurgus cup suggest that the simultaneous presence of silver, gold, copper and antimony in the soda-lime-silica glass matrix and the heat treatment could have caused the precipitation of a fine dispersion of Ag-Au alloy NPs.[4, 5]

Later on, in Mesopotamia during the 9th century AD, silver and/or copper NPs were dispersed within the outermost layers of glazed ceramics to obtain metallic luster decorations: for example, the medieval glaze in Figure 1-1C shows iridescence under specular reflection, with shiny blue and green colours. When transmission electron microscopy (TEM) analysis is

performed on the sample, a double layer of silver nanoparticles with sm aller sizes (5–10 nm) in the outer layer and larger ones (5–20 nm) in the inner layer can be observed (Figure 1-1D). A schematic representation of the interference between the two layers with constant distance of about 430 nm is shown in Figure 1-1E. The light scattered by the second layer has a phase shift with respect to the one scattered by the first layer: each wavelength is scattered differently, since the phase shift depends on the wavelength of the incoming light.[6, 7]

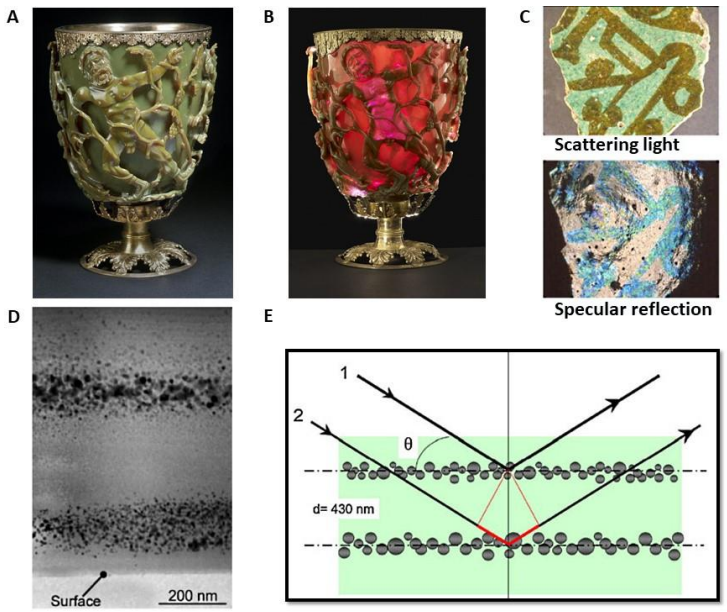

*Figure 1-1 Lycurgus Cup (British Museum; IV century BC) illuminated **A)** from the outside and **B)** from the inside. **C)** Medieval piece of a glazed ceramic (9th century AD) observed by scattered light and specular reflection. **D)** TEM image of the double layer of silver nanoparticles. **E)** Schematic representation of interference phenomena due to the double layer with an interlayer distance of 430 nm. Adapted from references [6, 7].*

1.1.1 Optical properties of noble metal nanoparticles

The beautiful examples reported in the previous Section suggest that noble metal NPs are characterized by extraordinary optical properties, that make them suitable for a high number of applications. The optical properties are

exploited when light interacts with matter, thus an exact analysis can be obtained solving the Maxwell equations with the appropriate boundary conditions. However, this goes beyond the scope of this thesis. More classically, when a NP is illuminated, the electromagnetic (EM) field of light interacts with the conduction electrons, which usually move freely inside the particle creating the so-called plasmon. As a consequence, an electric dipole is created, so that negative and positive charges accumulate in opposite regions in the particle and the generated electric field results opposite to the light one. Since the size of the NP is much smaller than the photon wavelength, the resulting plasmon oscillation is distributed over the whole particle volume, hence localized surface plasmons (LSPs) are created. The electrons displacement generates a restoring force, so that when the external field is removed, they oscillate with a resonant plasmon frequency.[8, 9] Consequently, a resonance is achieved as soon as the frequency of the EM radiation approaches the LSP frequency, so that a localized surface plasmon resonance (LSPR) band can be observed in the extinction spectrum of the NPs colloid.[10] The extinction cross-section for metallic NPs, which depends also on the power of the incident light, is the summation of the absorption and scattering contributions and it is defined as the effective area of a homogeneous incoming beam from which they will absorb or scatter every photon. Additionally, LSPR is strongly dependent on the NP size or shape, the dielectric function of the surrounding medium and the nature of the metal. In Figure 1-2A-B, it is possible to notice that two kinds of transitions are excited when Ag and Au NPs are illuminated. Apart from the LSPR, interband transitions have a certain probability to take place. In the case of silver, the two bands are well-resolved, since the interband energy is quite high (Figure 1-2C) and this behaviour can be described with a lossless Drude model.[11] A completely different situation can be observed within Au NPs spectrum. As

shown in Figure 1-2D, the interband energy is small, so that losses, associated to the transition between d levels and the conduction band, are likely: interband transitions and LSPR overlap, resulting in the decay into electron-hole pairs and a reduced plasmon intensity.[8, 9, 12] However, although Ag outperforms Au, usually Au is preferred due to its higher chemical stability and biocompatibility in most applications.

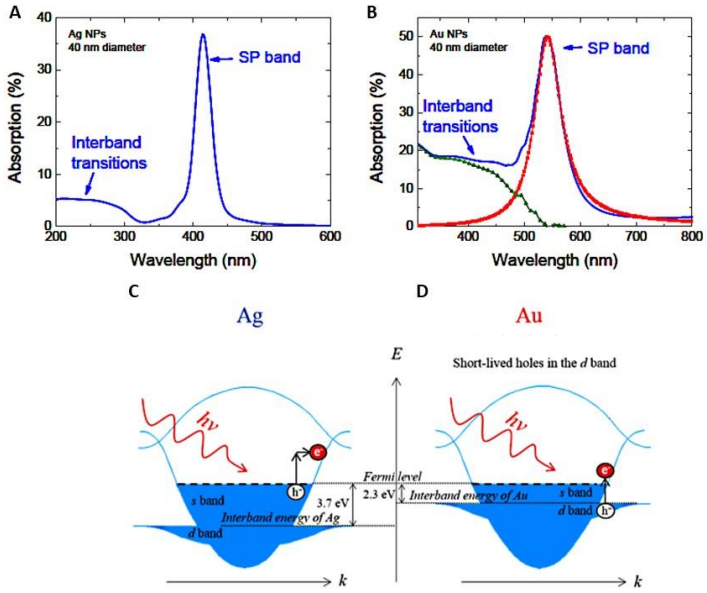

*Figure 1-2. Optical absorption spectra for **A)** Ag and **B)** Au NPs embedded in a silica matrix with dielectric function ε = 2.25 (diameter 40 nm). For Au NPs, the contributions to the optical absorption of interband transitions and LSPR are resolved. Adapted from Reference [8]. Schematic representation of phonon-assisted **C)** intraband electronic transition in Ag NPs and **D)** interband electronic transition in Au NPs when irradiated with Vis light. Adapted from Reference [12].*

The optical properties of noble metal NPs are influenced not only by the nature of the metal, but also by the size and shape of the particles. Adjusting the synthetic procedure, various morphologies can be obtained, spanning from nanospheres to nanocubes, hexagonal shapes, nanorods and nanostars (Figure 1-3). Interestingly, all these NPs have different optical properties. For example, in the case of gold nanorods with different aspect ratios (the length divided by the width), this effect is visible to the naked eye.

The UV-Vis spectra for gold nanorods typically show two bands: one at higher energy, corresponding to the collective oscillation of free electrons in the presence of the external EM field along the transverse dimension, and the other at longer wavelengths, corresponding to the absorption and scattering of light along the longitudinal dimension of the nanorod.[13] As the length of the rod increases, it is possible to observe a shift of the band at longer wavelengths, from the visible to near infrared, and the colour of the corresponding dispersions changes from pink to blue, green and brownish (Figure 1-3F-H).[7]

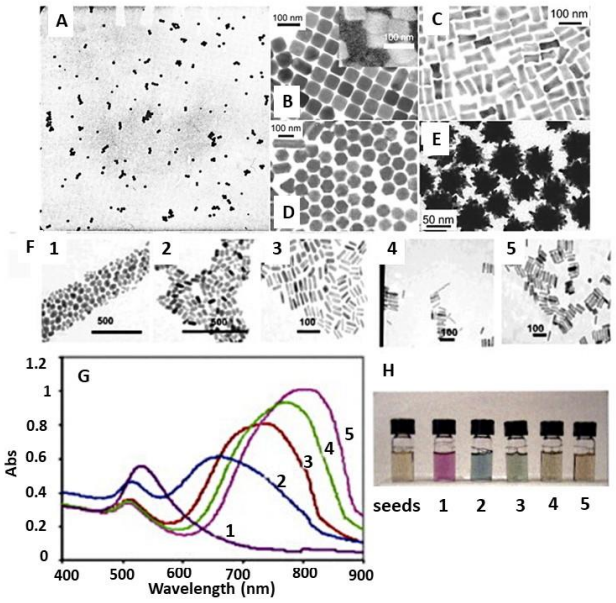

Figure 1-3 TEM images of Au NPs with different shapes: ***A)*** *nanospheres,* ***B)*** *nanocubes,* ***C)*** *nanorods,* ***D)*** *hexagons,* ***E)*** *nanostars. Au nanorods with different aspect ratio (the length divided by the width):* ***F)*** *1-5 TEM images,* ***G)*** *UV-Vis spectra and* ***H)*** *photographs of the dispersions. Adapted from Reference* [7]*.*

Nowadays, numerous strategies for the synthesis of noble metal NPs have been reported in literature, but they can be mainly divided in two macro-groups, namely bottom-up and top-down methods. The former deals with the

reaction of atoms or molecules under specific chemical or physical conditions, while the latter is essentially the reduction in NPs of bulk materials by means of physical, mechanical or chemical processes.[14]

1.1.2 Bottom-up synthesis of noble metal nanoparticles

The chemical reduction of precursors is one of the most common methods for the synthesis of noble metal NPs. Apart from the precursor, two species are fundamental for the synthesis, namely the reducing agent and the stabilizer, and two steps are essential, namely the nucleation and the growth. In 1951 Turkevich reported the *in situ* synthesis of Au NPs with a size of 20 nm from the reduction of chloroauric acid ($HAuCl_4$) in boiling water containing sodium citrate as stabilizing and reducing agent.[15] The method was later improved by Frens, who found that Au NPs with sizes ranging from 15 to 150 nm can be obtained adjusting the $HAuCl_4$: citrate ratio.[16]

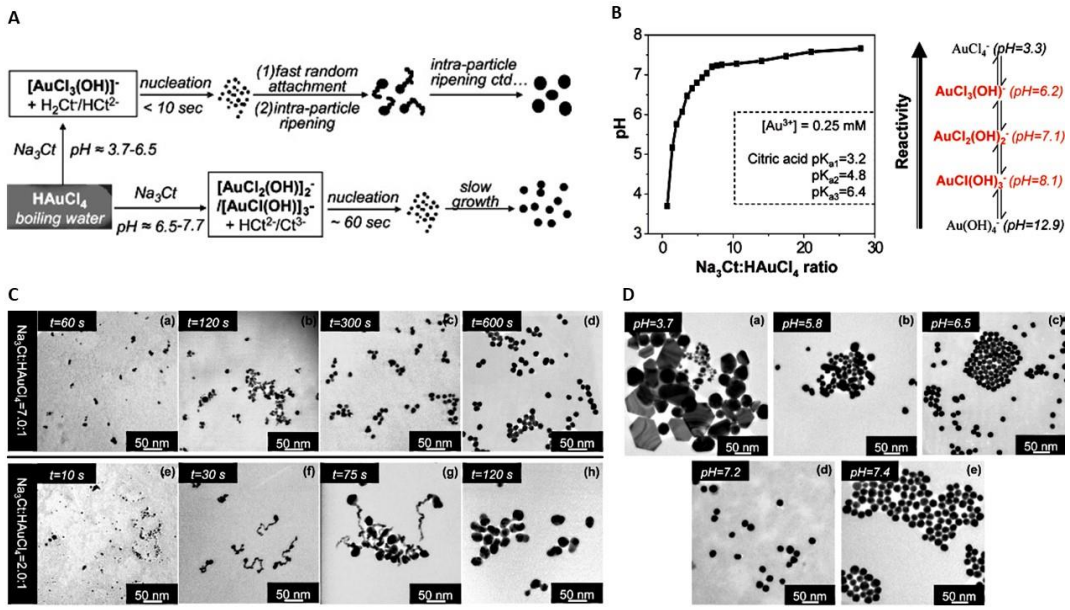

Figure 1-4 ***A)*** *Schematic illustration of the two possible reaction pathways for the synthesis of Au NPs as a function of the solution pH.* ***B)*** *Variation of the solution pH upon the addition of sodium citrate to a chloroauric acid solution (0.25 mM) and structure and reactivity of gold*

complexes as a function of pH. ***C)*** *TEM images showing the temporal evolution of Au NPs size and shape using high (top row) and low (bottom row) citrate:$HAuCl_4$ ratio.* ***D)*** *TEM images of Au NPs synthesized varying the solution pH, but with fixed initial $HAuCl_4$ and citrate concentrations. Adapted from Reference* [17]*.*

Here, nucleation and growth take place in the same process, and the size distribution is determined by various parameters, such as temperature, pH and strength of the reducing and stabilizing agents. Since citrate is a weak base, changing its concentration, the solution pH is also changing. Furthermore, the reactivity of gold complexes, reflected by their reduction potentials, varies markedly when the pH changes (Figure 1-4B). As shown in Figure 1-4 A, Ji *et al.* found that two different reaction pathways are followed when the synthesis is carried out at low and high pH values. Under high pH (6.5-7.7), which correspond to a high citrate: chloroauric acid ratio, nucleation is quite slow (~ 60 sec) and it is followed by slow diffusion-controlled growth, giving rise to relatively small NPs. When the pH is lower (3.7-6.5), the higher reactivity of the formed gold complexes is accompanied by a faster nucleation, followed by random attachment and intra-particle ripening, giving rise to relatively larger NPs with higher polydispersity. The TEM images showing the temporal size and shape evolution of Au NPs as a function of citrate: $HAuCl_4$ ratio and pH are shown in Figure 1-4 C-D.[17]

Other common *in situ* synthesis of Au NPs are carried out using different stabilizing agents, such as borohydride, hydrazine, formaldehyde, hydroxylamine, citric and oxalic acid, polyols, hydrogen peroxide etc., or stabilizing agents, such as thiolates, phosphorus-, nitrogen-, oxygen-based ligands, dendrimers, polymers and surfactants (*i.e.* cetyltrimethylammonium bromide, CTAB).[18]

When the Turkevich method is applied to the synthesis of Ag NPs starting from $AgNO_3$, the ability of citrate to form relatively stable complexes with positively charged silver ions, leads to the formation of relatively big and polydisperse Ag NPs (30-150 nm) and a variety of shapes, such as spheres,

rods, plates and polyhedra.[19] Pillai *et al.* showed how citrate is able to influence the particles growth and morphology. The augmented absorbance of the broad plasmon band at 420 nm with time is a clear sign of a slow particle growth, whose rate is also influenced by citrate concentration. (Figure 1-5C) The TEM images in Figure 1-5A-B show that small spherical Ag NPs are formed in the early stage of the reaction, but the presence of citrate induces their agglomeration into nanoclusters, until an optimal size. However, the small particles undergo the so-called Ostwald ripening process: they are reoxidized to Ag^+ ions and then adsorbed on the surface of bigger particles, where they are reduced. A complete scheme of the nucleation and primary and secondary growth of Ag NPs in the presence of citrate is shown in Figure 1-5D.[20]

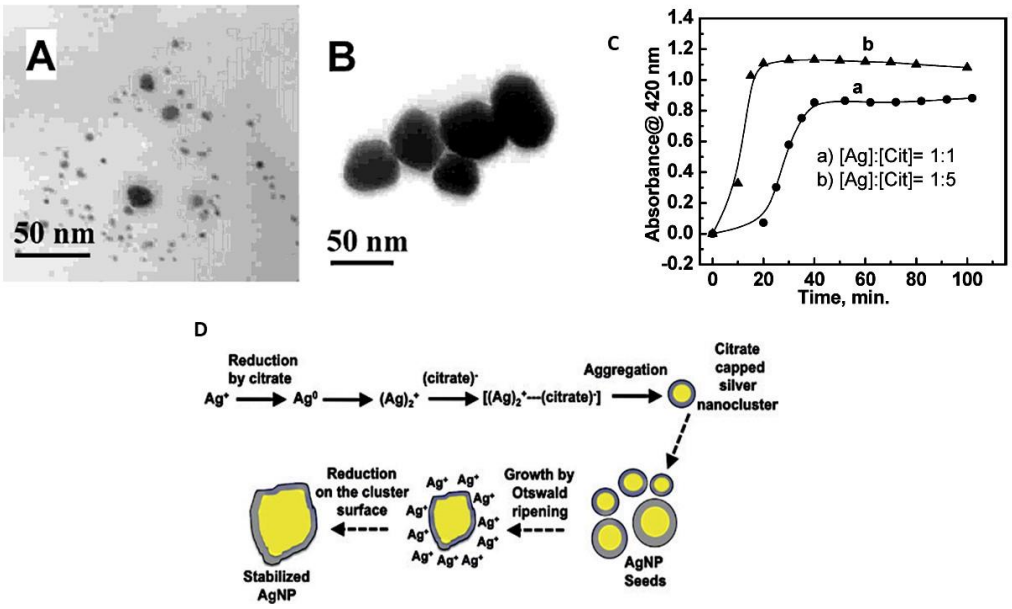

*Figure 1-5 TEM micrographs of silver colloids at **A)** an early stage and **B)** a later stage of the synthesis performed using sodium citrate as reducing and stabilizing agent. **C)** Temporal evolution of the absorbance of the Ag NPs plasmon band at 420 nm for different Ag^+:citrate ratios. **D)** Schematic representation of the nucleation and primary and secondary growth of Ag NPs in the presence of citrate. Adapted from Reference [20].*

More recently, aiming to obtain better size and shape control of the NPs, seeded-growth methods have been developed, based on the temporal separation of nucleation and growth. Bastús *et al.* proposed this method for the synthesis of highly monodisperse Au NPs: the nucleation occurs in boiling water in the presence of sodium citrate, thus producing small seeds (~8 nm). Later, seeds growth is performed thanks to the accurate control of temperature and number of Au atoms added in every growth step. Indeed, after the synthesis of Au seeds, the subsequent steps were carried at 90°C in order to favour growth against secondary nucleation and, besides, avoid the Ostwald ripening process. The TEM images in Figure 1-6A show the step by step increase in the size of Au NPs after every growth step (from ~8 to ~180 nm). The UV-Vis spectra of the gold colloids in Figure 1-6B exhibit a well-defined LSPR band, which is peaked at 518 nm for the Au seeds, while it is red shifted at every growth step; furthermore, the increasing absorbance is a proof of the deposition of Au on the preformed seeds.[21]

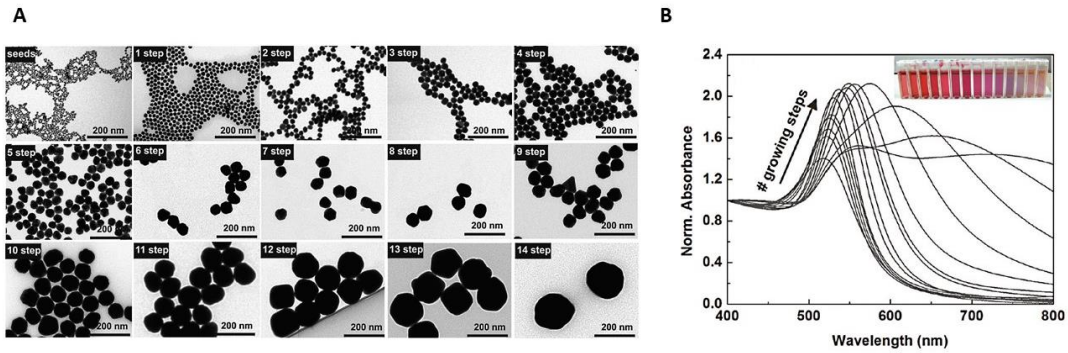

Figure 1-6 ***A)*** *TEM micrographs of the Au NPs after the nucleation and every growth step, with sizes ranging from ~8 to ~180 nm.* ***B)*** *UV-Vis spectra of the gold colloids after different growth steps. Adapted from Reference* [21]*.*

Unlike the above-mentioned solution processed bottom-up methods, a direct synthesis method of noble metal NPs is the thermal decomposition of solid

precursors, which is useful for the production of large amounts of material, but, on the other hand, appears to be a complex process, due to the high number of factors affecting the solid-state and solid-gas systems. Thus, suitable precursors, heating rate, annealing time, temperature and atmosphere should be carefully selected and controlled.[22] Wang *et al.* succeeded in the synthesis of Ag NPs from the thermal decomposition of silver nitrate in a chemical vapour deposition system with a source temperature of 400°C, while the substrate temperature varies in the range 110-350°C. Ag NPs were synthesized on TiO_2 films. The authors observed that the particles size decreases from 75 to 25 nm when the distance from the silver source, which is directly proportional to the decreased substrate temperature, varies from 15 to 25 cm. Furthermore, when different values of pressure are applied on TiO_2 anatase or rutile, nanorods or nanoplates are formed, respectively. SEM images of the obtained Ag nanostructures and a schematic representation of the synthetic procedure are shown in Figure 1-7A-F.[23]

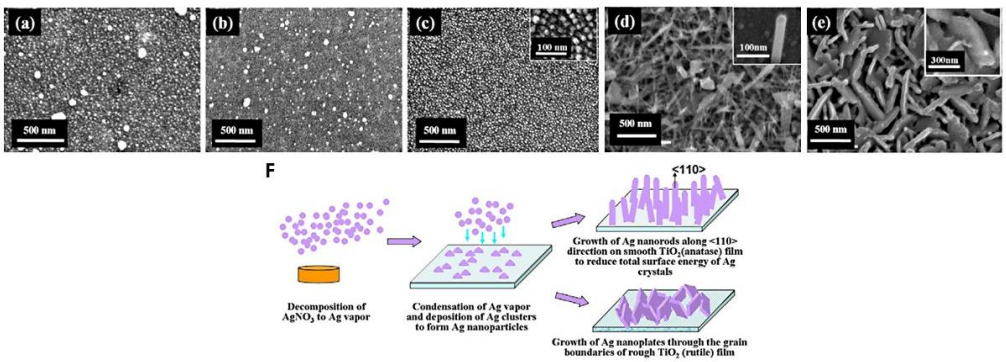

*Figure 1-7 SEM images of the synthesized Ag NPs on TiO_2 film at a distance of **A)** 15 cm, **B)** 20 cm, **C)** 25 cm from the silver source and **D)** Ag nanorods on TiO_2 anatase, and **E)** Ag nanoplates on TiO_2 rutile. **F)** Schematic representation of the growth mechanism of Ag NPs, nanorods and nanoplates on TiO_2 film. Adapted from Reference [23].*

Similarly, the thermal decomposition of precursor salts dissolved in organic solvents is particularly suitable for the direct formation of NPs on the desired substrate surface, for various technological applications, as it will be shown later in this thesis.[24]

1.1.3 Top-down synthesis of noble metal nanoparticles

An effective technique for the preparation of noble metal NPs is the laser ablation synthesis in solution (LASiS), which relies on the pulsed laser irradiation of a bulk metal source dipped in a liquid solution. Although a comprehensive explanation of the synthetic procedure is still lacking, it has been established that photons are absorbed in the irradiated area of the metal source, thus causing heating and photoionization, which give rise to the expulsion of material generating an expanding plasma plume. Supersaturation in the plasma plume is the major driving force for the nucleation of NPs, which is followed by diffusion-limited growth and coalescence, also favoured by the cooling effect of the surrounding liquid. The size distribution and morphology of the particles can be influenced by various factors, such as the nature of the solvent and the presence of electrolytes or surfactants.[25, 26] Tilaki *et al.* studied the laser ablation of copper in deionized water and acetone and noticed that in the first case the obtained particles observed with TEM are characterized by an average size of 30 ± 14 nm and have a core@shell structure, which can be ascribed to the presence of a Cu core and a CuO shell. Furthermore, the diffraction pattern of the obtained particles confirms this observation. On the other hand, when the ablation is performed in acetone, the particles, all appearing in the same contrast, have an average size of 3 ± 1.3 nm and the diffraction pattern is the typical one for Cu NPs. These findings clearly suggest that water has a role

in the surface oxidation of the obtained particles, while acetone works as a capping layer on the NPs surface, thus preventing oxidation.[27] Although one of the main advantages of LASiS is the possibility to synthesize uncapped naked NPs in solution, it was demonstrated that the absence of a capping agent is the reason for the formation of big NPs aggregates, which are also prone to precipitation. Mafuné *et al.* studied the influence of sodium dodecyl sulfate (SDS) on the ablation of Ag in water and found that the average diameter of Ag NPs decreases as the SDS concentration increases.[28] (Figure 1-8A-C)

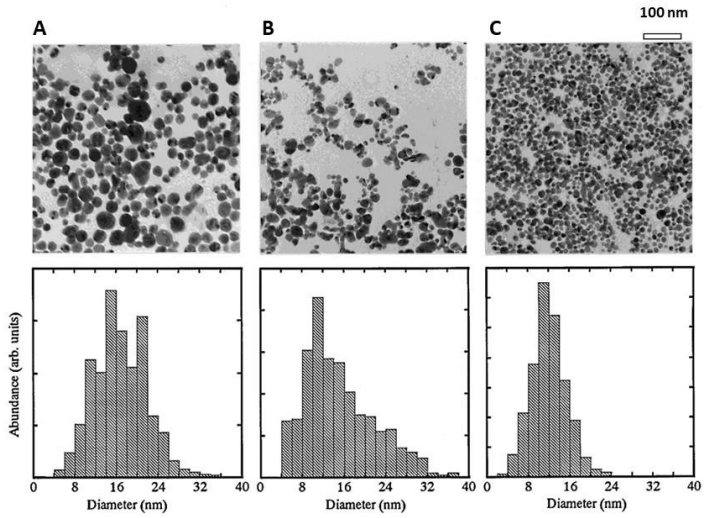

*Figure 1-8 TEM micrographs and size distribution of Ag NPs prepared by laser ablation synthesis in solution (LASiS) in aqueous solution of SDS **A)** 0.003 M, **B)** 0.01 M and **C)** 0.05 M. Adapted from Reference [28].*

LASiS revealed to be a feasible method for the synthesis of ligand-free AuAg bimetallic NPs: Ag is ablated in a gold colloidal solution and the composition and the optical properties, consequently, strongly vary with the initial Au NPs concentration.[29, 30]

The laser-metal target interaction can take place also in a different environment, such as in vacuum or in the presence of a background gas. In

these cases, pulsed laser deposition or ablation (PLD or PLA) is a useful technique for the deposition of nanostructured thin films, as it will be shown later in this thesis.

1.2 Dye-sensitized solar cells

Dye-sensitized solar cells (DSSCs), along with perovskite solar cells, can be considered the most promising alternatives to conventional Si-based or thin film solar cells, being able to convert solar energy to electricity with acceptable efficiency and moderate costs.[31, 32]

DSSCs appeared in literature in 1991 for the first time, when Grätzel and O'Regan proposed a low cost and highly efficient solar cell,[33] based on light harvesting by a sensitizing dye attached to a wide band gap semiconductor.[34–37]

State-of-the-art DSSCs based on iodide/triiodide or cobalt based redox couples in a liquid electrolyte reached validated power conversion efficiencies (η or PCE) of 14%,[38] while, when a solid-state hole conductor is used, PCE can reach values over 5%.[39] Nowadays, several companies are able to manufacture DSSCs for residential installations as well as consumer electronics.

A typical DSSC can be schematized as a photoanode or photoelectrode (PE), constituted by a dye adsorbed on a n-type semiconductor oxide (typically TiO_2 in the anatase phase), in contact with a hole transporting material (HTM), such as a liquid electrolyte. The flow of charges in the system is ensured by the presence of a catalytic material on the counter-electrode (CE) surface. Both the PE and the CE are made of conducting glass, prepared covering the glass with a transparent conducting oxide (TCO), typically indium tin oxide (ITO) or fluorine-doped tin oxide (FTO).[33, 40, 41] The

working principle of a DSSC under solar illumination is presented in Figure 1-9.

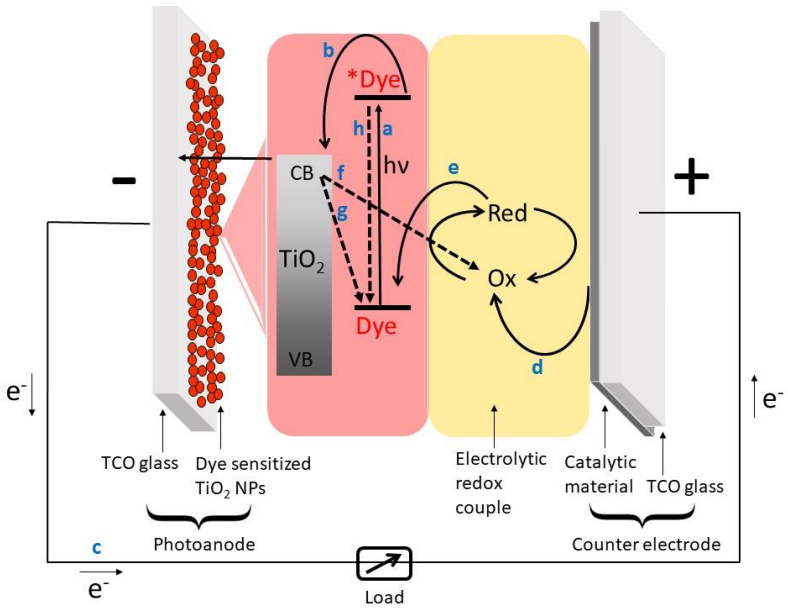

Figure 1-9. Schematic representation of the working principle of a DSSC under solar illumination. Recombination processes are indicated by dashed arrows.

$$Dye + h\nu \rightarrow {}^{*}Dye \quad (a$$

$${}^{*}Dye \rightarrow Dye^{+} + e_{cb}^{-}(TiO_2) \quad (b$$

$$Ox + e^{-}(cathode) \rightarrow Red\,(cathode) \quad (c$$

$$Dye^{+} + Red \rightarrow Dye + Ox \quad (d$$

$$Ox + e_{cb}^{-}(TiO_2) \rightarrow Red + TiO_2 \quad (e$$

$$Dye + + e_{cb}^{-}(TiO_2) \rightarrow Dye + TiO_2 \quad (f$$

$${}^{*}Dye \rightarrow Dye + h\nu' \text{ or } \Delta \quad (g$$

Upon irradiation, (a) photon absorption gives place to the excitation of electrons from the dye Highest Occupied Molecular Orbital (HOMO) to its Lowest Unoccupied Molecular Orbital (LUMO), thus leading to the formation of *Dye, (b) which is then able to inject charges from the LUMO in the conduction band of the TiO_2 semiconductor. Here, electrons firstly diffuse in

the disordered TiO_2 network until they reach the back contact of the anode and then (c) to the CE, through the external circuit. Simultaneously, (d) thanks to the presence of a catalytic material on the CE surface, reduction of Ox (oxidized form of the electrolyte) occurs, while (e) Dye^+ (oxidized dye) rapidly transfers its holes to Red, the electron rich form of the redox couple. A good dye regeneration is ensured when the energy of the HOMO of the redox mediator is higher than the dye one. However, the electron transfer events here described can be limited by several undesirable loss reactions, such as the charge recombination from the semiconductor conduction band (f) to Dye^+ which gives rise to the so-called dark current, or (g) to Ox (recombination back reaction), and (h) the (radiative or non-radiative) decay of the LUMO level of the dye to its HOMO one.[42] The typical time constants for the described processes are shown in Figure 1-10.

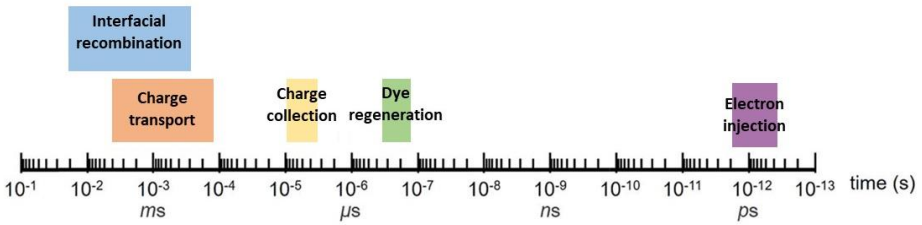

Figure 1-10 Overview of the typical timescale of the main kinetic processes occurring in a DSSC. Adapted from Reference [43].

Since their first appearance in literature, researchers have worked on the optimization of all the components of DSSCs, in order to maximize the cell performances. However, before reviewing the recent advances in the field, the device key parameters and figures of merit (FoM) should be presented.

1.2.1 Key parameters and figures of merit

1.2.1.1 Photoconversion efficiency

The photoconversion efficiency (PCE) of a solar cell is given by the ratio between the maximum generated power (P_{max}) and the power of the incident light (P_{in}) and it is usually calculated by the following equation:

$$\eta = \frac{P_{max}}{P_{in}} = \frac{J_{max} \cdot V_{max}}{P_{in}} = \frac{J_{SC} \cdot V_{OC} \cdot FF}{P_{in}}$$

The key parameters are the photocurrent and photopotential which can be experimentally measured under different conditions, such as open or short circuit and under monochromatic or sunlight illumination.

1.2.1.2 Short circuit density

The short circuit density (J_{sc}) is the highest current density that a cell can supply at 1 sun when it is short-circuited. The J_{sc} is closely related to the ability of the dye to absorb light over a wide range of wavelengths and to inject electrons from its excited level to the semiconductor conduction band (Eqn (a, Eqn (b). Furthermore, higher is the rate of dye regeneration (Eqn (d) ensuring low values of dark current (Eqn (f), higher is the J_{sc}. Indeed, the overall J_{sc} is given by the following equation:

$$J_{SC} = J_{inj} - J_{rec}$$

Where J_{inj} represents the injection current, while J_{rec} is the recombination current contributing to the photovoltaic (PV) performance loss. In particular, J_{SC} is closely related to the light harvesting efficiency (LHE), the charge

injection and charge collection efficiencies,[44] which will be presented in Section 1.2.1.5.

1.2.1.3 Open circuit voltage

Another key parameter which can be highly affected by the recombination processes is the open circuit voltage (V_{oc}): it represents the electrical potential difference when no current is flowing between PE and CE under illumination. The maximum V_{oc} for a DSSC is given by the difference between the quasi-Fermi energy level for the semiconductor (E_{cb}) and the redox potential of the electrolytic couple (E_{red}). Nevertheless, a more complete description of the V_{oc} is given by the following equation:

$$V_{OC} = \frac{kT}{q} \ln\left(\frac{\eta \Phi_0}{n_0 k_{ET}[Ox]}\right)$$

Where k is the Boltzmann constant, T is the absolute temperature, q is unit charge; η and Φ_0 are closely related to the J_{inj} and they represent the photogenerated electrons quantum yield and the incident photon flux, respectively. The influence of the loss reactions is given by the terms n_0, k_{ET} and [Ox] which are the electron density in the semiconductor conduction band in the dark, the recombination rate constant and the concentration of the oxidized form of the electrolyte, respectively.[45]

1.2.1.4 Fill Factor, series and shunt resistances

The fill factor (FF) is a measure of the quality of the cell, since it is given by the ratio between the maximum theoretical power ($P_{max} = J_{max} \cdot V_{max}$) and the real output power ($P_{out} = J_{SC} \cdot V_{OC}$). It is calculated as the ratio between the blue and the green shaded regions in Figure 1-11A. This parameter

represents the easiness of extraction of the photo-generated charge carriers from the solar cell. The FF can assume values in the range 0-1. Indeed, if we consider the V_{oc} as the illumination dependent resting potential of the cell, the FF value will differ from unity as the V_{oc} faces voltage losses; the latter are caused by the presence of internal resistances when an external load is connected and the current starts to flow.[46] The FF can be affected by the series resistance (R_S) and the shunt resistance (R_{sh}): the former can be associated to the bulk resistance of the materials and the electrodes, the contact resistance at the interface between the various cell components and charge transfer resistance in the semiconductor material. High values of R_S give rise to a smaller voltage drop in the diode, inducing a slower increase of current with voltage (Figure 1-11B). On the other hand, R_{sh} is related to the presence of alternative paths for the photogenerated current, for example in the traps or the pinholes in the semiconducting film or high degree of recombination. Low values of R_{sh} are associated to huge current leakage in the cell, causing a decrease of current with the applied voltage (Figure 1-11B).

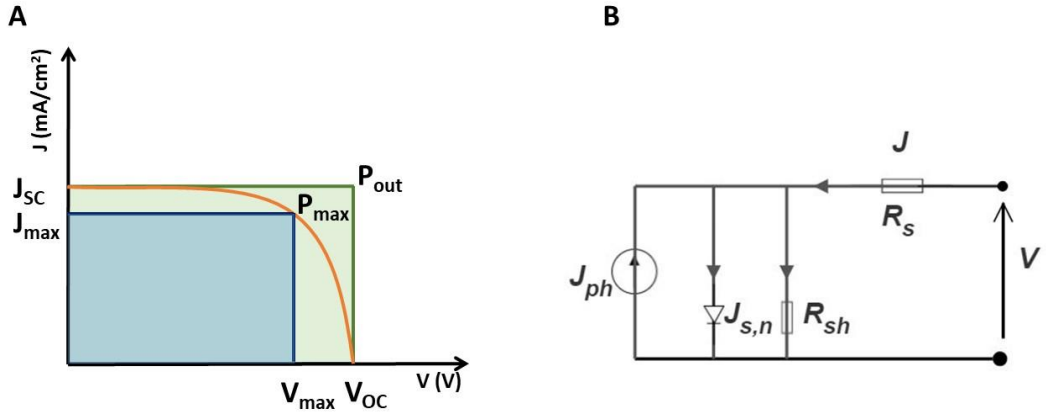

Figure 1-11 ***A)*** *Hypothetical Current-Voltage (I-V) curves. Various important cell parameters are also indicated in the figure.* ***B)*** *Equivalent circuit for a solar cell showing the photogenerated current density J_{ph}, the current flowing in the external load J and the applied voltage V, the series and shunt resistances, R_s and R_{sh}, respectively.*

The R_S can be calculated as the slope of the I-V curve around the V_{OC} value. A high value of R_S negatively affects the overall PCE of the cell, as shown in Figure 1-12A. On the other hand, the R_{sh} can be calculated as the slope of the I-V curve around the J_{SC} point and when its value approaches infinity, the PV device is characterized by high FF values (Figure 1-12B).[45, 47, 48]

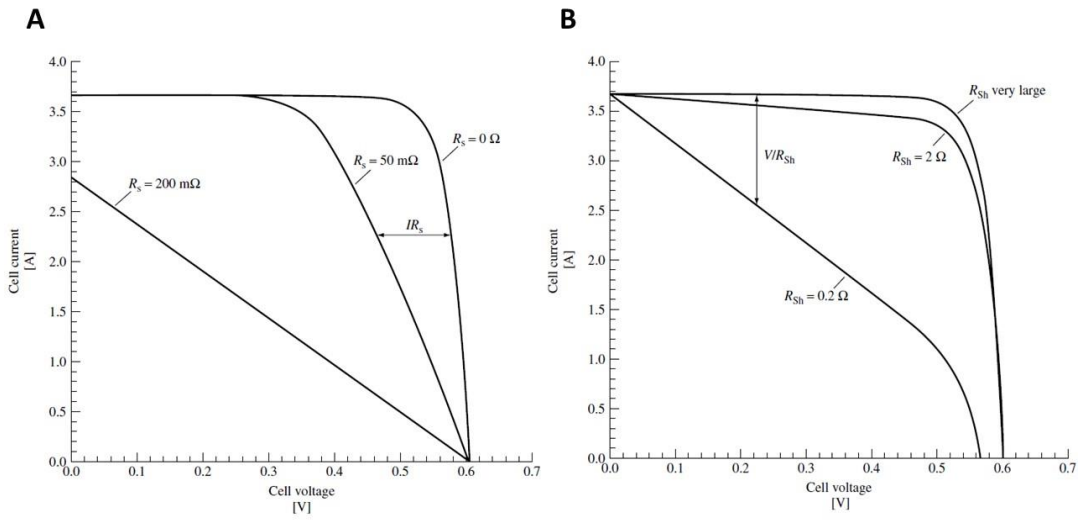

Figure 1-12 ***A)*** *Effect of the series resistance (R_s) variation on the I-V characteristic of a solar cell, when the shunt resistance R_{sh} is infinite.* ***B)*** *Effect of the shunt resistance (R_{sh}) variation on the I-V characteristic of a solar cell, when the series resistance R_s is zero. Adapted from Reference* [45].

1.2.1.5 Incident photon conversion efficiency

All the parameters described in the previous sections are measured under 1 sun illumination, while the incident photon conversion efficiency (IPCE) represents the external quantum efficiency (EQE) of the cell at a specific excitation wavelength (λ_{ex}). It is usually expressed by the following equation:

$$IPCE(\lambda_{ex}) = \Phi_A(\lambda_{ex}) \cdot \Phi_{inj} \cdot \Phi_{reg} \cdot \Phi_C$$

Where Φ_A (λ_{ex}) is the light harvesting efficiency (LHE) at λ_{ex}. This term can be evaluated by UV-Vis spectroscopy, since it is defined as $1\text{-}10^{-A}$, where A is the absorbance at λ_{ex}. Furthermore, Φ_{inj} is the electron injection efficiency from the *Dye LUMO level to the TiO_2 conduction band. Φ_{reg} is the efficiency of regeneration of Ox on the CE and Φ_C is the charge collection efficiency.[49] A schematic representation of the mentioned processes can be observed in Figure 1-13.

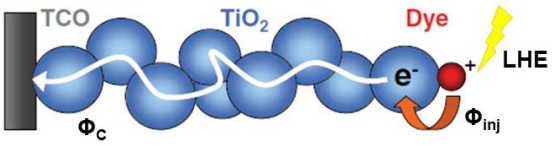

Figure 1-13 Schematic representation of the processes contributing to the IPCE: light harvesting, electron injection and charge collection and their efficiencies LHE, Φ_{inj} and Φ_C.

1.2.2 Device components

The main components of DSSCs are shown in Figure 1-14, as well as the main processes occurring in the cell.

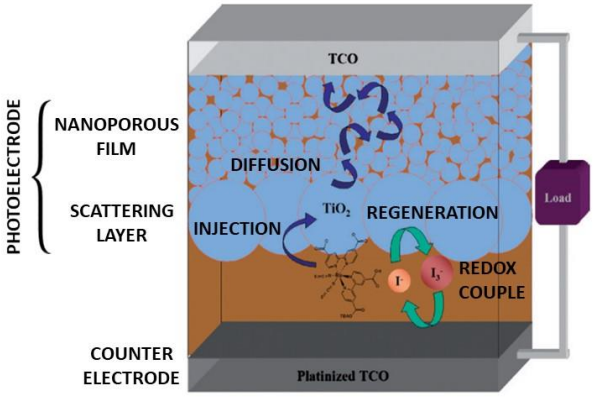

Figure 1-14 Schematic representation of the cell components and some of the main electron transfer processes.

1.2.2.1 Photoelectrode

A PE is usually fabricated by depositing a thin compact layer of a wide band gap semiconducting oxide on a TCO coated glass. As shown in Figure 1-15 for applications in PV, a semiconductor should be characterized by a suitable band position for the injection of electrons from the sensitizing dye. Indeed, owning a wide band gap (E_g > 3 eV), these semiconductors are characterized by absorption in the UV region, which implies the necessity of using a sensitizer with high extinction coefficient in the visible range.

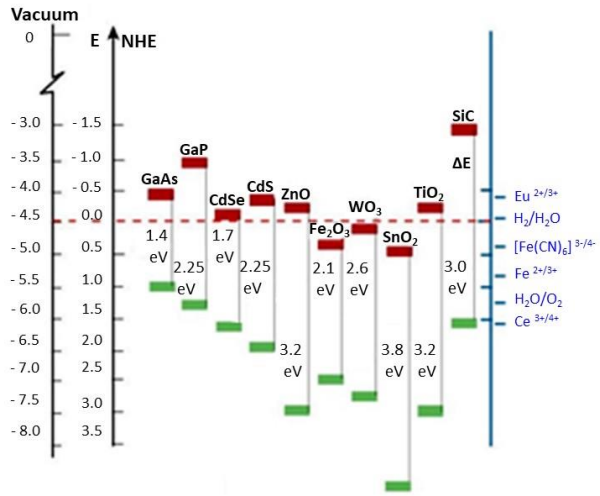

Figure 1-15 Comparison of the lower edge of the CB (in red), upper edge of the VB (in green) and band gap energy (in eV) for various semiconductors in contact with an aqueous electrolyte at pH 1. The standard redox potentials for some redox couples are shown, as well as the standard hydrogen potential. The energy scale is indicated in eV using both the vacuum and the normal hydrogen electrode (NHE) level as a reference. Adapted from Reference [50].

For sufficient dye loading, a nanoporous film of semiconductor should be used, in order to ensure a high surface area.[51] The most widely used semiconductor is TiO_2, but various examples of DSSCs carrying ZnO or SnO_2

can be found in literature. ZnO, owing a similar E_g, is considered the most promising alternative to TiO_2: it is characterized by low cost, high stability against photocorrosion and it has a high μ_e (115–155 $cm^2\ V^{-1}\ s^{-1}$), which ensures efficient electron transport in the semiconducting thin film and slow recombination rate.[52] However, ZnO based DSSCs are characterized by lower PCE compared to the TiO_2 based counterparts: Memarian *et al.* reported a PCE of 7.5% using ZnO polydispersed aggregates obtained by spray pyrolysis.[53] The formation of insulating agglomerates of Zn^{2+}/dye complexes, causing the dissolution of ZnO, limits the electron injection, when acidic dyes carrying carboxylic groups are used.[54] On the other hand, SnO_2 is characterized by higher E_g (3.8 eV) and μ_e (250 $cm^2\ V^{-1}\ s^{-1}$ and 125 $cm^2\ V^{-1}\ s^{-1}$ for single crystal and nanostructured SnO_2) compared to TiO_2 (E_g 3.2 eV and μ_e 1 $cm^2\ V^{-1}\ s^{-1}$),[55] but the low conduction band edge energy is the reason for the poor PV performance (PCE ~1.70%), which can be endorsed to low V_{oc} values (~0.4 V for iodide based electrolytes).[56] An alternative strategy to boost the PV performance, while taking advantage of the reported SnO_2 high μ_e value, is the fabrication of hybrid structures of SnO_2 and TiO_2: Gu *et al.* reported a PCE of 7.87% when using as PE material SnO_2@TiO_2 core@shell nanoparticles prepared by flame spray pyrolysis.[57]

Thus, an ideal photoanode should have the following characteristics:

• high surface area to ensure high dye loading;

• high electron mobility for a fast electron injection from the dye excited state and fast electron transfer from the dye to the external circuit;

• porous structure to facilitate the diffusion of the electrolyte;

• high resistance to photocorrosion;

• high scattering of the sun light to favour the absorption from the dye of the diffused light.[58]

A common methodology used to match these requirements envisages four layers of anatase TiO_2 with different particles sizes. A blocking underlayer

(thickness ~50 nm), whose role is to enhance the adhesion on TCO glass substrate and to help reducing the dark current generated by the charge recombination between the electrons in the TCO glass and the holes of the oxidized electrolyte. This is possible thanks to the reduction of the number of pores, which allow the infiltration of the electrolyte into the TiO_2/TCO interface and the formation of a compact thin layer.[59, 60](Figure 1-16)

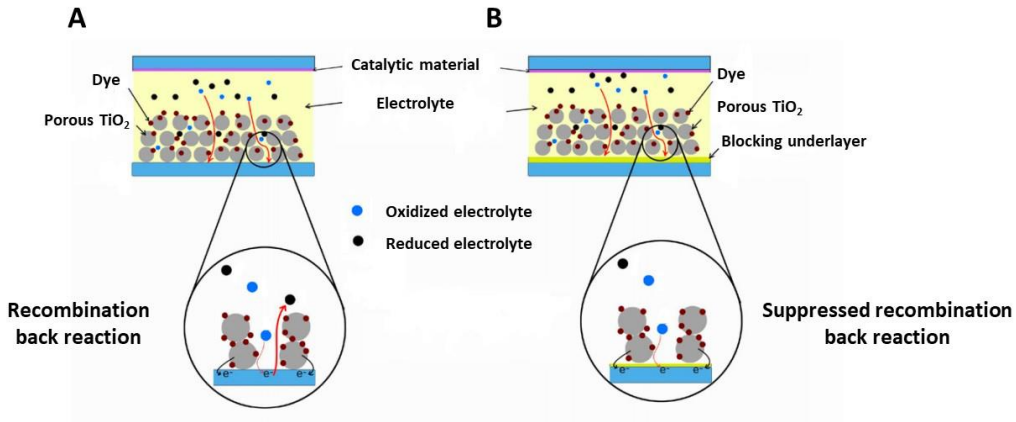

*Figure 1-16 Schematic representation of **A)** the recombination of electrons in the FTO back contact with the oxidized form of the electrolyte and **B)** its suppression in the presence of the blocking underlayer.*

The active layer is usually a transparent layer of mesoporous anatase TiO_2 nanoparticles with a diameter of ~20 nm. The thickness of the layer varies in the range ~5-12 µm, according to the extinction coefficient of the sensitizing dye. The large surface area of the NPs ensures the adhesion of a large number of dye molecules. Among the various techniques available, screen printing is the most efficient and reproducible one, allowing the deposition of ordered multilayers with the desired thickness.

A non-transparent scattering layer can be deposited on top of the active layer, acting as a photon trapping system: the presence of larger TiO_2

nanoparticles (~200-400 nm) causes an elongation of the optical path of the incident light enhancing light absorption.[61]

The post-treatment with $TiCl_4$ for the deposition of a thin layer of small TiO_2 nanoparticles (upper blocking layer) is usually performed, but the positive effect on the PV performance has been highly debated in literature. Among the others, the most common explanation is that small TiO_2 nanoparticles resulting from the vaporization of organic binders during the sinterization process, fill in the pores generating a more uniform film leading to easier electron transfer. However, Sommeling *et al*. showed an increase in photocurrent after the $TiCl_4$ treatment, but it was evident that neither the dye loading (probably more dye binding sites are provided) nor the decrease in charge transport losses or recombination could independently explain the results. They were also able to show a downward shift of the TiO_2 CB of ~100 mV, which in any case was not causing a decrease in V_{OC}: overall, we can assume that the efficacy of the $TiCl_4$ post treatment can vary widely, according to the quality of the starting TiO_2 active layer.[62]

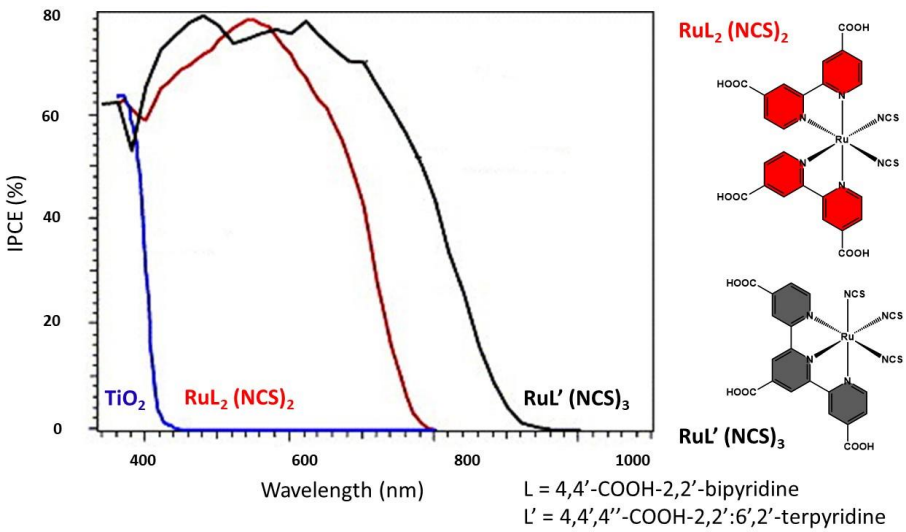

Figure 1-17 Incident photon to current conversion efficiency (IPCE) as a function of the wavelength for the standard ruthenium sensitizers ***N3*** *(cis-Bis(isothiocyanato) bis(2,2'-bipyridyl-4,4'-dicarboxylato ruthenium(II), red line), the black dye* ***N749*** *([[2,2''6',2''-terpyridine]-4,4',4''-tricarboxylato(3-)-N1,N1',N1'']tris(thiocyanato-N)hydrogen ruthenium(II),*

black curve), and the blank nanocrystalline TiO_2 film (blue curve). The chemical structures of the sensitizers are shown as insets. Adapted from Reference [67].

The necessity to use a molecular chromophoric compound arises from the really poor light absorption from wide band gap semiconductors, such as TiO_2 (Figure 1-17), whose absorption in the UV spectral range limits the efficiency of the electrical response.[63] The first class of sensitizers which found application in DSSCs are polypyridyl Ru(II) complexes, whose ancestor is $Ru(bpy)_3Cl_2$.

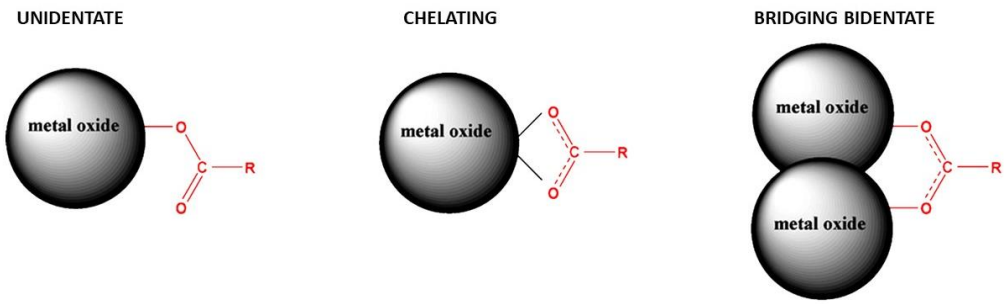

Figure 1-18 Binding modes of the dye through its carboxylic groups on TiO_2 NPs surface. Adapted from Reference [64].

Usually these complexes have a general $ML_2(X)_2$ formula, where L stands for 2,2′-bipyridyl-4,4′- dicarboxylic acid, M for Ru and X for water, halide, cyanide or thiocyanate. The carboxylic functionality represents the typical anchoring group for the sensitization of the semiconductor. As shown in Figure 1-18, the dyes can link to the TiO_2 surface through unidentate, chelating or bridging bidentate modes with the metal cation: however, the unidentate mode, involving an ester-like linkage, results in poor stability of the structure due to large rotational freedom of the dye molecules. For this reason, the chelating or the bridging bidentate modes are more common, thanks to the carboxylate linkage. Furthermore, the dyes anchoring is even more stable when it occurs through two carboxylic groups.[65, 66]

The so called N3 and black dye are among the most famous synthesized dyes for the first generation of Ru based DSSCs. Their structure and IPCE spectra in a DSSC are shown in Figure 1-17 compared with the photocurrent response of bare TiO_2. They are both characterized by high IPCE values (~80%) in the visible range, but the black dye response is extended also in the NIR region.[67]

A PCE of 10% was achieved employing the N3 dye, but its main drawback arises from the high degree of protonation of the free carboxylic groups in the bpy moiety, which causes the downshift of the TiO_2 CB edge, thus reducing the V_{OC}. Furthermore, aggregation on the TiO_2 surface occurs due to the formation of intermolecular hydrogen bonding, causing self-quenching of the dye excited state (Figure 1-19).[64, 68, 69]

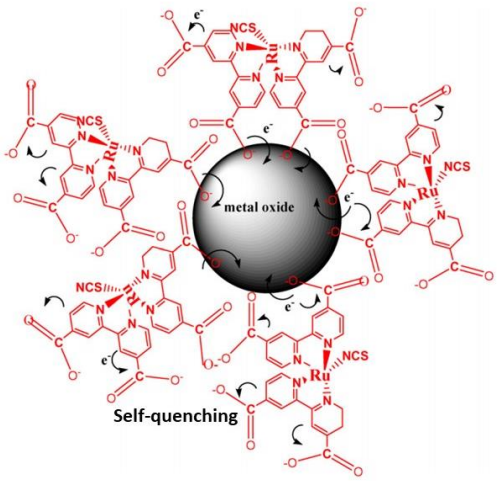

Figure 1-19 Representation of the inefficient electron injection into nanostructured metal oxide arising from aggregation and/or high degree of protonation in N3 dye. Adapted from Reference [64].

New generations of dyes arose from the modification of N3: the aggregation was suppressed adding amphiphilic alkyl chains, as in the case of Z907, while higher molar extinction coefficients and conjugation were obtained adding a thiophene moiety prior to the alkyl chain, as in C101 and C106, the latter differing from the former for the presence of a sulphur atom (Figure 1-

20A-C). As shown in Figure 1-20D, the V_{OC} increases from 0.720 V for N3 to 0.730 V when the alkyl chain is introduced in Z907, but it reaches 0.778 V when using C101. Nevertheless, the low values of FF and PCE for the DSSC equipped with Z907 are ascribable to the use of a gel electrolyte, which reduces the mobility of ions and, consequently, the dye regeneration.

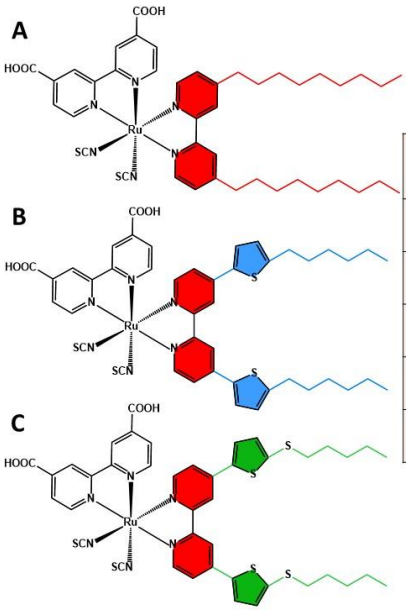

D

Dye	J_{SC} (mA/cm²)	V_{OC} (V)	FF	PCE (%)
N3	18.2	0.720	0.730	10 [a]
Black dye	20.53	0.720	0.704	10.4 [b]
Z907	12.5	0.730	0.670	6.1 [c]
C101	17.94	0.778	0.785	11.0 [d]
C106	19.2	0.776	0.760	11.29 [e]

[a] 10 µm of transparent TiO_2
[b] 18 µm of transparent TiO_2; Dye + taurochenodeoxycholic acid
[c] 10 µm of transparent TiO_2 + 4 µm scattering TiO_2; gel electrolyte
[d] 7 µm of transparent TiO_2 + 5 µm scattering TiO_2; Dye + chenodeoxycholic acid
[e] 7 µm of transparent TiO_2 + 5 µm scattering TiO_2; Dye + chenodeoxycholic acid

Figure 1-20 Molecular structures of ***A)*** *Z907 (cis-Bis(isothiocyanato)(2,2'-bipyridyl-4,4'-dicarboxylato)(4,4'-di-nonyl-2'-bipyridyl)ruthenium(II)),* ***B)*** *C101 (cis-Bis(isothiocyanato)(2,2'-bipyridyl-4,4'-dicarboxylato)(4,4'-bis(5-hexylthiophen-2-yl)-2,2' bipyridyl)ruthenium(II))****, C)*** *C106 (cis-Bis(isothiocyanato)(2,2'-bipyridyl-4,4'-dicarboxylato)(4,4'-bis(5-(hexylthio)thiophen-2-yl)-2,2'-bipyridyl)ruthenium(II)) dyes.* ***D)*** *Photovoltaic performance of DSSCs equipped with N3,[70] black dye,[71] Z907,[72] C101,[73] C106[74] dyes.*

Despite the good PV performance, the large-scale application of Ru-based sensitizers is limited by the difficult purification and low molar extinction in the visible range and the rarity and environmental hazard of the starting materials. For these reasons, metal-free organic sensitizers have attracted increasing interest, thanks to their versatile structure, tunable electronic properties and high absorption of visible light. Fast electron injection in the

TiO_2 CB is ensured by push-pull dyes, with a general structure donor-π bridge-acceptor (D-π-A): the D moiety plays the role of the light harvesting, which gives rise to an intramolecular charge transfer (ICT) through the bridge to the A.[43]

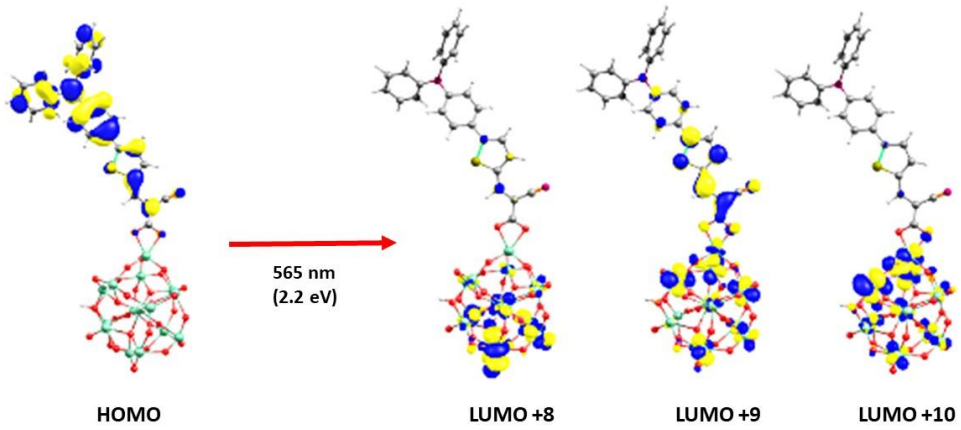

Figure 1-21. Active molecular orbitals (MOs) isosurfaces of the computed vertical transitions of Dye-$(TiO_2)_{15}$ systems at the TD-DFT/B3LYP theoretical level. The represented molecule has a triphenilamine donor, a thiophene bridge and a cyanoacrylic acid acceptor. Adapted from Reference [75].

Triarylamine derivatives were chosen as efficient donors, thanks to their electronic properties and planarity. The main advantage of D-π–A dyes is the localization of the molecular orbitals involved in the electronic transition: the HOMO is strongly localized on the donor moiety, while the LUMO is on the acceptor fragment. Furthermore, when the dye is adsorbed on the TiO_2, the orbitals accepting the transition are localized also on the TiO_2 cluster orbitals, demonstrating an efficient route for the electron injection (Figure 1-21).

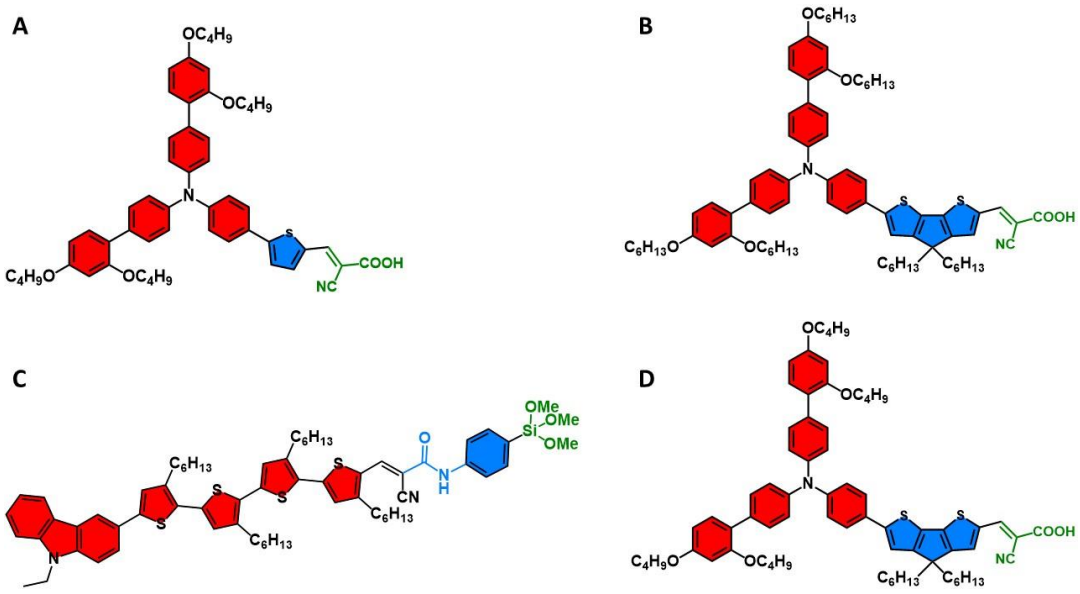

E

Dye	J_{SC} (mA/cm²)	V_{OC} (V)	FF	PCE (%)
D35	10.7	0.92	0.68	6.7 [a]
Y123	14.1	0.876	0.78	9.8 [b]
LEG4	10.9	0.85	0.74	6.78 [c]
ADEKA-1	15.6	1.036	0.774	12.5 [d]
ADEKA-1 + LEG4	18.36	1.013	0.770	14.3 [e]

[a] 12 µm transparent TiO_2, 3 µm scattering layer; $Co(bpy)_3^{3+/2+}$ electrolyte; CE: platinized FTO glass
[b] 4 µm transparent TiO_2, 4 µm scattering layer; $Co(bpy)_3^{3+/2+}$ electrolyte; CE: platinized FTO glass
[c] transparent TiO_2 + scattering layer (undeclared thickness); $Co(bpy)_3^{3+/2+}$ electrolyte; CE: electropolymerized PEDOT on FTO glass
[d] 4 µm transparent TiO_2, 2 µm semitransparent layer, 4 µm scattering layer; $Co(Cl\text{-}phen)_3^{3+/2+}$ electrolyte; CE: Pt-treated FTO
[e] 4 µm transparent TiO_2, 2 µm semitransparent layer, 4 µm scattering layer; $Co(phen)_3^{3+/2+}$ electrolyte; CE: graphene nanoplatelets+ gold-treated FTO glass

*Figure 1-22. Molecular structures of **A)** D35 (E)-3-(5-(4-(bis(2',4'-dibutoxy-[1,1'-biphenyl]-4-yl)amino)phenyl)thiophen-2-yl)-2-cyanoacrylic acid), **B)** Y123 (3-{6-{4-[bis(2',4'-dihexyloxybiphenyl-4-yl)amino-]phenyl}-4,4-dihexyl-cyclopenta-[2,1-b:3,4-b']dithiphene-2-yl}-2-cyanoacrylic acid), **C)** ADEKA-1 (2-Cyano-3-[5''-(9-Ethyl-9H-carbazol-3-yl)-3,4',4''-tri-n-hexyl-[2,2',5',2'']terthiophenyl-5- yl]trimethoxysilane, **D)** LEG4 (3-{6-{4-[bis(2',4'-dibutyloxybiphenyl-4-yl)amino-]phenyl}-4,4-dihexyl-cyclopenta-[2,1-b:3,4-b']dithiophene-2-yl}-2-cyanoacrylic acid). **E)** Photovoltaic performance of DSSCs equipped with D35,[76] Y123,[79] LEG4,[78] ADEKA-1[80] dyes and ADEKA-1 + LEG4[38] blend.*

In addition, various studies were performed to assess the best structure of these dyes. Strong electron donating substituents can induce a red shift of the absorption, improve the charge transfer ability and suppress the recombination. These requirements are matched using long chain bulky alkoxyl groups as substituents on an additional phenyl ring on the triarylamine, as in the case of D35 dye.[76, 77] The bridge plays an important role in favouring the ICT from D to A, thus thiophene, dithiophene, cyclopentadithiophene (CPDT) are among the most common and efficient ones.[76, 78] In order to accept electrons from D, the acceptor should be a good electron withdrawing and anchoring group, such as cyanoacrylic acid, carboxylic acid or alkoxysilane.[38, 43]

In conclusion, the main advantage of metal-free push-pull dyes relies in the high molar extinction values, which allow the reduction of the semiconducting film thickness, thus decreasing the charge recombination rate and the transport time, making them suitable for the application in combination with iodide-free redox mediators. The FoM of the most efficient DSSCs and the molecular structures of the D-π–A dyes used as sensitizers, such as D35, Y123, LEG4 and ADEKA-1, are shown in Figure 1-22.

Nevertheless, several other classes of sensitizers were developed, such as porphyrins,[81] phthalocyanins,[82] coumarins[83] and dyes extracted from natural products, such as anthocyanins, betalains, chlorophylls, carotenoids, etc.[32, 84, 85]

1.2.2.2 Electrolyte

Traditional DSSCs are fabricated using a solvent based iodide-triiodide (I^-/I_3^-) redox couple electrolyte. The most common solvent is acetonitrile (ACN), by virtue of its polarity, low viscosity and high stability, ensuring good diffusion of ions and efficient charge transfer. Its main drawback is the low

boiling point (78°C) which affects the long-term stability of the PV system, due to the solvent volatility and leakage. In order to overcome such problems, other common alternatives are methoxy acetonitrile, 3-methoxypropionitrile (MPN), N-methyl-2-pyrrolidone or γ-butyrolactone. As an alternative, solvent mixtures can be used, as in the case of the addition of valeronitrile (VN) to ACN.[86, 87] It has been demonstrated that various additives can play a role in determining the overall PCE: the addition of 4-*tert*-butylpyridine (TBP), which is able to adsorb on the bare TiO_2 surface through its nitrogen lone pair, induces an increase in V_{OC}, which is probably related to a shift of the TiO_2 CB edge to higher energies and the recombination suppression, consequently. On the other hand, positive charged species, such as Li^+ (frequently used as iodide counterion) and guanidinium (from another commonly used additive, guanidinium thiocyanate) give rise to a shift of the TiO_2 CB edge towards lower energies and a V_{OC} decrease.[40, 88–91] However, Li^+ is also able to intercalate into the semiconducting film, favouring the charge recombination suppression and the charge injection.[86] Thus, the appropriate balance in the additives concentration should be found for the studied PV system. Furthermore, aqueous electrolytes,[92] as well as quasi-solid, based on polymer gel or ionic liquids, and solid state ones, based on HTMs, such as copper halogen salts or molecules (*i.e.* spiro-OMeTAD {2,2′,7,7′-tetrakis(N,N′-di-*p*-methoxyphenylamine)-9,9′-spirobifluorene}) are gaining increasing interest.[86, 87]

Since 2010, various studies were carried out on the electrolyte composition, seeking for iodide-free redox mediators. The I^-/I_3^- redox couple is characterized by an inherent low redox potential, which limits the maximum V_{OC} that the DSSC could obtain. Furthermore, the energetic mismatch between its reduction potential and most of the Dye^+/Dye states usually leads to large voltage losses. Another disadvantage that should not be discarded

for large scale applications is the corrosive nature of this redox mediator towards most of the metals that usually find application in PV systems, such as Pt, Au, Ag, Cu, Al etc.[93–95] Various examples of iodide-free redox mediators span from alternative halogen redox couples, $SCN^-/(SCN)_3^-$, disulfide/thiolate (T^-/T_2) to cobalt and copper based complexes. In particular, rigid Cu complexes show excellent performance as HTMs in solid state DSSCs,[96, 97] while Co complexes, being characterized by more positive oxidation potentials compared to I^-/I_3^-, nonvolatility, optical transparency and non–corrosiveness, are able to ensure high PCE in liquid based DSSCs.

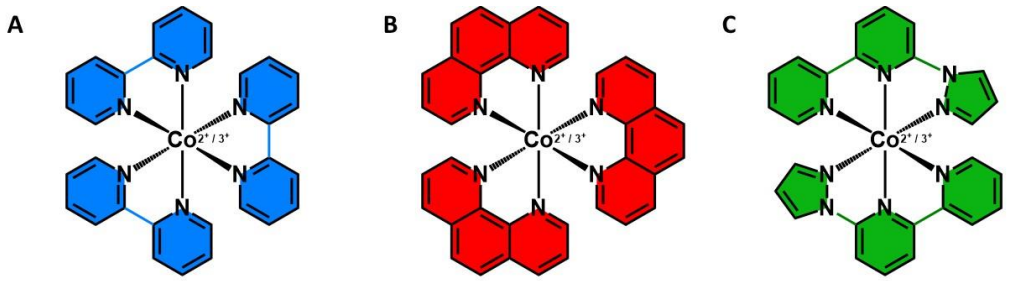

D

Redox couple	E_0 (V *vs* NHE)	J_{SC} (mA/cm²)	V_{OC} (V)	FF	PCE (%)
$Co(bpy)_3^{n+}$	0.57	9.4	0.89	0.57	4.8 [a]
$Co(phen)_3^{n+}$	0.62	8.2	0.91	0.51	3.8 [a]
$Co(bpy-pz)_2^{n+}$	0.86	5.3	1.02	0.68	3.6 [a]

[a] 13 µm transparent TiO_2 + scattering layer; D35 sensitizing dye; CE: platinized FTO glass

Figure 1-23 Chemical structures of the following cobalt complexes: ***A)*** $Co(bpy)_3^{n+}$ *(bpy = 2,2'-bipyridine),* ***B)*** $Co(phen)_3^{n+}$ *(phen= 1,10-phenanthroline),* ***C)*** $Co(bpy-pz)_3^{n+}$ *(bpy-pz = 6-(1H-pyrazol-1-yl)-2,2'-bipyridine).* ***D)*** *Reduction potentials and the photovoltaic performance of DSSCs equipped with these complexes as redox mediators.*[98]

Furthermore, the redox potential can be easily modulated varying the ligand nature (Figure 1-23), thus matching the oxidation potential of the sensitizer for an efficient dye regeneration.[86, 99] Nonetheless, according to Feldt *et al.* even if a more positive redox potential induces an higher V_{OC} value in a DSSC, as shown in Figure 1-23, the photocurrent and the overall PCE

decrease, probably due to lower regeneration and charge collection efficiencies. However, the same authors suggest that performing the measurements in different conditions, i.e. varying the Co complex concentration in the electrolytic solution, can simply greatly enhance the regeneration efficiency.[98] In addition, $\mathrm{Co(bpy-pz)_3^{n+}}$ was found to induce a PCE of 10.08 % when used in combination with Y123 dye in a DSSC with a photoanode composition of 5.6 and 5 µm of transparent TiO_2 and scattering layer, respectively, and a nanoporous poly(3,4-propylenedioxythiophene) (PEDOT) counter-electrode.[100]

1.2.2.3 Counter-electrode

A CE has a central role in a DSSCs, collecting charges from the external circuit and catalysing the reduction of the redox mediator. For this reason, the electrodic material should have good electrical conductivity, stability and catalytic activity, to ensure a fast reduction and an efficient suppression of the recombination reaction.[101, 102] Since the first appearance of DSSCs in literature, platinum has been the material of choice for CEs and the fabrication methods span from the thermal decomposition of precursor salts,[103] the electrochemical decomposition[104] and the chemical reduction[105] to the sputtering[106] and the casting and calcination of Pt NPs.[107] Nevertheless, the high cost and the lack of resistance to corrosion of Pt limit its application for long-term stable PV devices. Among all the candidates for the fabrication of Pt-free CEs, carbon based materials and conductive polymers play a major role, although other metal compounds and hybrid materials are extensively studied.[108, 109] Transition metal dichalcogenides, such as molybdenum disulfide (MoS_2) and tungsten disulfide (WS_2), demonstrated to have an excellent catalytic activity towards the reduction of

triiodide, and this activity is directly correlated to the number of active edges in the 2D structure. DSSCs equipped with edge-oriented WS_2 as CE exhibited a PCE of 8.85 % when associated with N719 dye and an iodide based electrolyte.[110] Graphene (GR) based materials can be used both in the case of iodide and iodide-free electrolytes. When graphene oxide is used in combination with graphene nanoplatelets (GO/GNPs) for the fabrication of CEs by spray-coating and successive reduction with hydrazine, the obtained DSSCs show similar performance to Pt based ones.[111] On the other hand, among the various conductive polymers, PEDOT exhibits high catalytic activity towards $Co(bpy)_3^{n+}$, giving rise to a PCE of 10.3%, because of the high surface area of the catalytic material and its low charge transfer resistance.[112] The SEM images of the above-mentioned materials deposited on FTO glass and the FoM of the DSSCs equipped with them are reported in Figure 1-24A-C.

A

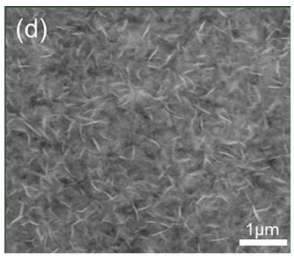

B

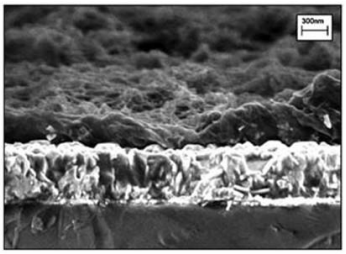

C

	Catalytic material	J_{SC} (mA/cm²)	V_{OC} (V)	FF	PCE (%)
1	Pt	15.34	0.778	0.60	7.20 [a]
	Edge oriented WS_2	16.12	0.789	0.69	8.85 [a]
2	Pt	15.2	0.901	0.66	9.0 [b]
	GO/GNPs 50:50	15.6	0.885	0.67	9.3 [b]
3	Pt	14.5	0.917	0.63	7.9 [c]
	PEDOT	15.9	0.91	0.71	10.3 [c]

[a] 10 µm transparent TiO_2 + 5 µm scattering layer; N719 dye; I^-/I_3^- electrolyte
[b] 5 µm transparent TiO_2 + 5 µm scattering layer; Y123 dye; $Co(bpy)_3^{n+}$ electrolyte
[c] 8 µm transparent TiO_2 + 4 µm scattering layer; Y123 dye; $Co(bpy)_3^{n+}$ electrolyte

Figure 1-24 SEM images of the following catalytic materials on FTO glass: ***A)*** *edge oriented tungsten disulfide (WS_2),* ***B)*** *cross-section of poly(3,4-propylenedioxythiophene) (PEDOT).* ***C)*** *Comparison of the photovoltaic performance of DSSCs equipped with 1) Pt and edge oriented WS_2, 2) Pt and GO/GNPs 50:50 and 3) Pt and PEDOT as CEs. Adapted from References* [110] *and* [111]*.*

In any case, the best PCE certified by NREL for liquid state DSSCs (12.3 %) was obtained employing a 5 + 5 µm thick PE consisting of a mesoporous and scattering TiO_2 layer, respectively, co-sensitized with two D-π-A molecules, a zinc porphyrin (YD2-o-C8) and a triphenylamine derivative (Y123), a $Co(bpy)_3^{n+}$ based electrolyte and a platinized FTO CE.[113, 114]

On the other hand, the most efficient DSSC reported in literature (PCE = 14.3 %, as shown in Figure 1-22E) was prepared by co-sensitization of the semiconducting film with ADEKA-1 and LEG4, $Co(phen)_2^{n+}$ electrolyte and Au/GR nanoplateles CE.[38]

1.2.3 Noble metal nanoparticles in DSSCs

The role of noble metal NPs in a PV system has been widely investigated, as a consequence of their characteristic LSPR and high surface area which can result in high catalytic activity. Among the various possible strategies to achieve better PV performance, as far as the PE is concerned, a balance between the light harvesting (LH) and the charge collection should be found: the light absorption can be enhanced increasing the semiconducting layer thickness, but this negatively affects the charge collection, since the electrons should travel along a larger path to reach the collecting electrode, causing voltage losses. For this reason, a viable alternative can be the improvement of LH in the dye low absorption regions, as shown in Figure 1-25 for N719 dye, whose absorption after 600 nm is very low. Dang *et al.* showed that adding noble metal NPs to TiO_2 the PCE can be enhanced, simply matching the LSPR with the dye low absorption region. In the case of N719, they found that multiple core-shell TiO_2-Au-TiO_2 (TAuT) NPs (TEM image in Figure 1-25B) can induce an increase in J_{SC} as a consequence of the increased LH and charge collection. Furthermore, since the plasmon

enhanced DSSCs reach optimal PCE at lower PE thickness, reduced voltage loss induced by reduced recombination gives rise to increased V_{OC}. (Figure 1-25E)[115] A similar behaviour can be observed when Ag@SiO_2 core@shell nanoprisms (33 nm SiO_2 shell, 70 nm total diameter, TEM image in Figure 1-25D) are embedded in TiO_2 for the PE fabrication: Gangishetty *et al.* showed that J_{SC}, V_{OC} and PCE increase with the addition of 0.05 % of these nanoprisms to the PE, compared to the DSSCs with bare N719 sensitized TiO_2, as a consequence of the LH enhancement up to 750 nm, as showed also by the higher IPCE in Figure 1-25 C.[116]

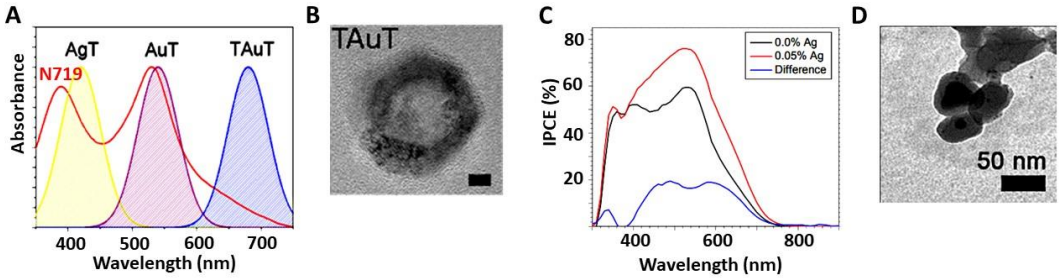

E

PE material (optimal thickness)	J_{SC} (mA/cm²)	V_{OC} (V)	FF	PCE (%)
1 TiO_2 (13.01 µm)	14.31	0.799	0.728	8.32
1 TiO_2-Au-TiO_2 (11.04 µm)	18.03	0.823	0.728	10.81
2 TiO_2 (8-10 µm)	11.2 ± 1.2	0.65 ± 0.01	0.757 ± 0.112	5.6 ± 0.6
2 TiO_2 + 0.05% Ag@SiO_2 (8-10 µm)	14.4 ± 1.4	0.70 ± 0.01	0.735 ± 0.09	7.4 ± 0.7

[a] N719 dye; I^-/I_3^- electrolyte; Pt CE
[b] N719 dye; I^-/I_3^- electrolyte; Pt CE

Figure 1-25 ***A)*** *Absorption spectrum on N719 dye (in red) and LSPR bands of TiO_2-Au-TiO_2 (TAuT, d_{core} ~15 nm, d_{Au} ~0-4 nm, d_T ~2 nm) NPs (in blue), Ag@TiO_2 (AgT, d_{core} ~15 nm, d_T ~2nm) NPs (in yellow) and Au@TiO_2 (AuT, d_{core} ~15 nm, d_T ~2 nm) NPs (in purple). The results obtained with AgT and AuT are not shown in this thesis.* ***B)*** *TEM image of TAuT NPs. The scale bar represents 5 nm.* ***C)*** *IPCE spectra of DSSCs prepared with N719 sensitized TiO_2 (in black) and with N719 sensitized TiO_2 with 0.05% embedded Ag@SiO_2 nanoprisms (in red). The difference spectrum is shown in blue line.* ***D)*** *TEM image of Ag@SiO_2 nanoprisms (33 nm SiO_2 shell, 70 nm total thickness) after sinterization.* ***E)*** *Comparison of the photovoltaic performance of DSSCs equipped with 1)TiO_2 and TAuT NPs, and 2) TiO_2 and TiO_2 + 0.05% Ag@SiO_2 as PE materials. Adapted from References* [115] *and* [116].

The application of noble metal NPs in DSSCs CE is still limited, although few examples are reported for the combination of Au NPs with GR-based

materials or bimetallic nanostructures. Due to the already discussed high corrosiveness of iodide-based electrolytes, Au NPs based CEs are reported in association with cobalt based redox mediators.

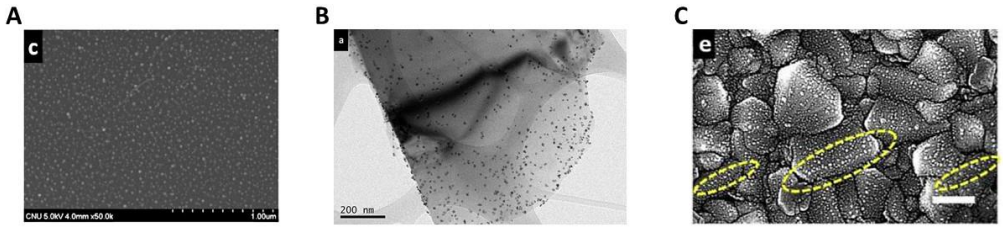

D

	CE material	J_{SC} (mA/cm²)	V_{OC} (V)	FF	PCE (%)
1	Pt	8.09 ± 0.12	0.3303 ± 0.0001	0.4912 ± 0.0026	1.45 ± 0.2 [a]
	Au NPs/rGO	7.27 ± 0.11	0.3552 ± 0.0025	0.5042 ± 0.0035	1.30 ± 0.01 [a]
2	Pt NPs	13.94	0.740	0.716	7.4 [b]
	$Pt_{0.5}Au_{0.5}$ NPs	14.66	0.745	0.730	8.0 [b]

[a] 12 µm transparent TiO_2 + 4 µm scattering layer; N719 dye; $Co(bpy)_3^{n+}$ electrolyte
[b] 14 µm transparent TiO_2 + 4 µm scattering layer; N719 dye; I^-/I_3^- electrolyte

Figure 1-26 ***A)*** *SEM and* ***B)*** *TEM images of the Au NPs/rGO nanohybrid prepared by Ar plasma reduction on FTO glass and TEM grid, respectively.* ***C)*** *SEM image of $Pt_{0.5}Au_{0.5}$ bimetallic NPs prepared by dry plasma reduction on FTO glass. The scale bar represents 200 nm.* ***D)*** *Comparison of the photovoltaic performance of DSSCs equipped with 1) Pt and Au NPs/rGO nanohybrid, and 2) Pt NPs and $Pt_{0.5}Au_{0.5}$ bimetallic NPs as CE materials. Adapted from References* [117] *and* [118]*.*

Dao *et al.* showed the *in situ* synthesis of Au NPs/rGO nanohybrid by consecutive drop-casting on FTO glass of a graphene oxide (GO) solution and $HAuCl_4$ precursor solution, followed by simultaneous reduction with Ar plasma, to obtain reduced graphene oxide (rGO) and Au NPs. SEM and TEM images of the nanohybrid are shown in Figure 1-26A-B. The obtained CEs are characterized by high surface area and low charge transfer resistance. However, as far as the PV performance of the fully assembled DSSCs are concerned, the overall PCE is very low also in the case of Pt CE, due to inefficient combination of $Co(bpy)_3^{n+}$ with N719 dye (Figure 1-26D).[117] Better results were obtained when AuPt bimetallic NPs were synthesized by dry

plasma reduction on FTO glass, after drop-casting of H_2PtCl_6 and $HAuCl_4$ mixed solution in 5:5 ratio. The obtained $Pt_{0.5}Au_{0.5}$ bimetallic NPs are shown in Figure 1-26C. The combination of Pt and Au is accompanied by higher catalytic activity and thus higher PCE.[118](Figure 1-26D)

Au mirror thin films (~ 50 nm) deposited by sputtering, in combination with GR nanoplatelets, were used for the fabrication of the most efficient DSSCs reported in literature:[80, 119] the addition of Au ensures higher PCE as a consequence of the enhanced J_{SC}, given by higher CE reflectivity, and lower charge transfer resistance, thus improving the FF.[120]

Notes: when not specified, the reported PCEs are measured under 1 SUN illumination (100 mW/cm^2).

1.3 Raman Scattering

The Raman scattering or Raman effect was reported for the first time by Chandrasekhara Venkata Raman in 1928.[121] This process involves the simultaneous emission of a photon when a molecule interacts with the incident light: Rayleigh scattering involves the emission of a photon with the same energy of the incident one, but a different direction and/or polarization, while, as far as the Raman effect is concerned, the energy of the scattered photon is different from the incident one, following the transition between rotational/vibrational levels. The two processes are illustrated in Figure 1-27A-B. Since the emission of the photon is instantaneous, there is not an actual absorption of the incident light causing an electronic transition, and for this reason the phenomenon is observed also when using light in the transparency region of the molecule. The phenomenon can be rationalized as the formation of a very short-lived complex between the incoming light and the molecular electron cloud, which is considerably smaller than the light

wavelength. The interaction is so fast that the nuclei do not have time to move appreciably and only a small temporary dipole is formed. Furthermore, the complex is not stable and the light is immediately released as scattered radiation.[122] In order to better understand and depict the processes, the absorption is usually described as causing the excitation to a virtual state, followed by the emission of light carrying the same (Rayleigh) or different energy (Raman) as the incident photons. (Figure 1-27C-D)

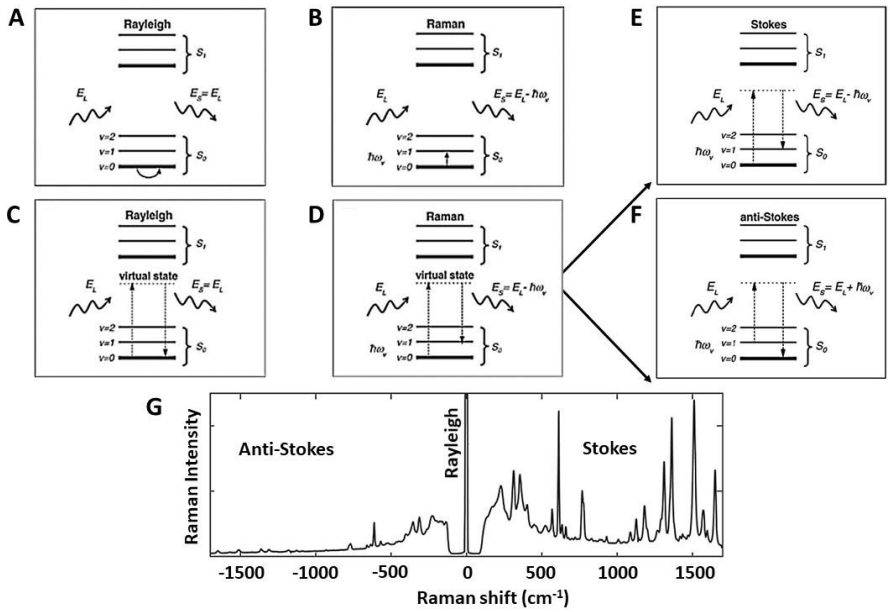

*Figure 1-27 Jablonski diagrams depicting the **A)** Rayleigh and **B)** Raman scattering processes. Alternatively, the **C)** Rayleigh and **D)** Raman scattering processes are presented showing the excitation to a virtual state, followed by the photon emission. Jablonski diagrams depicting the **E)** Stokes and **F)** anti-Stokes Raman scattering processes. **G)** Typical Raman spectrum of a Raman active molecule (Rhodamine 6G), showing several Raman peaks on the Stokes side and their (weaker) anti-Stokes counterparts. The spectrum was obtained using a 633 nm excitation laser line. Adapted from Reference [123].*

Furthermore, there are two possible Raman processes, named Stokes and anti-Stokes, according to the energy of the emitted photon. The former occurs when the molecule is excited from its vibrational ground state to the first vibrational excited state, so that the scattered photon energy is smaller

than the incident one for a quantity $\hbar\omega_v$, which corresponds to the energy difference between the two involved vibrational states. On the contrary, when the molecule is in a vibrational excited state (i.e. due to thermal excitation) and relaxes to the ground state, the emitted photon has an energy greater than the incident one for a quantity $\hbar\omega_v$, which corresponds to the energy difference between the vibrational states donating and accepting the transition. (Figure 1-27E-F)[123] When interpreting a Raman spectrum, the observed peaks are related to a molecular vibrational mode. Due to the selection rules, a vibration is Raman-active when it is accompanied by an anisotropic change in polarizability: the latter measures the deformability of a bond under the influence of an incident electromagnetic field, causing a temporary dipole. An example of Raman spectrum is shown in Figure 1-27G. When the energy of the incident photon matches the frequency of an electronic transition of the molecule (the intermediate virtual state coincides with a real electronic one), the phenomenon is known as resonant Raman scattering, which gives rise to an enhancement of the scattering efficiency of the molecule by factors between 10^2 and 10^6.[124]

As anticipated in Section 1.1.1, the Raman cross-section is defined as the effective area of a homogeneous incoming beam from which the molecule will scatter every photon. It depends on the power of the incident light and it relates the signal produced by a Raman scattering event. Compared to other optical processes, such as UV-absorption (~10^{-18} cm^2) or fluorescence (~10^{-19} cm^2), the Raman cross-section (~10^{-24} cm^2) is several orders of magnitude smaller.[125]

1.4 Surface-enhanced Raman scattering spectroscopy

An amplification of the Raman signal can be obtained using Surface-enhanced Raman scattering spectroscopy (SERS), which relies on the

interaction between light, molecules and metal nanostructures. The effect was observed and reported for the first time in 1974 by Fleischmann, who used Raman spectroscopy to study the formation of a monolayer of adsorbed pyridine molecules on the surface of a silver electrode: unexpectedly, the Raman spectrum of pyridine changed when it was examined in the proximity of the electrode and a strong ring stretching band appeared at 1025 cm^{-1}, which can be associated with the coordination of the metal through nitrogen.[126] The first attempts to rationalize this evidence were made in 1977 by Jeanmarie and Van Duyne and by Albrecht and Creighton, independently: they both recognized that the increased signal could not be explained by the increased surface area of the roughened electrode alone.[127, 128] Nowadays, two processes are considered fundamental to the SERS effect: the electromagnetic (EM) and the chemical (CM) mechanisms.

1.4.1.1 SERS enhancement mechanisms

SERS is observed for molecules on or nearby the surface of metallic nanostructures that can support LSPR, which act as SERS substrates.[129] The EM mechanism is schematically illustrated in Figure 1-28A. Elastic scattering of the incident field E_0 off a metal sphere, having a diameter smaller than the wavelength of the incoming electromagnetic field E_0, leads to a field enhancement by the additional component E_{LM}. The resulting incoming field $E_{in} = E_0 + E_{LM}$ induces a dipole moment μ_{ind} in the molecule. E_{in} and μ_{ind} are vectorial properties which are connected by the molecular polarizability tensor (α). The dipolar radiation emitted by the molecule (E_{DIP}), which is red-shifted with respect to the incident laser light in the case of Stokes scattering, undergoes an enhancement by the scattering component E_{SC} due to the presence of the metal sphere, so that the outcoming electric

field is given by: $E_{out} = E_{DIP} + E_{SC}$. Although the EM mechanism does not require the molecule in direct contact with the metal surface, it abruptly decreases as the distance, R, between the molecule and the metal surface increases $(1/R)^{-12}$. For spherical NPs, the EM mechanism provides SERS enhancement around 10^6-10^8. This value can be further increased to 10^9-10^{11} as a consequence of the molecules located in a hotspot, the gap region between two coupled NPs.[129–131] However, although classical electromagnetics predicts that enhancements should vary inversely with the square of the gap size, for gaps with dimensions significantly below 1 nm, quantum effects associated with electron tunneling between NPs become important, changing the dominant plasmon energies significantly, resulting in a reduction in the EM enhancement.[132]

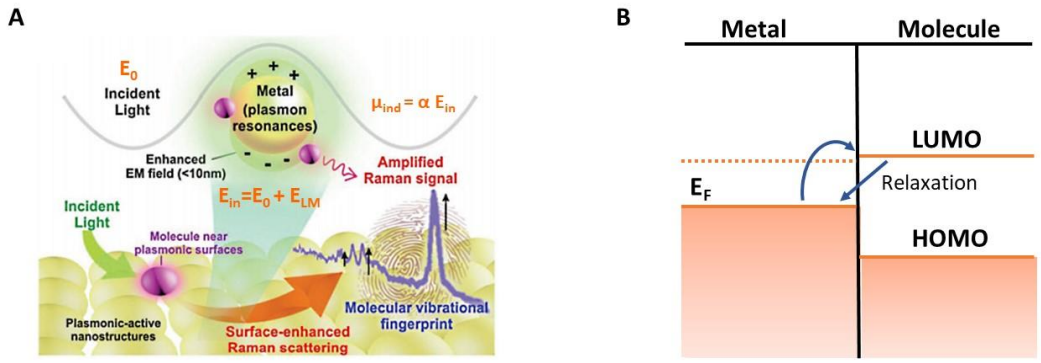

*Figure 1-28 Schematic representations of **A)** electromagnetic and **B)** chemical SERS enhancement mechanisms. Adapted from References [130] and [139].*

If we recall the basic formula for the induced dipolar moment, $\mu_{ind} = \alpha E_{in}$, the EM mechanism contributes through the increase in E_{in}, while SERS can also be enhanced up to 10^3-fold *via* a CM mechanism, which acts by means of the increase in electronic polarizability α. Charge transfer (CT) between the molecule in its electronic ground state and the metal can occur, thus changing the polarizability α and the Raman scattering cross-section of the molecule. The same effect occurs in coordination chemistry when ligand

molecules are bound to a metal center.[133] For CT to take place, the molecule must be chemisorbed on the metal substrate, so that the mechanism is usually referred to as a first-layer effect. The CM mechanism involves the interaction of the molecules with the surface plasmons, giving rise to charge-transfer excitation from the molecular HOMO levels to the nanoparticles Fermi-level or the inverse, from the Fermi-level to the LUMO levels of the molecule, as shown in Figure 1-28B. Basically, the enhancement is thought to proceed *via* new electronic states which arise from the formation of the bond between the analyte and the metal surface.[134–136] The combination of the two primary mechanisms contributes to the total enhancement. In 1997, Nie and Kneipp independently reported the single molecule detection of dyes in silver colloids, achieving Raman signal enhancement around 14 orders of magnitude greater than those obtained in the absence of a metal substrate.[137, 138]

1.4.1.2 SERS methods

SERS substrates can be divided into colloidal NPs, such as individual NPs or colloidal assemblies, or nanostructured platforms prepared through self-assembly of particles obtained by wet-chemical synthesis or lithographic approaches. In addition, the versatility of SERS derives from the possibility to detect various kind of analytes through different strategies: surface-affinity strategies, when the signal arises from the analyte itself; SERS tags strategies, when the signal arises from a Raman tag; and probe-mediated strategies, when the signal arises from a change in the probe upon the interaction with the analyte.

1.4.1.2.1 SERS substrates: Colloidal NPs

SERS efficiency dramatically differs as a function of NPs morphology and degree of aggregation. Usually, higher SERS efficiency is obtained when spherical NPs are partially aggregated, since junctions between the nanoparticles act as SERS hot-spots where large field enhancements occur, allowing detection down to the single molecule level. However, techniques allowing a fine control over aggregation are not yet perfect and thus the reproducibility of SERS signals is challenging. As an alternative way to generate hot-spots, anisotropy in metal NPs has been widely studied.[140]

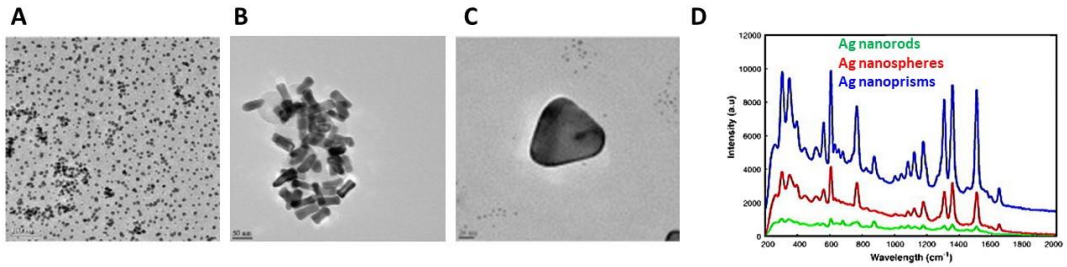

*Figure 1-29 TEM images of silver **A)** nanospheres, **B)** nanorods and **C)** nanoprism. **D)** SERS spectra of Rhodamine 6G (10^{-3} M) with silver nanospheres, nanorods and nanoprisms obtained using a 785 nm excitation laser line. The spectra were recorded in aqueous solutions under dilute conditions, with a similar number of NPs in all the samples (~$1.4 \times 10^{11}/cm^3$). Adapted from Reference* [141].

Tiwari *et al.* reported a comparative study of the SERS activity of Ag nanorods, nanoprisms and nanospheres, whose structure is shown in Figure 1-29A-C, using Rhodamine 6G. They evaluated that the SERS enhancement of Ag nanoprisms is considerably higher than Ag nanospheres and nanorods: in all cases a Ag-N stretching vibration is visible at ~235 cm^{-1}, confirming the contribution of the CM mechanism, while the higher efficiency of the Ag nanoprisms can be explained by the matching of their intense in plane dipole band, peaked at 646 nm, and the 785 nm excitation light (Figure 1-29D).[141]

Furthermore, the anisotropy of the structure probably ensures higher concentration of hot-spots.

1.4.1.2.2 SERS substrates: nanostructured platforms

Aiming to higher reproducibility, uniformity and long-term stability for real-life applications, immobilization of noble metal NPs on a solid support can be performed. Generally, the techniques for immobilization are bottom-up approaches, such as self-assembly of preformed metal NPs, or top-down approaches, such as lithography.[132] Lee *et al.* immobilized Au nanobipyramids on paper substrate by immersion in a colloidal solution for two days. It can be seen that both the transverse and longitudinal plasmon bands, corresponding to the two possible ways in which electrons can be polarized within these nanostructures, exhibit a blue shift compared to those observed in solution (Figure 1-30A), due to the change in dielectric constant of the surrounding medium. The Au bipyramids, homogeneously adsorbed on the paper substrate without aggregation (Figure 1-30B), are able to give SERS enhancement of the Raman peaks for trans-1,2-bis(4-pyridyl)ethane, ensuring its detection up to 0.5 nM, as shown in Figure 1-30C.[142]

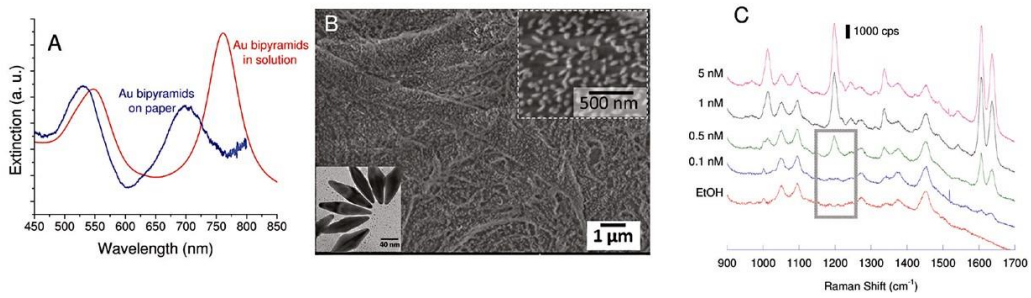

Figure 1-30 ***A)*** *Extinction spectra of gold bipyramid in solution (in red) and adsorbed on paper substrate (in blue).* ***B)*** *SEM images of gold bipyramids adsorbed on paper substrate.*

In the inset, TEM image of gold bipyramids. ***C)*** *SERS spectra obtained from the paper substrate adsorbed with gold bipyramids, exposed to different concentrations (5 - 0.1 nM) of trans-1,2-bis(4-pyridyl)ethane in ethanol, using a 785 nm excitation laser line. Adapted from Reference* [142]*.*

1.4.1.2.3 SERS hybrid materials

The possibility to further enhance SERS efficiency and its applications emerged with the discovery of graphene-enhanced Raman scattering, which is mainly dominated by the CM mechanism, *via* a ground-state chemical interaction between the π-electrons and the molecules. After this observation, various studies were performed on the combination of graphene with noble metal nanostructures to form graphene-based hybrid SERS platforms, whereby metallic NPs generally promote SERS *via* EM enhancement, while graphene mainly contributes *via* additional CM enhancement. Additionally, graphene can also improve SERS *via* a synergistic EM mechanism, deriving from the direct contact between graphene and a metal of higher work function (such as Au), which results in an electron flow from graphene to the Au surface through p-doping, contributing to higher EM enhancement from Au. [130, 143]

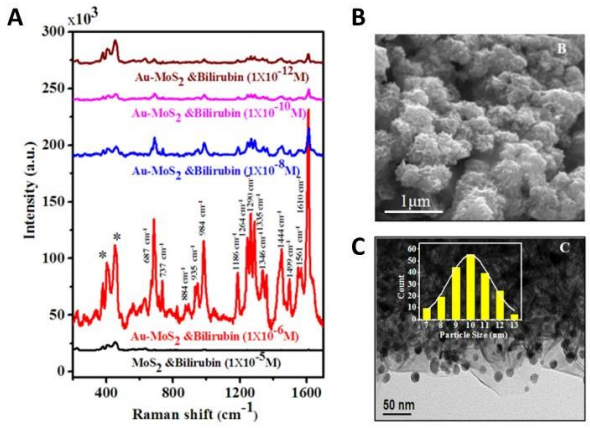

Figure 1-31 SERS spectra of bilirubin in water with concentration ranging from 10^{-5} M to 10^{-12} M, obtained using MoS_2 (black curve) and Au-MoS_2 substrates, using a 633 nm excitation laser line. Asterisk-marked peaks are from the MoS_2. ***B)*** *SEM image and* ***C)*** *TEM image of*

Au decorated MoS_2 nanoflowers. The average size of Au NPs is shown in the inset. Adapted from Reference [144].

Interestingly, diverse 2D materials beyond graphene, such as transition metal dichalcogenides and hexagonal boron nitride, nowadays find application in the fabrication of SERS hybrid materials. Singha *et al.* showed the detection of bilirubin in water in the range 10^{-5} M - 10^{-12} M through Au decorated MoS_2 nanoflowers (Figure 1-31A), obtained by reduction of $HAuCl_4$ in a MoS_2 nanoflowers solution. The SEM and TEM images of the hybrid material and the average size of the Au NPs are shown in Figure 1-31B-C.[144]

1.4.1.2.4 SERS affinity strategies

The simplest detection method relies on the affinity of a Raman active analyte for an unmodified SERS substrate, by means of electrostatic, van der Waals or covalent interactions, or using a “drop and dry” method, where a small amount of the sample solution is dropped onto a SERS-active substrate or they are mixed in solution before being dropped on a surface for the measurement and allowed to dry (Figure 1-32 A). As the solution evaporates, both the NPs and the analyte tend to concentrate, forming a ring structure on the surface, known as “coffee ring effect”, characterized by high concentration of the analyte and a great density of hotspots in the ring region.[145] Xu *et al.* used this method for the detection of polycyclic aromatic hydrocarbons using unfunctionalized Au NPs. In the case of pyrene, they obtained a detection limit of 0.5 µM (Figure 1-32 B), measuring the SERS spectra along the periphery of the coffee ring region. As shown in the SEM images and EDX analysis in Figure 1-32C, Au NPs are almost exclusively deposited on the periphery of the ring, whereas NaCl (residue of the Au NPs

synthesis) is localized in the middle region, followed by the bare silicon wafer in the center of the ring.[146]

Alternatively, Montes-García *et al.* showed an example of affinity strategy through functionalization (Figure 1-32D), demonstrating that a higher detection limit (5 nM) can be obtained fabricating a SERS substrate by Layer-by-Layer (LbL) assembly of Au NPs and ammonium pillar[5]arene (Figure 1-32E), a supramolecular species able to give rise to host-guest interactions with polycyclic aromatic hydrocarbons, such as pyrene. The SEM image in Figure 1-32 F shows the Au NPs/ammonium pillar[5]arene assembly on PDDA modified glass, obtained after two depositions. The SERS spectra recorded at different pyrene concentrations and the representative SERS mapping of its 594 cm^{-1} band at 0.1 μM are reported in Figure 1-32 G-H.[147]

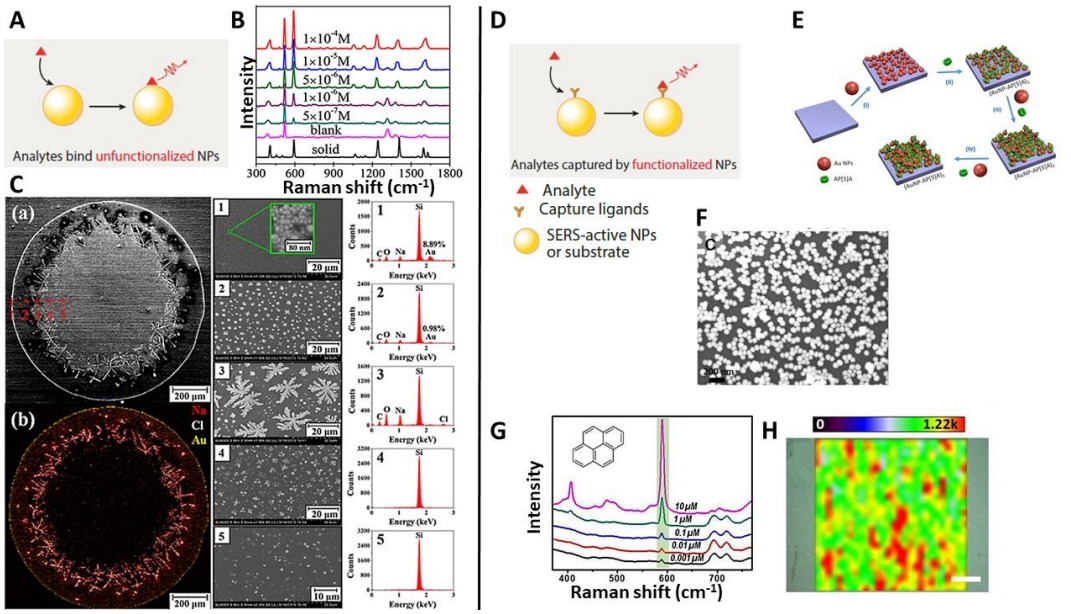

Figure 1-32 ***A)*** *Schematic representation of SERS affinity strategy with unfunctionalized substrate.* ***B)*** *Raman and SERS spectra of pyrene at different concentrations measured at the edge of the coffee ring pattern obtained using a 785 nm excitation laser line.* ***C)*** *(a) SEM image and (b) EDX analysis for the coffee ring pattern (red = Na; white = Cl; yellow = Au). The middle column shows the SEM images at higher magnification, and the right column is the EDX results for five points along the diameter of the coffee ring.* ***D)*** *Schematic representation of SERS affinity strategy with functionalized substrate.* ***E)*** *Schematic*

representation of the Layer-by-Layer assembly of Au NPs and ammonium pillar[5]arene. ***F)*** *SEM image of AuNPs/ammonium pillar[5]arene assemblies on PDDA modified glass obtained after two depositions.* ***G)*** *SERS spectra of pyrene at different concentrations (10 µM - 0.001 µM).* ***H)*** *SERS mappings obtained at 594 cm^{-1} with the optimized plasmonic substrate (two depositions of AuNPs/ammonium pillar[5]arene), obtained using a 785 nm excitation laser line (scale bar 20 µm). Adapted from References* [146] *and* [147]*.*

1.4.1.2.5 SERS tag strategies

SERS tag strategies rely on the signal from a Raman reporter attached to the NP, rather than using the intrinsic Raman response from the analyte itself. This approach makes SERS suitable for the indirect detection of analytes with low Raman cross-section. The Raman reporter provides the SERS tag with Raman fingerprinted signals. Optionally, a protective shell, made of silica or PEG can be added to enhance the particle stability. Specificity towards the analyte can be achieved by attaching a targeting ligand such as antibodies, aptamers, small molecules, or molecular imprinted polymers (Figure 1-33A). When exposed to the analyte, several changes can occur, causing a variation in the SERS intensity of the Raman reporter: immobilization or accumulation of the SERS-tags at specific locations, for example in SERS based imaging; clustering/ declustering of the SERS-tags, resulting in hot-spots turn-on (Figure 1-33B) or turn-off; and reduced or increased distance between the Raman reporter and the SERS-active substrate.[145, 148]

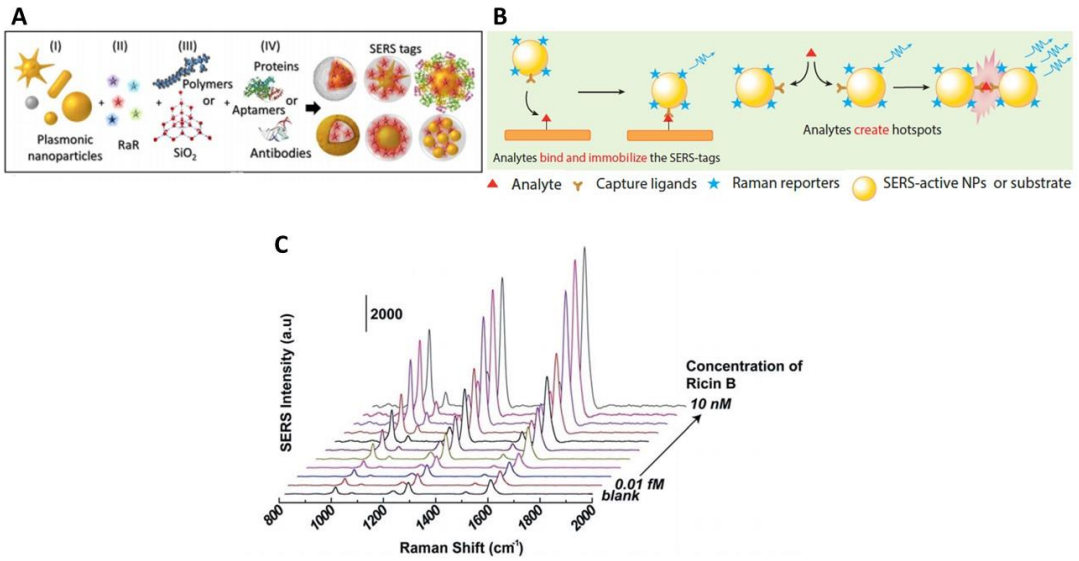

Figure 1-33 ***A)*** *Schematic representation of the key elements in SERS tag strategy: (i) plasmonic nanoparticles, (ii) Raman reporter molecules, (iii) protective shell and (iv) target ligands.* ***B)*** *Schematic representation of the SERS tag strategy occurring by hot-spot turn on.* ***C)*** *SERS spectra of Raman reporters with different concentrations of ricin B, obtained using a 785 nm excitation laser line. Adapted from References* [148], [145] *and* [149].

Zengin *et al.* used the SERS tag strategy for the detection of Ricin B, a protein toxin. Ag NPs were functionalized with a Raman reporter molecule, covered with a protective shell and then coated with ricin B aptamer. When this colloidal solution was dropped onto a silicon substrate coated with ricin B, hot-spots formed between adjacent ricin B aptamer modified Ag NPs and the Raman signal of the reporters could be greatly enhanced (Figure 1-33C).[149]

To conclude, some applications of direct and indirect SERS are presented in this thesis, although there are definitely several other materials and methodologies for SERS detection, considering that there is no universal measurement methodology and the choice is always determined by the application itself.

1.5 Chemiresistive sensing

Chemiresistors are a class of sensing devices whose functioning is based on the change in electrical resistance of the active material in the presence of the analyte of interest, upon application of a potential. Basically, the active sensing element has a double role, namely the receptor and the transducer: as a receptor, it is able to selectively interact with the analyte, while transducing the information into a macroscopically accessible signal, such as the change in resistance, in the case of chemiresistors. The active materials, deposited as a film between two metal electrodes, are usually metals, metal oxides, conductive polymers; more recently nanomaterials such as metal or semiconducting nanowires, carbon based nanomaterials (*i.e.* nanotubes, fullerenes, graphene) and semiconductive or metallic NPs have found application in this field, thanks to their small size and high surface-to-volume ratio providing several benefits for sensing over traditional bulk materials.[150–152] Among metallic NPs, the most used are electrostatically stabilized ones, prepared by Turkevich-like methods, which usually undergo post-synthetic modifications such as cross-linking reactions, and monolayer-protected clusters (MPCs), where metal NPs are stabilized by a self-assembled monolayer (SAM) of organomercaptans or organoamines. Sensing devices are usually fabricated by drop casting, LbL deposition or spin coating of the colloids on a pair of gold electrodes or interdigitated electrodes (IDEs) sputtered or evaporated on a Si/SiO_2 insulating substrate. The resistance exhibited by a 3D network of metal NPs connected by short molecules is given by the following equation:

$$R = R_0 e^{\beta L}$$

Where β is a pre-exponential factor that depends on the nature of bonding in the molecular backbone and L is the interparticle distance. It has been demonstrated that when L is lower than ~ 3 nm, the accepted mechanism for electron transfer is tunneling, while for higher values of L, hopping transport occurs, although the dominant mechanism strongly depends also on the nature of the bonding (Figure 1-34A).[152, 153]

When metal NPs coated with a molecular layer are deposited in the electrodic channel in a chemiresistor device, one among the three situations depicted in Figure 1-34B can occur: i) at an early stage, the distance between isolated NPs is so big that electron transfer is not allowed; ii) if the interconnected film grows, when the NP capacitance is sufficiently low that the electron transport barrier height is larger than kT, then a staircase behaviour may be observed in the I-V curve; iii) when percolation is achieved, the interparticle distance is so small that the number of pathways for electron transport is high enough to give a ohmic behaviour and a linear correlation between current and voltage is obtained.[150]

The most common application for chemiresistors is in the field of sensors for organic vapor and liquid-phase molecules and gases. Usually, in this kind of sensors, metal NPs provide the electrical conductivity, while the organic matrix provides a selective binding site for the adsorption of the analyte of interest, with an overall variation of the device resistance upon interaction with the analyte.

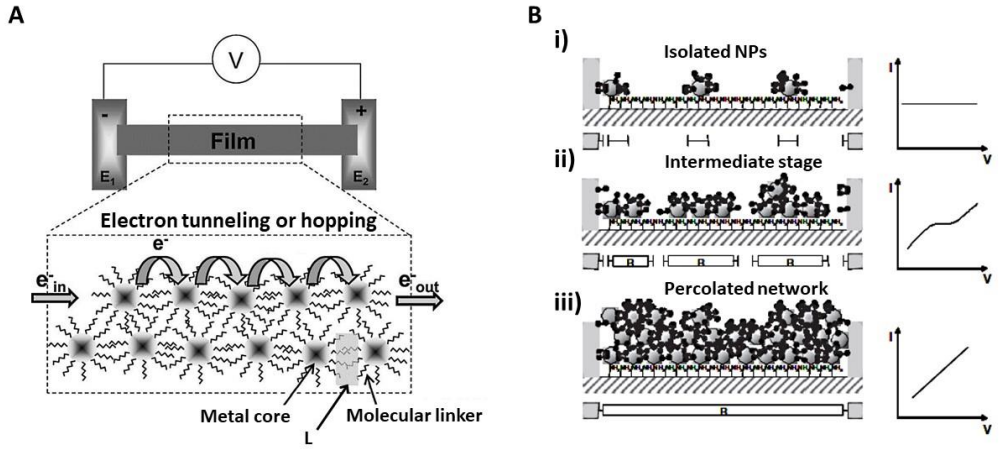

Figure 1-34. ***A)*** *Schematic representation of a chemiresistor where metal NPs interconnected by a molecular linker act as active material between two electrodes. Electron tunneling or hopping occurs when a voltage (V) is applied.* ***B)*** *Schematic representation of the conductive film growth in the chemiresistor electrodic channel, from i) isolated NPs, passing by ii) an intermediate stage to a iii) percolated network, and the corresponding I-V curves. Adapted from Reference* [150].

1.6 Heavy metals as water contaminants

The severe contamination of water resources due to the accumulation of hazardous heavy metals deriving from anthropogenic activities, such as several industrial, domestic and technological applications, represent a concerning risk to human health.[154] For this reason, various strategies have been developed for the detection and the removal of metal ions from aqueous systems. The most common categories of detection methods are: spectroscopic techniques, including atomic absorption spectroscopy, atomic emission spectroscopy, inductively coupled plasma mass spectrometry, which, despite the high sensitivity, are quite expensive and require laborious pre-treatment processes; electrochemical detection techniques, including amperometry, voltammetry, potentiometry, impedance measurement and coulometry, which allow relatively simple and fast analysis.[155] On the other hand, nowadays various detection methods exhibiting high limits of

detection, rely on the use of nanomaterials.[156] Among the various hazardous compounds that pollute the water resources, mercury ions (Hg^{2+}) have the tendency, once migrated in the food chain, to undergo bioaccumulation and biomagnification, resulting in a breakdown of the immune system, persistent damage to the central nervous system, cardiovascular collapse, acute renal failure, severe gastrointestinal damage and even death after acute exposure of humans.[157, 158] For this reason, the United States Environmental Protection Agency established that 10 nM (2 ppb) should be the maximum permitted level of Hg^{2+} in drinking water.[159]

2 Chapter 2

Fabrication and characterization of nanostructured gold counter electrodes for dye sensitized solar cells

In Section 1.2.3, the combination of noble metal NPs with 2D materials or the formation of bimetallic NPs as counter electrode materials for DSSCs has been shown, while the lack of examples of noble metal NPs as exclusive catalytic materials in this field has been highlighted.

In this thesis, the fabrication of gold nanostructured CEs by pulsed laser ablation (PLA) and a standard thermal decomposition method will be presented. The surface morphologies, optical properties, electrochemical behaviour, catalytic activity and the performance of the DSSCs equipped with the fabricated CEs will be presented, in comparison with standard Pt CEs. Conventionally, DSSC counter electrodes are Pt-based, but its high cost and lack of resistance to corrosion limit its application for the production of long-term stable PV devices. In addition, it was demonstrated that it is not the material of choice when push-pull dyes and iodide-free electrolytes are used. The main goal of the work is showing that a nanostructured gold layer deposited on a FTO glass by PLA can efficiently replace a standard platinum CE in DSSCs.

Large part of the work displayed in this chapter has been published.[160]

2.1 Materials and methods

2.1.1 Materials

Transparent conductive glasses were purchased from Dyesol (now Greatcellsolar), made of soda-lime glass coated with fluorine-doped tin oxide (FTO) with a sheet resistance of 7 Ω/sq. The transparent titania paste (Dyesol 18NR-T) and the scattering titania paste (WER 2-O Dyesol, 150–200 nm) were purchased from Dyesol (now Greatcellsolar). The dye Y123 (3-6-4-[bis(2',4'-dihexyloxybiphenyl-4-yl)amino-]phenyl-4,4-dihexyl-cyclopenta[2,1-b:3,4-b']dithiphene-2-yl-2-cyanoacrylic acid) and the cobalt complexes for electrolyte (DN-C09 and DN-C10) were purchased from Dyenamo. All the other chemicals employed in this study purchased from Sigma Aldrich were used without any further modification. Milli-Q water (18.2 MΩ) was used in all the preparations.

2.1.2 Photoanode preparation

Before use, glass substrates were cleaned by sonication with detergent and then washed with deionized water and ethanol. DSSCs equipped with four layers photoanodes were used in this work. A blocking underlayer was deposited on all photoanodes by immersion of the FTO glasses in 200 mL of a 40 mM $TiCl_4$ solution in deionized water at 70 °C for 30 min, followed by annealing at 500 °C for 30 min. The transparent active TiO_2 layer (TL) was deposited by screen printing method, using a frame with polyester fibers having 77:48 mesh size and Dyesol 18NR-T titania paste. To obtain thicker layers, the deposition was repeated several times drying the film at 125°C for 6 minutes. Scattering layers (SL) were deposited with the same screen printing method, but using WER 2-O Dyesol, containing titania particles with

sizes ranging from 150 to 200 nm. At this point, thermal treatment in air atmosphere was performed, using a temperature gradient program with five levels at 125 °C (6 min), 325 °C (5 min), 375 °C (5 min), 450 °C (15 min) and 500 °C (15 min). The upper blocking layer was deposited with the same procedure followed for the blocking underlayer.[161, 162] The as-prepared photoanode was immersed overnight in the dye solution (0.1 mM of Y123 dye and 5 mM of chenodeoxycholic acid in 4-*tert*-butanol: acetonitrile (1:1 *v/v*) solvent mixture) at room temperature in the dark. The molecular structure of the dye is shown in Figure 1-22B. The excess dye was rinsed with ethanol and the photoanode dried in an oven at 80 °C.

2.1.3 Counter electrode preparation

The standard reference platinum CE (named Pt) was prepared by deposition of a 5 mM solution of H_2PtCl_6 in 2-propanol by doctor blade technique, using one layer of adhesive tape (3 M Magic), followed by sinterization in air atmosphere using a temperature gradient program with the following levels: 125 °C (5 min), 180 °C (5 min), 235 °C (5 min) and 320 °C (30 min).[163]

A similar procedure was used for the preparation of the reference gold CE by thermal decomposition of a 5 mM solution of $HAuCl_4$ in 2-propanol, using the same temperature gradient program for sinterization.[164]

The deposition of Au NPs by PLA technique was performed by Dr. S. Trusso at the Istituto per i Processi Chimico Fisici (IPCF-CNR) in Messina. Au NPs were deposited onto the FTO glass surface by PLA technique using a KrF excimer laser (Compex 205 - Lambda Physik, $\lambda = 248$ nm, $\tau = 24$ ns). In order to avoid excessive damage of its surface, a pure gold target (99.9%, Kurt J. Lesker) was mounted on a rotating holder and then ablation was performed at the laser fluence of 2.0 Jcm^{-2} in a controlled Ar atmosphere at 100 Pa, using 30000 laser shots. Substrates (FTO glass and crystalline silicon, *c*-Si)

were positioned on a substrate holder located 35 mm far from the target. The process took place in a vacuum chamber with a residual pressure better than 1.0×10^{-4} Pa.

Nanostructured gold CE prepared by thermal decomposition and PLA will be referred to as Au therm and Au PLA, respectively.

2.1.4 Symmetrical dummy cells and DSSC assembly

The symmetrical dummy cells were fabricated using two identical CEs for each type of catalyst (Pt, Au therm and Au PLA); using a heat press machine they were sealed together in a sandwich type arrangement with the help of a sheet of Surlyn ionomer (25 μm, Du-Pont) cut as an O-ring. The gap between the electrodes was filled with the electrolytic solution, which was inserted in the pre-drilled pinhole using vacuum technique. The Co-based electrolytic solution had the following composition: 0.22 M $Co(bpy\text{-}pz)_2(PF_6)_2$, 0.05 M $Co(bpy\text{-}pz)_2(PF_6)_3$, 0.1 M $LiClO_4$, 0.2 M *tert*-butyl pyridine in 85:15 (*v/v*) acetonitrile : valeronitrile solvent mixture.[100] The DSSCs were prepared with the same method and configuration, but sealing together the PE and the CE.

2.1.5 Characterization

Scanning electron microscopy (SEM) images of the platinum and gold thin films on FTO substrates were acquired using a Zeiss Supra 40 field ion microscope. SEM characterization was performed by G. Compagnini and L. D'Urso at Università degli Studi di Catania. The NPs size was determined using ImageJ particle counting software.

UV–Vis absorption spectra were acquired with a home-made UV–Vis spectrometer (Avaspec 2048L spectrometer equipped with Avantes AvaLight-DHS Deuterium-Halogen light source).

Square wave voltammetric (SWV) measurements were performed in collaboration with Prof. Francesco Nastasi and Prof. F. Puntoriero at Università degli Studi di Messina. An Autolab PGSTAT 12 potentiostat/galvanostat instrument connected to an electrochemical cell with a three electrodes setup was used to perform SWV measurements at room temperature in dry and argon purged acetonitrile solution. A solution 5×10^{-4} M of $Co(bpy\text{-}pz)_2(PF_6)_3$ and 5×10^{-2} M of tetrabutylammonium hexafluorophosphate (supporting electrolyte) in acetonitrile was used for the SWV measurements. The ferrocene/ferrocinium redox couple was used as an internal reference (0.63 *vs* NHE in acetonitrile). In the measurement apparatus the working electrodes (WE, 1 cm^2 active area) were prepared by deposition of Pt and Au on FTO glasses with the previously described procedure, while a platinum and a silver wire were used as a counter and a reference electrode (RE), respectively. In the SWV analysis, a staircase voltage ramp is used to sweep the potential linearly between WE and RE and the current at the WE is measured. The latter is measured at the end of both the forward and reverse pulses, thus minimizing the capacitive current contribution. The difference between these two current values is plotted with respect to the potential of the WE. The following experimental conditions were used for all the measurements herein reported: 15 Hz square wave frequency, 0.01 V scan increment, 0.02 V amplitude, 5 s equilibration time and 0.15 V/s effective scan rate.

The photoanode thickness was measured using a surface profiler DektakXT (Bruker) equipped with a 2 μm radius diamond-tipped stylus. All the thickness values reported were recorded with the same experimental conditions: 524 μm vertical scan range, 6000 μm scan length and 1 mg stylus force. The thickness values were verified performing several measurements with different starting positions by translation of the sample.

Current-Voltage characteristic curves for the DSSCs and dummy cells were acquired with a Keythley 236 sourcemeter unit under AM 1.5 G sun illumination with a power of 100 mW cm^{-2} and in the dark, respectively.

2.2 Results and discussions

In the present section, a comparative study of the fabricated gold and platinum CEs will be presented, showing their surface morphologies, optical properties, electrochemical behaviour, catalytic activity and the performance of the DSSCs equipped with them.

2.2.1 Counter electrodes: morphology

SEM imaging was used to attain a morphological characterization of the prepared CEs. In the case of the deposition of H_2PtCl_6, the thermal decomposition induces the formation of Pt NPs of few nanometers in size on FTO glass (Figure 2-1A). When the image at higher magnification is observed in Figure 2-1B, isolated Pt NPs are clearly discernible besides the presence of nanoaggregates and coalesced particles between the valleys of the FTO grains, as shown also by Duong *et al.*.[165] In Figure 2-1C, the size distribution diagram shows that the majority of the isolated Pt NPs has an average size of 2.7 ± 1.7 nm, even though a large number of sub-nanometric particles are detectable in the SEM picture. Such a population is not included in the distribution function, given the impossible task of separating it from the image background noise. Furthermore, among the nanoaggregates, only the discernible NPs with a clear outline were included in the size estimation. When the same thermal decomposition method is applied to $HAuCl_4$, the formation of isolated Au NPs is clearly visible on the FTO-glass surface. In Figure 2-1D-E, it is possible to observe different shapes of NPs other than spherical ones, i.e. triangular, hexagonal, cubic and rod-shaped, as highlighted also by De la Garza *et al.* and Chew *et al.*:[166, 167] the thermal decomposition of $HAuCl_4$, in the absence of stabilizing agents, leads to the nucleation and growth of Au NPs, whose morphology is also influenced by

the presence of the FTO grains. The size distribution diagram shows that the obtained Au NPs have an average diameter of 13.2 ± 5.0 nm (Figure 2-1F). It is worth to note that the FTO surface is not completely covered by neither the Pt nor the Au NPs.

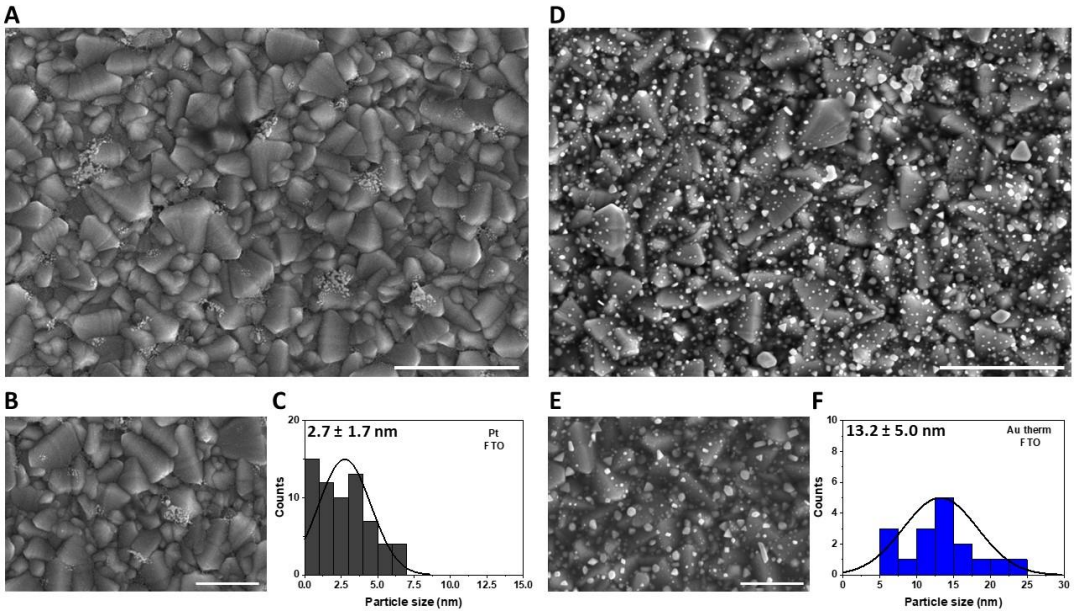

*Figure 2-1 SEM micrographs of Pt and Au thin films deposited on FTO glass by thermal decomposition of H_2PtCl_6 and $HAuCl_4$ at **A-D)** low and **B-E)** high magnification. The scale bars represent 1 µm and 500 nm at low and high magnification, respectively. Particle size distributions of the **C)** Pt and **F)** Au NPs deposited on FTO glass.*

A completely different surface morphology is observed for the gold thin films deposited by PLA. When the deposition is performed on *c*-Si substrate, isolated Au NPs are visible, with an average size of 23.0 ± 5.4 nm (Figure 2-2 B). Such a morphology is typical of noble metal NPs prepared by PLA, since a small portion of the target material is vaporized when the laser pulse hits it. This process results in the formation of a plasma plume that, driven by its internal pressure, starts to expand in the direction normal to the target surface. The presence of a background gas enables the particle growth.

Once deposited on the substrate surface, the NPs start to grow and, depending on the deposition time and the total number of laser pulses, different morphologies can be observed.[168–170]

However, when Au NPs deposit on FTO glass during the same ablation process, a different morphology is observed (Figure 2-2 D), probably driven by the interaction with the semiconducting substrate.[167] The FTO glass surface appears covered by a nearly percolated gold layer consisting of islands separated by narrow gaps. The SEM image at higher magnification and the size distribution diagram reveal that the nanostructured Au layer consists of coalesced Au NPs with an average size of 15.0 ± 4.3 nm (Figure 2-2E-F). Furthermore, the FTO grains appear completely covered by Au NPs, which still preserve the plasmonic properties.

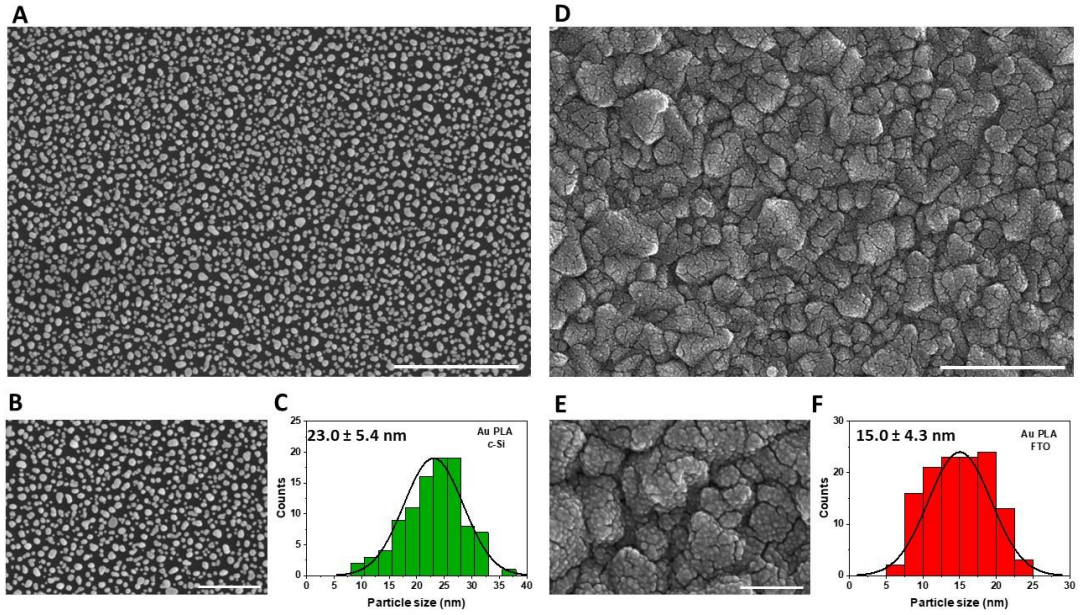

*Figure 2-2 SEM micrographs of Au thin films deposited by pulsed laser ablation on **A-B)** c-Si substrate and **D-E)** FTO glass at **A-D)** low and **B-E)** high magnification. The scale bars represent 1 µm and 500 nm, at low and high magnification, respectively. Particle size distributions of the Au NPs deposited on **C)** c-Si substrate and **F)** FTO glass.*

2.2.2 Counter electrodes: optical properties

As shown in 1.1.1, noble metal NPs are characterized by extraordinary optical properties arising from the interaction of light with the SPs, giving rise to LSPR, which strongly depends on the NPs size and shape, the nature of the metal and the dielectric function of the surrounding medium.

The different morphologies of the Au thin films prepared by thermal decomposition and PLA lead to very different optical properties of the obtained CEs. In Figure 2-3A, the extinction spectrum of the Au therm CE shows an absorption band in the visible range peaked at about 570 nm: the band appears red-shifted in comparison to the one of ~ 15 nm Au colloids in water (~ 520 nm).[21] The nanostructured gold layer deposited by PLA on FTO glass shows a broad band peaked at about 780 nm and extending up to 900 nm Figure 2-3A). Such a red-shift and broadening of the SPR band, with respect to the typical LSPR on isolated Au NPs, is a consequence of the formation of an interconnected network of NPs where dipole-dipole interactions play a major role.[171]

In Figure 2-3B the transmittance spectra of the prepared CEs are shown. Both Pt and Au CEs fabricated by thermal decomposition of H_2PtCl_6 and $HAuCl_4$, respectively, are characterized by high transmittance (~ 80-90 %) in the whole Vis-NIR region, while Au PLA CE exhibits ~ 50 % transmittance around 500 nm, while it considerably decreases at higher wavelengths as a consequence of the strong electronic coupling of Au NPs within the 2 D array shown in Figure 2-3 D-E.

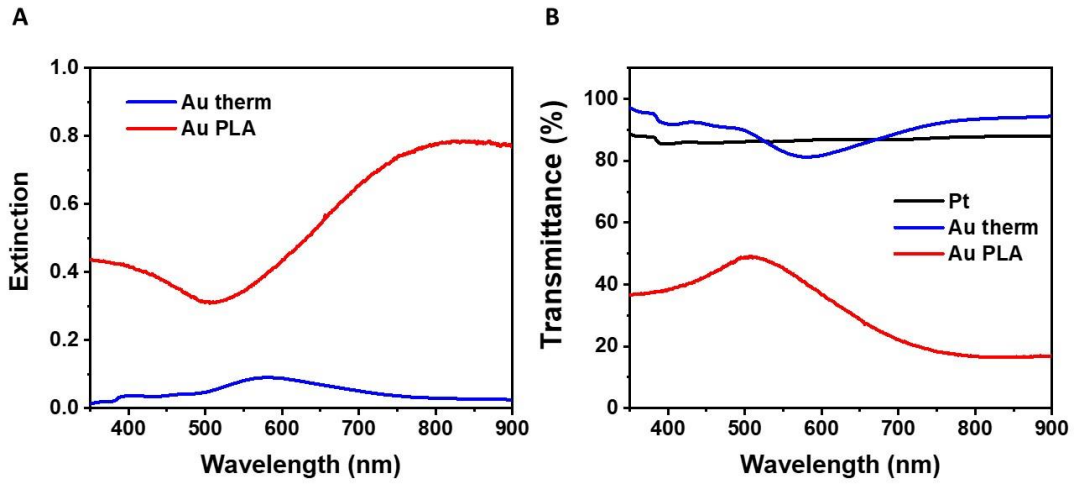

Figure 2-3 ***A)*** *UV-Vis extinction spectra of the Au thin films deposited on FTO glass by (blue) thermal decomposition of $HAuCl_4$ and (red) pulsed laser ablation.* ***B)*** *Transmittance spectra of the (black) Pt and (blue) Au thin films deposited on FTO glass by thermal decomposition and (red) pulsed laser ablation of gold.*

2.2.3 Counter electrodes: catalytic activity

Apart from conductivity, the main requirement of a CE in a DSSC is the catalytic activity towards the electrolyte regeneration. SWV was used to evaluate the different activity of the prepared Pt and Au CEs as catalysts towards the reduction of the electrolytic species $[Co(bpy\text{-}pz)_2]^{3+}$. This pulsed voltammetric technique was chosen due to its ability to ensure high speed of analysis and high sensitivity to the rate of electron transfer at the interface between the electrode and the electrolytic solution. This sensitivity derives from the possibility to differentiate the charging/capacitive current from the faraidic one, which is correlated to the redox reactions taking place at the WE surface.[172–175] To facilitate their interpretation, the obtained SW voltammograms will be reported in integral form. The results of SWV measurements of $[Co(bpy\text{-}pz)_2]^{3+}$ performed on the prepared Pt, Au therm and Au PLA electrodes are shown in Figure 2-4. First of all, it is possible to

notice that a redox reaction occurs at 0.86 V *vs* NHE[100] on the three WEs, thus demonstrating that they are all able to catalyse the electrolyte regeneration. Furthermore, this redox potential makes the chosen electrolyte suitable for the dye regeneration reaction, since an appropriate driving force (≥ 250 mV) should be ensured.[176–178] Indeed, the HOMO energy level of the Y123 dye adsorbed on TiO_2 is reported in literature as 1.08 V *vs* NHE.[179]

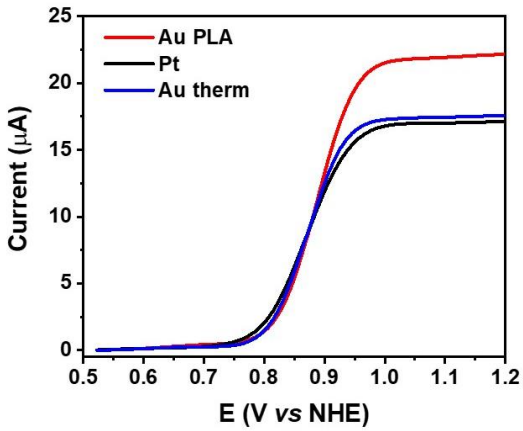

Figure 2-4 Square wave voltammetric measurements (reported in integral form) of Co(bpy-pz)$_2$(PF$_6$)$_3$ with (black) Pt, (blue) Au therm and (red) Au PLA as working electrodes.

In addition, another important information is given by the obtained voltammograms: the Au PLA electrode provides the highest value of current for the Co(II)/Co(III) redox reaction, compared to Au therm and Pt. In the studied system, high current values are directly related to high catalytic activity, which consists in a faster reduction of the oxidized form of the electrolyte. As demonstrated by Sapp *et al.,* cobalt complexes are characterized by higher affinity towards gold, compared to platinum.[180] However, the different current values obtained with Au PLA and Au therm can be rationalized as depending on the different surface morphology of the electrodes. When comparing Figure 2-1 D-E and Figure 2-2D-E it is clear

that the gold thin film deposited by PLA is able to cover the FTO grains, which are basically inactive towards the catalysis of the cobalt complex reduction. On the contrary, the thermal reduction of $HAuCl_4$ gives rise to isolated Au NPs, thus leaving the TCO layer exposed. The similar current values obtained with Au therm and Pt WEs could be rationalized taking into account the presumable higher superficial area of the obtained Pt NPs, ensuring the catalysis of a similar number of redox processes, despite the higher affinity of cobalt for gold.

Current-Voltage (I-V) curves were acquired for symmetrical dummy cells in the dark. Such measurements allow the calculation of the differential resistance of the cells, as the reciprocal slope ($\frac{\partial V}{\partial I}$) at low overpotentials around the equilibrium potential. High electron transfer kinetics leads to small differential resistance values. Carli *et al.* compared gold mirror electrodes prepared by top down methods and standard Pt ones and found that the redox couple Co(II)/Co(III) is usually characterized by a smaller differential resistance on Au CEs than on Pt ones.[181]

As shown in Figure 2-5A, the I-V curves in symmetrical dummy cells are characterized by a linear response at low overpotentials (-0.1; 0.1 V). In the same region, the differential resistance values are calculated as 45.31 Ω, 44.11 Ω, 129.37 Ω for Au PLA, Pt and Au therm, respectively (Table 2.1). Once again, the different surface morphology of the prepared gold electrodes can explain their different catalytic behaviour. The percolated gold layer, homogeneously covering the FTO grains as a consequence of the PLA, is able to ensure low differential resistance and high electron transfer kinetics in the electrolyte regeneration reaction. A similar resistance value is obtained with Pt CEs, probably depending on the high superficial area of the Pt NPs. On the contrary, Au therm CEs give rise to an approximately three times higher resistance value: despite the higher affinity of cobalt for gold compared to platinum, the low number of catalytic sites descending from the

very poor covering of the inactive FTO grains and the probably low superficial area of the Au thin film deposited by thermal decomposition of $HAuCl_4$, can explain the obtained resistance value.

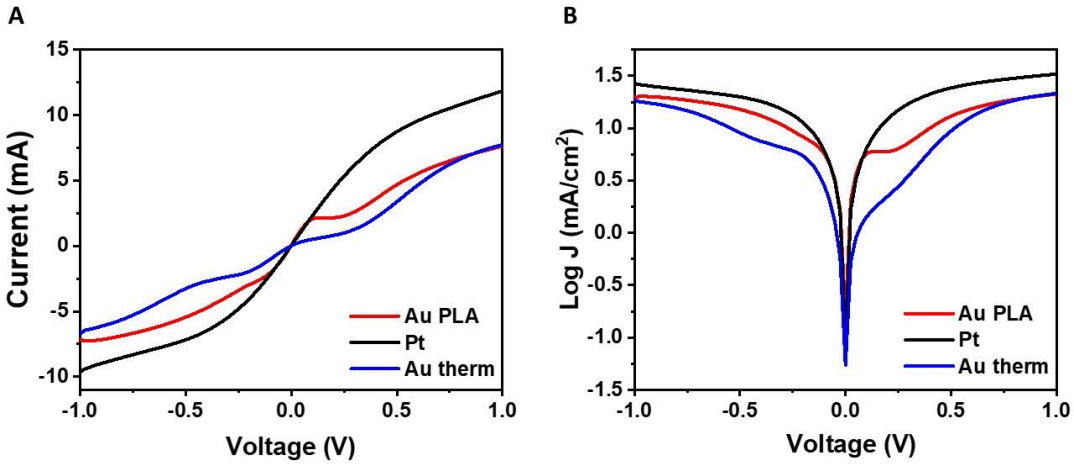

Figure 2-5 ***A)*** *I−V curves, and* ***B)*** *Tafel polarization plot of the symmetrical dummy cells (0.36 cm^2 active area) prepared with two identical Au PLA, Au therm and Pt CEs.*

In addition, the qualitative analysis of the Current-Voltage curves for symmetrical dummy cells suggests that the main limitation of the chosen Co(II)/Co(III) electrolytic couple arises from the diffusional transport, which makes it difficult to access a purely kinetically controlled regime. Indeed, the rate of diffusion decreases when bulky ligands such as (*bpy-pz*) are used, since they contribute to the increased hydrodynamical radius of the Co(II)/Co(III) complexes.

Tafel-polarization measurements are conducted to estimate the anodic and cathodic steady-state polarization diffusion-limited current (J_{lim}). The latter is the current at the intersection with the Y-axis in a Tafel polarization plot. It represents the current density when the charge transfer at the CE is limited by the maximum number of electrolyte ions which are able to diffuse on its surface.[182, 183] This suggests that there is a correlation between J_{lim} and the

ionic diffusion coefficient of Co(III), which is usually the limiting component. Indeed, this relation is given by Fick's law,

$$J_{lim} = \frac{2FD\lfloor Co^{3+} \rfloor_{bulk}}{L}$$

Where F is the Faraday constant, D is the diffusion coefficient of Co(III) and L is the thickness of the spacer.[184]

Counter electrode	Differential resistance (Ω)	Log J_{lim}	J_{lim} (mA/cm²)	Diffusion coefficient (cm²/s)
Pt	44.11	1.427	26.73	$6.93 \cdot 10^{-6}$
Au therm	129.37	1.269	18.57	$4.82 \cdot 10^{-6}$
Au PLA	45.31	1.301	19.99	$5.19 \cdot 10^{-6}$

Table 2-1. *Differential resistance, limiting current and diffusion coefficient of the investigated dummy cells (0.36 cm² active area) prepared with two identical Au PLA, Au therm and Pt CEs and $[Co(bpy\text{-}pz)_2]^{2+/3+}$.*

As seen in Figure 2-5B, all the fabricated CEs are able to give well developed limiting current density plateau, thus indicating that the diffusion limiting region was reached in the given potential range. Assuming that the concentration gradient across the thin layer cell is linear under stationary conditions, that the process is regenerative and that $L = 2.5 \cdot 10^{-3}$ cm, D was calculated according to the equation above (Table 2-1). The highest J_{lim} and D values are found for the Pt CE (26.73 mA/cm² and $6.93 \cdot 10^{-6}$ cm²/s, respectively), suggesting that it should ensure the highest catalytic activity in a DSSC configuration. However, these measurements confirm the previously reported electrochemical data, since Au PLA CE gives higher values of J_{lim} and D compared to Au therm. Nevertheless, the obtained D values are in good agreement with the ones reported in literature for structurally similar cobalt complexes.[181, 184]

2.2.4 DSSCs performance

The DSSC performance strongly depends on the characteristics of the PE, CE and electrolyte, as shown in Section 1.2. Y123 dye, whose structure is shown in Figure 1-22B was chosen as a sensitizer, considering its excellent characteristics as Ru-free dye.

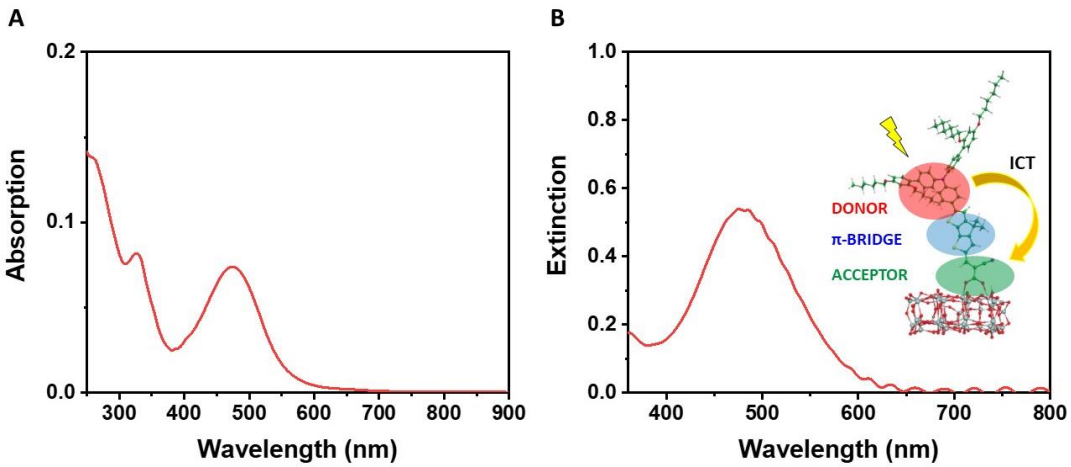

*Figure 2-6 UV-Vis **A)** absorption spectrum of a diluted Y123 solution in ethanol (~ 0.02 mM) and **B)** extinction spectrum of a TiO_2 photoanode (thickness 6 µm) sensitized with Y123. In the inset: schematic representation of the Y123 dye adsorbed on anatase TiO_2 (101) surface and the internal charge transfer (ICT) process.*

As an example, the absorption spectrum of a diluted Y123 solution in ethanol (~ 0.02 mM) is shown in Figure 2-6A, in comparison with the extinction one of a 6 µm thick TiO_2 PE sensitized with the same dye (Figure 2-6B). Two main absorption maxima are found at 474 and 326 nm with a hump at 260 nm, the first one arising from the internal charge transfer (ICT) between the donor and the acceptor moieties, through the π-bridge, while the second one can be ascribed to π→π* transitions.[185] The interaction of the cyanoacrylic acid anchoring group with TiO_2 generates a red-shift of the ICT absorption band for Y123 from 474 nm to 485 nm, when the dye is adsorbed on the

semiconducting layer. A schematic representation of the ICT process when the dye is adsorbed on the (101) surface of anatase TiO_2, through a bidendate linkage, is shown in the inset of Figure 2-6B.[186]

Since it was demonstrated that Y123 molecules are prone to aggregation by π-π stacking due to their planar geometry, de-aggregating agents, such as chenodeoxycholic acid (CDA), are usually added to the sensitizer solution: it has been demonstrated that CDA acts as a co-adsorbent on the TiO_2 surface, breaking the π-π stacking thus avoiding the self-quenching of the dye molecules. Even though the amount of adsorbed dye is lower, the presence of CDA does not affect the DSSC performance, while, on the contrary, aggregation of molecules reduces the photovoltaic efficiency.[187–189] Furthermore, CDA helps preventing the recombination of injected electrons with the oxidized form of the electrolyte (Figure 2-7).

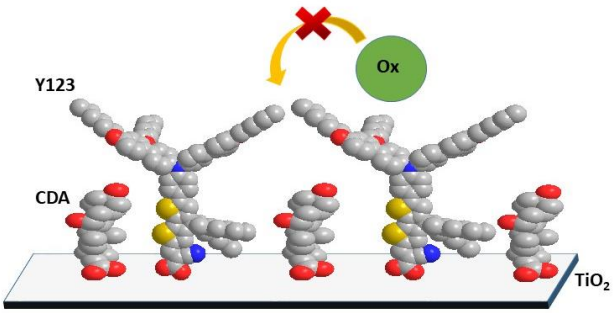

Figure 2-7 Schematic representation of the co-adsorption of Y123 dye and the de-aggregating agent, chenodeoxycholic acid (CDA), reducing the π-π stacking between the dye alkyl chains and the electron recombination with the oxidized form of the electrolyte (Ox).

As shown in Section 1.2.2.1, an adequate control over the dark current, arising from the recombination of electrons at the FTO-TiO_2 interface, can be obtained through the deposition of a blocking underlayer and upper layer, while higher light absorption arises from the use of a scattering layer.

The appropriate thickness of the PE was chosen by comparison of the photovoltaic performance of DSSCs equipped with a Pt CE and $[Co(bpy\text{-}pz)_2]^{2+/3+}$ based electrolyte. As shown in Section 1.2.2.2, cobalt based electrolytes are known to be the best choice when using push-pull dyes, such as Y123, but in this work the necessity to use iodide-free HTMs is driven also by the corrosiveness of iodide towards gold.[190] A comparative study was performed with three different PE structures, as schematized in Table 2-2 and Figure 2-8. The DSSCs equipped with one active TiO_2 layer and one scattering layer (2BL, 1TL, 1SL) are characterized by a poor J_{SC}, which can be ascribed to a low light harvesting efficiency, negatively affecting the FF and PCE.

When a thicker TiO_2 active layer (2BL, 2TL, 1SL) is used, the enhanced photocurrent is probably a consequence of the higher light harvesting efficiency deriving from the higher concentration of dye molecules adsorbed on the PE. In addition, the higher values of V_{OC} and FF deriving from low recombination rate, contribute to the enhancement of the PCE.

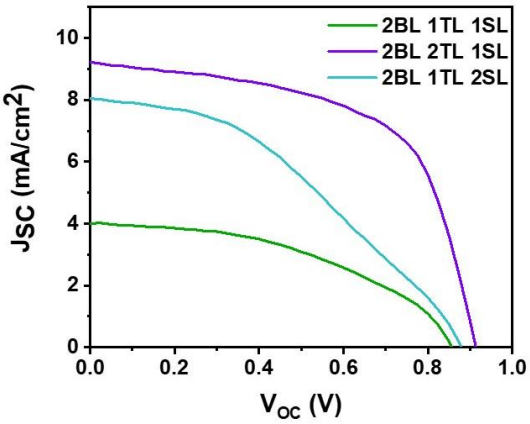

Figure 2-8 Photocurrent vs Voltage for DSSCs (0.181 cm² active area) equipped with different photoanodes: (green) 2BL 1TL 1SL, (violet) 2BL 2TL 1SL, (marine blue) 2BL 2TL 2SL. TL: transparent titania layer: SL: scattering layer. Data refer to the best performing cell for each photoelectrode.

PE structure	V_{OC} (V)	J_{SC} (mA/cm²)	FF	PCE (%)
2BL, 1TL, 1SL	0.87 ± 0.01	4.42 ± 0.70	0.43 ± 0.03	2.186 ± 0.53
2BL, 2TL, 1SL	0.92 ± 0.01	9.06 ± 0.21	0.57 ± 0.03	4.78 ± 0.32
2BL, 2TL, 2SL	0.88 ± 0.01	7.94 ± 0.13	0.39 ± 0.01	2.74 ± 0.02

Table 2-2. Photovoltaic parameters of the investigated DSSCs with Pt CE, $[Co(bpy\text{-}pz)_2]^{2+/3+}$ and different PEs. BL: blocking layer (underlayer + upper layer); TL: transparent titania layer: SL: scattering layer; Voc: open circuit voltage; Jsc: short circuit current; FF: fill factor; PCE: photocurrent efficiency. Average and standard deviation values are calculated over a set of 2 cells.

Indeed, the DSSC is characterized by a significantly lower value of R_S (364.96 Ω and 119.47 Ω for the PE with one and two active TiO_2 layers, respectively), which is related to the lower charge transfer resistance in the semiconducting material (Table 2-3).

PE structure	R_S (Ω)	R_{Sh} (Ω)
2BL, 1TL, 1SL	364.96	2190
2BL, 2TL, 1SL	119.47	2110
2BL, 2TL, 2SL	282.49	1450

Table 2-3. Series (R_S) and shunt (R_{Sh}) resistance values of the investigated DSSCs with Pt CE, $[Co(bpy\text{-}pz)_2]^{2+/3+}$ and different PEs. BL: blocking layer (underlayer + upper layer); TL: transparent titania layer: SL: scattering layer. Data refer to the best performing cell for each PE.

A thicker scattering layer (2BL, 2TL, 2SL) causes a dramatic decrease of the overall photovoltaic performance, which can be ascribed to a low dye regeneration: a thicker layer of big TiO_2 NPs hinders the flow of the electrolytic species, thus causing a reduction of V_{OC} and FF. Table 2-3 shows that the DSSC is also characterized by low R_{sh} (2110 Ω and 1450 Ω for the PE with one and two scattering layers, respectively) which usually

derives from the presence of alternative paths for the photo-generated current, since the charge transfer in a thicker film suffers from a longer charge transport distance to extract the excited electrons, as well as to recover the oxidized dye molecules.[191]

The comparative study on the CEs was then performed with the 2BL 2TL 1SL PE structure, to ensure the highest light harvesting efficiency (Figure 2-9).

CE material	V_{oc} (V)	J_{sc} (mA/cm²)	FF	R_s (Ω)	PCE (%)
Pt	0.92 ± 0.01	9.1 ± 0.2	0.57 ± 0.03	181.78 ± 33.31	4.8 ± 0.3
Au therm	0.90 ± 0.02	9.1 ± 0.6	0.52 ± 0.03	213.04 ± 26.82	4.3 ± 0.5
Au PLA	0.93 ± 0.01	9.1 ± 0.4	0.57 ± 0.03	168.12 ± 16.73	4.9 ± 0.1

Table 2-4. Photovoltaic parameters of the investigated DSSCs with Y123 sensitized 2BL 2TL 1SL photoelectrode, $[Co(bpy\text{-}pz)_2]^{2+/3+}$ and Pt, Au therm and Au PLA CEs on black background. Voc: open circuit voltage; Jsc: short circuit current; FF: fill factor; R_S: series resistance; PCE: photocurrent efficiency. Photoanode thickness: 8.5 µm. Average and standard deviation values are calculated over a set of 3 cells.

First of all, DSSCs equipped with Au therm CEs were studied in comparison with those equipped with Pt CEs. Although they are characterized by similar values of J_{SC} and V_{OC}, the main difference can be found in the FF (0.52 ± 0.03 and 0.57 ± 0.03 for Au therm and Pt, respectively) (Table 2-4). As shown in Section 1.2.1.4, the FF is significantly dependent on the series resistance: Au therm CEs exhibit higher values of R_S (213.04 ± 26.82 Ω and 181.78 ± 33.31 Ω for Au therm and Pt, respectively), probably descending from the non-adequate surface coverage of the FTO grains, which do not contribute to the electrolyte regeneration, as highlighted in Section 2.2.3. However, despite the common chemical nature of the catalyst, DSSCs equipped with Au PLA CEs exhibit higher values of V_{OC} (0.93 ± 0.01 V) and FF (0.57 ±

0.03), as well as lower R_S (168.12 ± 16.73 Ω), compared to Au therm. The different surface morphologies represent a valuable tool for data analysis: as shown in Figure 2-2 A-B, the electroactive Au NPs form a nearly percolated layer onto the FTO surface after PLA, thus ensuring the catalysis of a higher number of redox processes. Indeed, R_S is determined by various resistive events, among which resistance for electron transfer across the interface of electrolyte/CE can be found.[192]

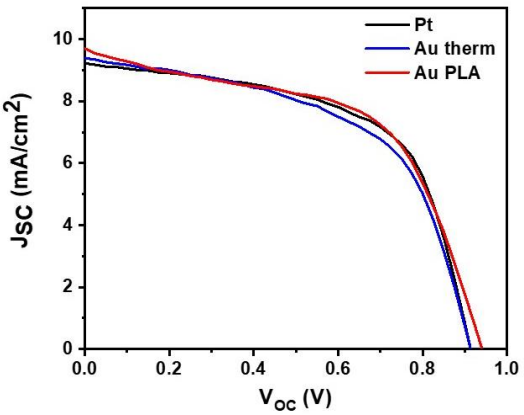

Figure 2-9 Photocurrent vs Voltage for DSSCs (0.181 cm² active area) equipped with different counter electrodes: (black) Pt, (blue) Au therm and (red) Au PLA. Data refer to the best performing cell for each CE.

In Table 2-5 2-5, the photovoltaic parameters of the same DSSCs equipped with Pt, Au therm and Au PLA CEs on white background are shown. In this case, all the DSSCs are characterized by higher values of J_{SC} and FF, thanks to the higher light harvesting deriving from the so-called albedo effect, *i.e.* the light diffused and reflected by the background.[193, 194] The difference found between the CEs prepared by thermal decomposition of H_2PtCl_6 or $HAuCl_4$ and Au PLA CE on black background, are significantly reduced by addition of a white background (Table 2-5). As a consequence of the higher transmittance of Pt and Au therm CEs (Figure 2-5B) more residual light is

impinging on the white background and can be reflected to re-cross the solar cell. In spite of the lower transmittance causing a lower average J_{SC}, DSSCs equipped with Au PLA CEs maintain high values of V_{OC} and FF, deriving from the higher catalytic activity towards the redox processes of the electrolyte.

CE material	V_{oc} (V)	J_{sc} (mA/cm^2)	FF	PCE (%)
Pt	0.94 ± 0.01	11.02 ± 0.89	0.60 ± 0.04	6.25 ± 0.98
Au therm	0.93 ± 0.02	10.99 ± 1.34	0.53 ± 0.06	5.42 ± 1.29
Au PLA	0.93 ± 0.01	9.67 ± 1.08	0.53 ± 0.09	4.84 ± 1.34

Table 2-5. Photovoltaic parameters of the investigated DSSCs with Y123 sensitized 2BL 2TL 1SL photoelectrode, $[Co(bpy\text{-}pz)_2]^{2+/3+}$ and Pt, Au therm and Au PLA CEs on white background. Voc: open circuit voltage; Jsc: short circuit current; FF: fill factor; PCE: photocurrent efficiency. Photoanode thickness: 8.5 µm. Average and standard deviation values are calculated over a set of 3 cells.

2.3 Conclusions

In summary, two novel fabrication methods of Pt-free CEs for DSSCs were developed. The nanostructured gold thin films deposited on FTO glass by thermal decomposition of $HAuCl_4$ and PLA were fully characterized. SEM investigation revealed that the different fabrication methods adopted give rise to completely different surface morphologies. The latter strongly affect the optical properties of the CEs, but also their electrochemical behaviour and catalytic activity, which were assessed by SWV and Current-Voltage and Tafel-polarization measurements in symmetrical dummy cells. Isolated Au NPs with different and irregular shapes were obtained by thermal decomposition of $HAuCl_4$. The process turned out to be an irreproducible and uncontrollable deposition technique, since it does not allow a good and homogenous covering of the TCO layer. On the contrary, PLA enables an accurate control over the surface morphology, which is characterized by the presence of a nearly percolated gold layer, homogeneously covering the FTO glass substrate. As a consequence of their surface morphology, higher catalytic activity was found by SWV for Au PLA CEs, as well as lower differential resistance in I-V measurements in symmetrical dummy cells and higher limiting current density and diffusion coefficient for Co(III) complex in Tafel-polarization measurements. The data were then confirmed by the Current-Voltage measurements in DSSCs equipped with the fabricated CEs. Au PLA CEs in DSSCs lead to better PV performance compared to the devices equipped with Au therm CEs. The PV parameters are comparable to the ones obtained with Pt CEs, thus demonstrating that Au PLA CEs can efficiently replace a standard platinum counter electrode in DSSCs.

It is worth noticing that PLA allows for the realization of nanostructures with very different surface morphologies, ranging from isolated nearly spherical NPs to percolated films, so that probably the DSSCs efficiency could be even improved by adopting different morphologies from the one investigated here, as well as different materials (*i.e.* silver or hybrid system, such as gold/rGO). PLA is a promising top-down method for the deposition of noble metal thin films, which could find application in the fabrication of transparent and high-performance Pt-free CEs for future large-scale applications not only in photovoltaics but even for others devices employing gold (or silver) for catalysis, sensing and opto-electronics.

3 Chapter 3

Fabrication and characterization of multiresponsive sensors based on noble metal nanoparticles

As highlighted in Sections 1.4 and 1.5, both SERS based and chemiresistive sensors are characterized by high versatility, high sensitivity, ease and low cost of fabrication. In addition, the extraordinary optical and electrical properties of noble metal NPs made them suitable as active materials for both the sensing techniques.

In this thesis, the synthesis of different types of noble metal NPs, spanning from citrate and tannic acid stabilized Ag NPs to Au@Ag core@shell NPs will be shown and their application for the fabrication of multiresponsive sensors will be presented. The optical properties, the morphological characterization by SEM and AFM, the SERS performance of the fabricated plasmonic sensing platforms, as well as the electrical response of chemiresistive sensors equipped with these NPs will be shown. Furthermore, the possible application of the fabricated plasmonic sensing platforms for the indirect SERS and chemiresistive detection of mercury ions in water will be demonstrated.

3.1 Materials and methods

3.1.1 Materials

Silver nitrate ($AgNO_3$), sodium citrate, tannic acid (TA), poly(diallyldimethylammonium chloride) (PDDA), poly(acrylic acid) (PAA), 1-naphthalenthiol (1-NAT), sodium borohydride ($NaBH_4$), hydrogen peroxide (H_2O_2, 28%), sulphuric acid (H_2SO_4, 98%), sodium chloride (NaCl), , lithium chloride (LiCl), calcium chloride ($CaCl_2$), magnesium chloride ($MgCl_2$), copper chloride dihydrate ($CuCl_2$ $2H_2O$), lead nitrate ($Pb(NO_3)_2$), cadmium chloride ($CdCl_2$) were purchased by Sigma Aldrich (now Merck); mercury nitrate ($Hg(NO_3)_2$) and potassium chloride (KCl) were purchased by Alfa Aesar and Fluka, respectively. Glass substrates were purchased by Knittel glass. Fraunhofer Organic Field Effect Transistors (OFET) chips, consisting of a Si/SiO_2 (230 nm thick) substrate with pre-patterned indium-tin oxide (ITO)/Au interdigitated electrodes (IDEs, 30 nm Au layer on 10 nm ITO adhesive layer) with channel length (L) of 2.5, 5, 10 and 20 µm were used as chemiresistive substrates. Milli-Q water (18.2 MΩ) was used in all the preparations.

3.1.2 Synthesis of tannic acid stabilized Ag NPs

Ag NPs were synthesized through a seeded-growth method, similar to the one showed in Section 1.1.2. The synthesis was performed in a three-neck round bottom flask with a condenser, to prevent solvent evaporation. A solution of sodium citrate (SC, 5 mM) and tannic acid (TA, 0.1 mM) in 150 mL of water was heated with a heating mantle under vigorous stirring. As soon as the solution started to boil, 1.5 mL of $AgNO_3$ (25 mM in water) were added: the nucleation of silver seeds occurred immediately with a clear

colour change from pale to bright yellow. Immediately after the seeds synthesis, Ag NPs growth was performed in the same vessel: 30 mL of seed solution were extracted, while 25 mL of water were added in the same flask. The temperature was lowered to 90°C in order to prevent further nucleation, instead favouring the seed growth. With a delay of 1 minute, 750 µL of SC (25 mM), 2.25 mL of TA (2.5 mM) and 1.5 mL of silver nitrate (25 mM) were added to the solution. After 30 minutes, 30 mL of solution were extracted and the remaining volume was used as seed solution for further NPs growth, performed with the same procedure. The extracted Ag NPs suspensions were purified by centrifugation to remove the excess TA and SC, with a speed depending on the NPs size. The size of the NPs was determined by STEM. Four different Ag NPs generations were used in this work, with sizes ranging from 15 to 43 nm. The 15 nm colloids were firstly centrifuged at 10414 g, and then twice at 8228 g. The suspension of 23 nm Ag NPs was centrifuged at 3214 g and then twice at 2057 g. The colloids containing 37 nm and 43 nm were centrifuged at 2057g and then twice at 804 g. In all cases, the centrifugation durations were 30 min and 45 min for the first and the second/third steps, respectively. After the purification, the NPs were redispersed in the same volume of water.[195]

3.1.3 Synthesis of citrate stabilized Ag NPs

Citrate stabilized Ag NPs were synthesized in a three neck round bottom flask, where 120 mL of a solution of SC (3.54 mM) and $NaBH_4$ (0.5 mM) were heated with a heating mantle to 60°C under vigorous stirring for 30 min. Then, 30 mL of $AgNO_3$ (2 mM) were added dropwise and subsequently the temperature of the obtained solution was raised to 90°C. Heating was continued for 20 min. The obtained Ag NPs were then used without any further treatment.[196]

3.1.4 Au NPs synthesis

The seeded-growth method described in Section 1.1.2 was adopted for the synthesis of Au NPs with sizes ranging from 18 nm to 54 nm. In a three neck round bottom flask, 150 mL of a solution of SC (2.2 mM) in Milli Q water were heated to boiling with a heating mantle for 15 min under vigorous stirring. In order to avoid the evaporation of the solvent, a condenser was used. Once the boiling point was reached, 1 mL of $HAuCl_4$ (25 mM) was added. The nucleation of Au seeds was evident from the colour change of the solution from yellow to grey and then soft pink in a 10 min timescale. At this point, the reaction mixture was cooled to 90°C to perform the NPs growth. In the same flask, 1 mL of $HAuCl_4$ (25 mM) was added and the process was repeated twice, with a reaction time of 30 min. After three additions, 55 mL of the obtained solution were extracted, while 53 mL of water were added in the same reaction vessel. Once the temperature reached again 90°C, 2 mL of SC (60 mM) were added and three consecutive addition of $HAuCl_4$ (25 mM) were performed with a delay of 30 min. The process was repeated until the desired Au NPs size was obtained. The synthesized Au NPs were then used without any further purification step.[21]

3.1.5 Au@Ag core@shell NPs synthesis

Au@Ag NPs (Au core 22 nm, Ag shell 5 nm) were synthesized through a seeded-growth method. In a two neck round bottom flask, 60 µL of L-ascorbic acid (100 mM) and 15 µL of $AgNO_3$ (100 mM) were added to 10 mL of 22 nm Au NPs and the obtained reaction mixture was stirred at room temperature for 30 min. At this point, 60 µL of L-ascorbic acid (100 mM) and 15 µL of $AgNO_3$ (100 mM) were added and the procedure was repeated 10 times in total. Au@Ag NPs with a size of 110 nm (Au core 54 nm, Ag shell 28 nm)

were synthesized with the same method, but using L-ascorbic acid 300 mM, $AgNO_3$ 300 mM and 54 nm Au NPs colloidal solution. The obtained Au@Ag NPs were then used without any further purification step.[197]

When not specified, the reported size of the synthesized NPs is the expected size estimated from their optical properties (maximum of the LSPR band), by comparison with the literature data.[195]

3.1.6 Substrates fabrication

Prior to use, the glass slides were cleaned by immersion in piranha solution (H_2O_2 : H_2SO_4 25:75) for 30 min and then thoroughly rinsed with water and stored in water until use. The chemiresistive substrates were instead cleaned by ultrasonication in acetone for 15 min, in order to solubilize the photoresist protection layer, followed by sonication in 2-propanol for 15 min.

The plasmonic platforms based on TA stabilized Ag NPs were prepared by two different methods. The first one consists on the functionalization of chemiresistive substrates with (3-aminopropyl)triethoxysilane (APTES, 43 mM in water) by immersion for 30 min, followed by immersion in TA acid stabilized Ag NPs colloidal solution for 3 h. Later, three LbL alternated depositions of tetra(ethylene glycol) dithiol (TEG, 5 mM in water) and TA stabilized Ag NPs were performed by immersion for 30 min and 3 h, respectively. For each deposition, new colloidal solutions were used. This substrate will be named APTES-Ag NPs-(TEG-Ag NPs)$_3$. The second method is the alternated electrostatic LbL deposition of TA stabilized Ag NPs and poly(diallyldimethylammonium) chloride (PDDA) on glass or chemiresistive substrates. The substrates were immersed in the cationic aqueous PDDA solution (1 mg/mL, 0.5 M NaCl) for 15 minutes and washed twice by immersion in water for 1 min. The procedure was repeated twice, alternating the immersion in a poly(acrylic acid) (PAA) solution (1 mg/mL, 0.5

M NaCl in water) with the immersion in PDDA solution. Finally, the substrates were immersed in the NPs colloidal solution and then rinsed with water and dried with a gentle stream of nitrogen. The procedure was repeated several times in order to obtain substrates with different Ag NPs loadings. For each deposition, new colloidal solutions were used. A schematic representation of the electrostatic LbL deposition is shown in Figure 3-1. Preliminary adhesion tests were performed with citrate stabilized Ag NPs and Au@Ag NPs by functionalization of chemiresistive substrates with APTES, followed by immersion in the colloidal solutions for 3 h.

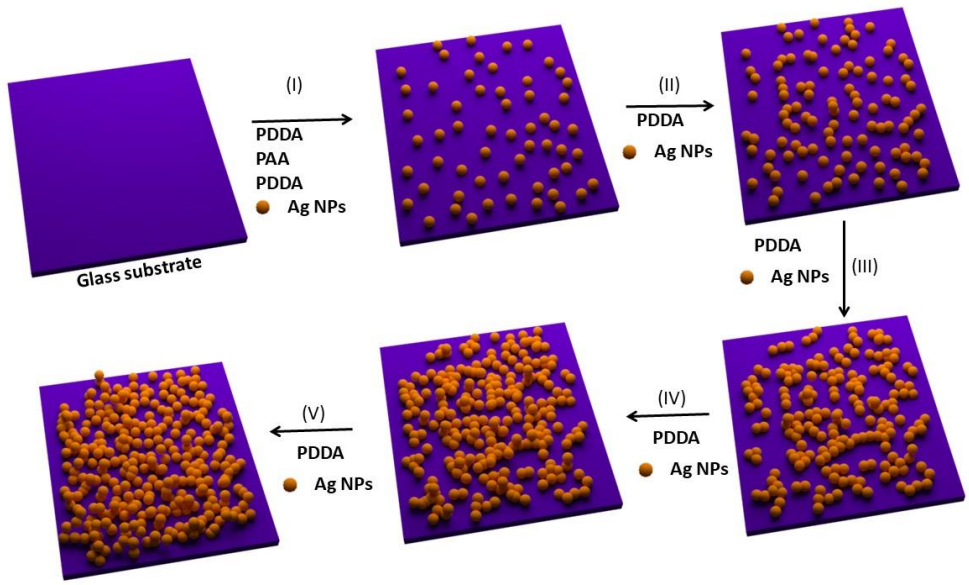

Figure 3-1 Schematic representation of the electrostatic layer-by-layer (LbL) deposition of polyelectrolytes and TA stabilized Ag NPs on glass substrate.

3.1.7 Optimization of the SERS substrates

The SERS performance of the plasmonic substrates prepared by alternated LbL deposition of Ag NPs and PDDA were investigated using 1-naphthalenthiol (1-NAT) as Raman reporter molecule. Prior to use, they were

immersed in a 50 mM $NaBH_4$ aqueous solution for 30 min to remove the stabilizing agents, then rinsed with water and N_2 dried. Subsequently, they were immersed in a 10^{-5} M 1-NAT aqueous solution overnight and then rinsed with water and N_2 dried.

3.1.8 Preparation of the Hg^{2+} solutions

A 10 mM stock solution of $Hg(NO_3)_2$ was prepared dissolving 17.13 mg in 5 mL of HCl pH 3 to avoid the precipitation of mercury oxide, while 1 mM and 1 µM solutions were prepared by dilution of the stock with water.

3.1.9 SERS and electrical detection of Hg^{2+} in water and selectivity

The plasmonic sensing platforms prepared with three alternate depositions of PDDA and Ag NPs 37 nm on glass substrate were immersed in a 1 mM or 1 µM $Hg(NO_3)_2$ solution for 1, 5 or 30 min, then rinsed with water and dried with nitrogen. When 1-NAT was employed, the plasmonic sensing platforms were previously treated with $NaBH_4$, as described in Section 3.1.7.

To perform electrical measurements, the plasmonic sensing platforms prepared with three alternate depositions of PDDA and Ag NPs 37 nm on chemiresistive substrates with IDEs (2.5 µm channel length) were immersed in a 1 mM aqueous solution of Li^+, Na^+, K^+, Ca^{2+}, Mg^{2+}, Cd^{2+}, Pb^{2+}, Cu^{2+} or Hg^{2+} for 30 min, then rinsed with water and dried with nitrogen.

3.1.10 Characterization

UV-Vis-NIR extinction spectra were recorded with a JASCO V-650 spectrophotometer. Scanning electron microscopy (SEM) and scanning transmission electron microscopy (STEM) characterization were performed using a FEI Quanta 250 FEG Scanning Electron Microscope, operating in

high vacuum mode with a pressure in 10^{-4} Pa range. A 10 µm gold coating was applied on non-conductive glass substrates prior to perform SEM. Atomic force microscopy (AFM) was performed in collaboration with Stefano Ippolito at Institut de Science et d'Ingénierie Supramoléculaires (ISIS) in Strasbourg. AFM images were acquired using a Bruker Dimension Icon microscope under ambient conditions in tapping mode. Bruker TESPA-V2 tips (spring constant k =42 N/m) were used to obtain images resolved by 512×512 or 1024×1024 pixels. SERS spectra were acquired with a Renishaw InVia Reflex system. The spectrograph used a high-resolution grating (2400 grooves cm^{-1}) with additional band-pass filter optics, a confocal microscope, and a 2D-CCD camera. A 532 nm laser excitation beam was employed for the excitation, using a 100x objective (N.A. 0.85, spatial resolution 0.46 μm^2), 0.02 mW maximum power and 1 s acquisition time. SERS images were obtained using a SERS point-mapping method, recording the spectra at each pixel of the image (40 µm × 40 μm^2, 2 µm step size, 441 points). Decodification of the SERS images was obtained using the characteristic peak intensity or area of TA (C-O stretching band centred at 1300 cm^{-1}) or 1-NAT (ring stretching band centred at 1367 cm^{-1}) using WiRE software V 4.2 (Renishaw, U.K.). The electrical characterization was performed in a probe station with a two-terminal configuration in ambient conditions, measuring the electrical resistance on chemiresistive substrates exposing IDEs with L= 2.5 µm, by means of a sourcemeter, Keithley 2636A/B, interfaced by LabTracer™ software, applying a 500 mV constant bias.

3.2 Results and discussions

3.2.1 Noble metal NPs synthesis and their optical properties in solution

Citrate stabilized Ag NPs were synthesized using a combination of a strong and a mild reducing agents, namely $NaBH_4$ and SC, and with an accurate control over the temperature. The first reduction step occurs at 60°C, when $NaBH_4$ induces the fast formation of small Ag nuclei, while SC passivates their surface, preventing agglomeration. In the second phase, the remaining SC induces the reduction of more Ag^+ ions on the surface of the already formed NPs. As far as the optical properties are concerned, the synthesized Ag NPs are characterized by a sharp LSPR band peaked at 416 nm, which is consistent with a diameter of around 50 nm, by comparison with the data reported by Agnihotri *et al*. (Figure 3-2).[196]

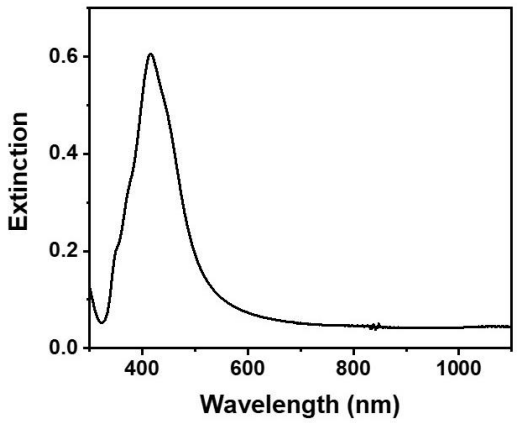

Figure 3-2 UV-Vis-NIR extinction spectrum of the synthesized citrate stabilized Ag NPs dispersed in water.

For the synthesis of TA stabilized Ag NPs with diameters ranging from 15 to 125 nm, silver nitrate was employed as silver precursor, while SC and TA were chosen as reducing agents and stabilizers. TA is a mixed gallotannin, whose structure consists of a central glucose core, linked to gallic acid esters. Its main applications derive from its antioxidant nature, since it is able to reduce serum cholesterol and triglycerides. In the synthesis of Ag NPs, TA

plays a dual role, since it is able to reduce Ag^+ ions through the oxidation of hydroxyl groups to the quinone form, while stabilizing the formed Ag NPs.[198] In this seeded-growth method, following the nucleation of Ag seeds, the main factors influencing the NPs growth rate are the temperature, the ratio between the concentration of Ag seeds present in solution and the silver precursor injected, as well as the TA concentration. Altogether, the method allows a precise control over the nanoparticle's size between 15 and 125 nm, leading to the growth of long-term stable and highly monodisperse NPs, thus avoiding the nucleation of new Ag nuclei.[195]

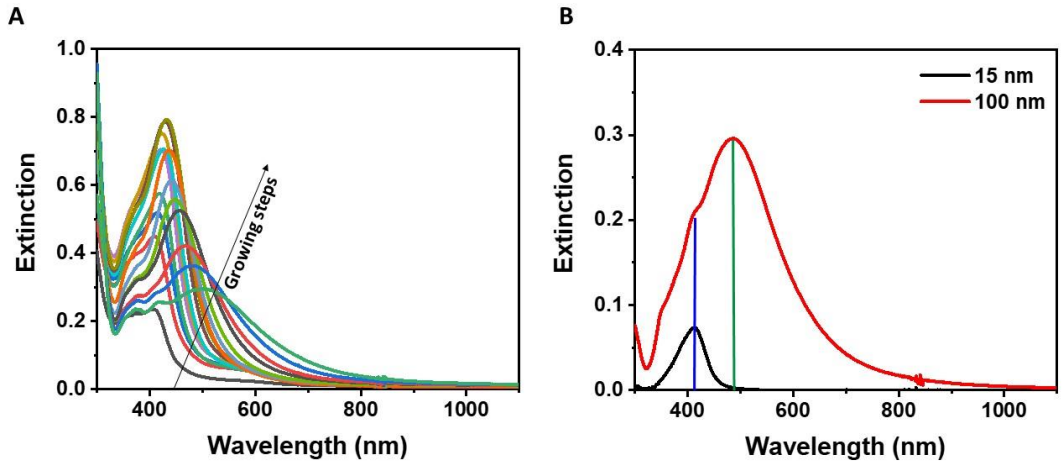

Figure 3-3 ***A)*** *UV-Vis-NIR extinction spectra of the synthesized tannic acid stabilized Ag NPs dispersed in water, with sizes ranging from 15 to 125 nm.* ***B)*** *UV-Vis-NIR extinction spectra of tannic acid stabilized Ag seeds (15 nm) and 100 nm Ag NPs after centrifugation. The blue and green lines indicate the position of the dipolar and quadrupolar bands, respectively for 100 nm Ag NPs.*

The UV-Vis-NIR extinction spectra of the obtained Ag NPs colloids are shown in Figure 3-3A. As the NPs size increases, it is possible to observe a red shift of the main dipolar LSPR band, starting from 408 nm for 15 nm Ag NPs. Furthermore, when the diameter is higher than 50 nm, a new band appears at shorter wavelengths, due to the quadrupole component of the plasmon resonance.[199] The position of the dipolar and quadrupolar bands are highlighted in Figure 3-3B, for colloidal solutions of 25 and 100 nm Ag NPs

after centrifugation. In addition, these extinction spectra show that the optical properties are retained after the purification steps.

STEM was used to determine the size of four generations of TA stabilized Ag NPs, which were then used in the SERS sensing platforms optimization. The results are shown in the Appendix.

To synthesize Au NPs, a seeded-growth method was adopted, using SC as both reducing agent and stabilizer. The method allows the synthesis of highly monodisperse and stable Au NPs, thanks to the accurate control over temperature and number of Au atoms added in every growth step. Indeed, after the synthesis of Au seeds, the subsequent growth steps were carried at 90°C in order to favour growth against secondary nucleation and, besides, avoid the Ostwald ripening process (dissolving of smaller particles, whose atoms are received by bigger ones, causing size polidispersity).[21] The UV-Vis-NIR spectra of the gold colloids in the 18 - 54 size range exhibit a well-defined LSPR band, which is peaked at 522 nm for the Au seeds, while it is red shifted at every growth step; furthermore, the increasing absorbance is a proof of the deposition of Au on the preformed seeds (Figure 3-4).

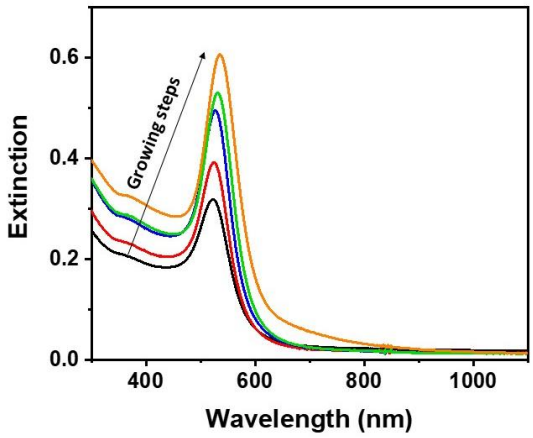

Figure 3-4 UV-Vis-NIR spectra of the synthesized Au NPs dispersed in water, with sizes ranging from 18 to 54 nm.

The prepared Au NPs were used for the synthesis of Au@Ag core@shell NPs. The chosen method is based on the reduction of Ag^+ ions on the surface of the pre-synthesized Au NPs in the presence of L-ascorbic acid. By using a mild reducing agent and controlling the concentration and the rate of addition of $AgNO_3$ it was possible to avoid the nucleation of free-standing Ag NPs.[200] The Ag shell growth on Au cores comes with a blue shift of the Au NPs LSPR band and the appearance of a new one at around 400 nm: the two bands merge after 5 additions of $AgNO_3$ when 22 nm Au core was used (Figure 3-5A), but not when 110 nm Au@Ag NPs were formed (Figure 3-5B). Furthermore, the presence of a Ag shell is clear from the formation of an absorption minimum at around 320 nm, which is inherent to Ag dielectric properties.[201]

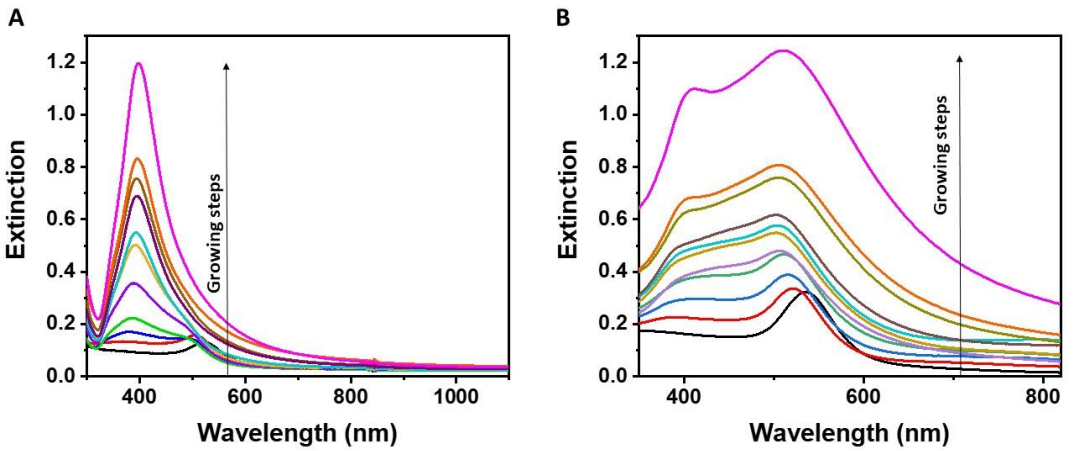

*Figure 3-5 UV-Vis-NIR spectra of the synthesized **A)** 32 nm Au@Ag core@shell NPs, starting from a 22 nm Au core (black spectrum) and **B)** 110 nm Au@Ag core@shell NPs, starting from a 54 nm Au core (black spectrum), dispersed in water.*

3.2.2 Chemiresistive sensing platforms: fabrication and morphology

The chemiresistive sensing platforms were prepared with a procedure similar to the one of Squillaci *et al.*, who deposited a 3D Au NPs network on pre-

patterned Si/SiO_2 substrates exposing Au IDEs by a two-step approach based on the preliminary formation of a chemisorbed SAM of TEG, followed by drop-casting of a Au NPs-TEG solution.[202] Being a dithiol, TEG was chosen due to its potential ability to cross-link NPs *via* the formation of Ag-S bonds at both its ends.[203] In the present work, instead of the TEG SAM, a preliminary APTES layer was deposited on the surface of a clean chemiresistive substrate, followed by its immersion in noble metal NPs colloidal solutions. In the case of citrate stabilized Ag NPs, a non-ordered assembly of NPs and a very low degree of deposition in the electrodic channel can be observed in Figure 3-6A. Furthermore, Figure 3-6B highlights the presence of particles with various shape besides the nanospheres, such as nanorods and triangular nanoplates.

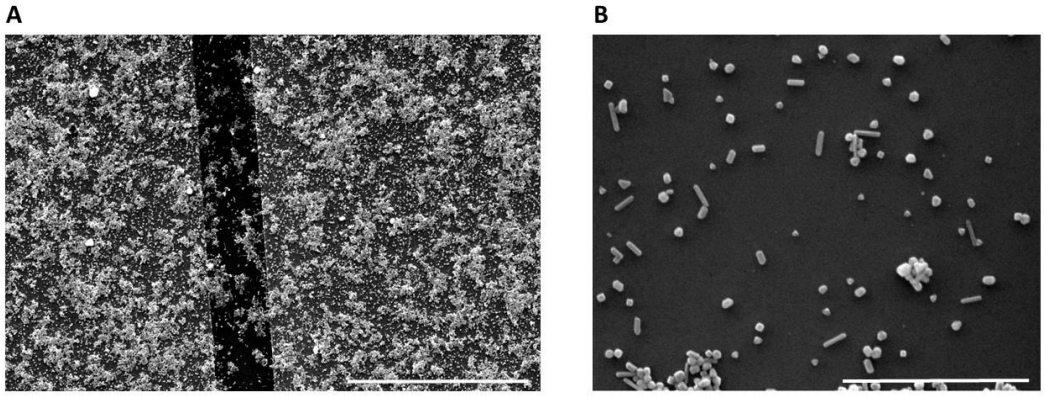

*Figure 3-6 SEM images of the TEG-citrate stabilized Ag NPs network on chemiresistive substrates exposing gold IDEs (L= 2.5 µm) at **A)** low and **B)** high magnification, showing the formation of nanoparticles, nanorods and triangular nanoplates. The scale bars represent 5 and 1 µm, respectively.*

On the contrary, TA stabilized Ag NPs (37 nm) exhibited a completely different behaviour. As shown in Figure 3-7A, a very low surface coverage is achieved when APTES-functionalized chemiresistive substrates are immersed in the colloidal solution. In order to assess the causes, a second functionalization step was performed by three consecutive alternate LbL

depositions of TEG and Ag NPs: the procedure did not allow the deposition of new Ag NPs, probably due to the inability of TEG to act as a linker for the NPs, which may be still covered by tannic acid, even after the purification. The SEM image of the APTES-Ag NPs-(TEG-Ag NPs)$_3$ on chemiresistive substrates is shown in Figure 3-7B.

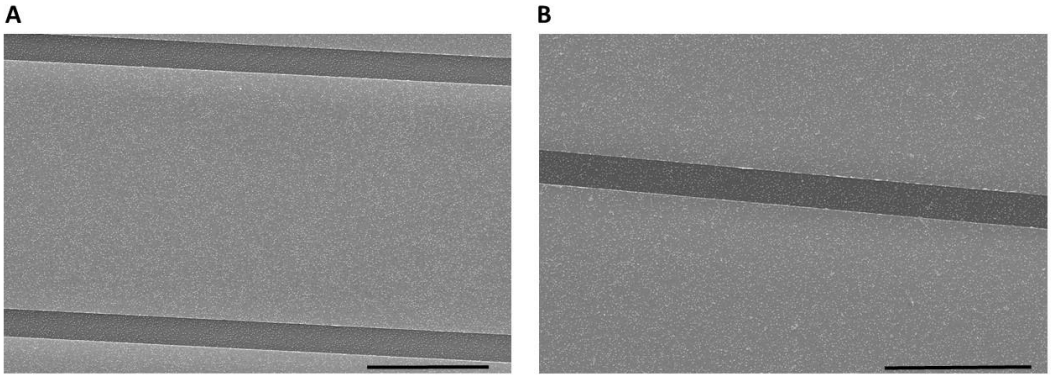

Figure 3-7 ***A)*** *SEM images of the APTES-tannic acid stabilized Ag NPs network and* ***B)*** *APTES-Ag NPs-(TEG-Ag NPs)$_3$ on chemiresistive substrates exposing gold IDEs (L= 2.5 µm). The scale bars represent 10 µm.*

Au@Ag NPs were deposited on APTES-functionalized chemiresistive substrates. When using Au@Ag NPs with a size of 32 nm it is possible to observe the coalescence of adiacent NPs, probably due to the removal of the very thin Ag shell (Figure 3-8A). Whereas, 110 nm Au@Ag NPs formed big aggregates covering very large areas of the electrode, as shown in Figure 3-8B. In both cases, the Ag shell was probably too thin (5 and 28 nm, respectively), thus undergoing oxidation during the substrate fabrication. For this reason, the prepared chemiresistive sensing platforms seem to be not suitable for the desired sensing applications.

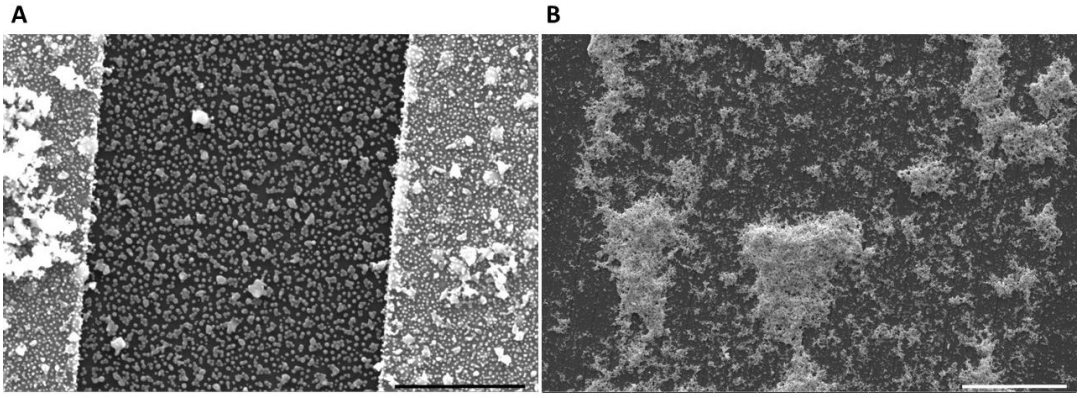

*Figure 3-8 SEM images of the Au@Ag NPs network on APTES functionalized chemiresistive substrates exposing gold IDEs (L= 2.5 µm) with **A)** 32 nm and **B)** 110 nm core@shell NPs. The scale bar represents 1 and 100 µm, respectively.*

Aiming to a better surface coverage, a different deposition method was employed. Electrostatic LbL deposition with polyelectrolytes such as PDDA and PAA was performed with 37 nm TA stabilized Ag NPs. The SEM image in Figure 3-9 shows the PDDA-Ag NPs network on a chemiresistive substrate after 3 consecutive LbL depositions. The inset clearly highlights the good surface coverage both on the IDE gold electrode and Si/SiO_2 channel, where a good degree of percolation is achieved. For this reason, the sensing substrates presented in the following Sections will be fabricated with electrostatic LbL deposition of PDDA and TA stabilized Ag NPs.

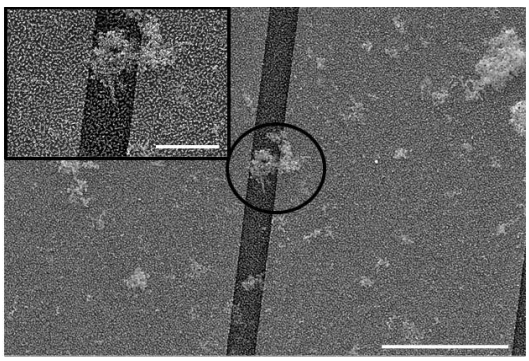

Figure 3-9 SEM images of the PDDA-TA stabilized Ag NPs network, obtained after 3 consecutive depositions on chemiresistive substrates exposing gold IDEs (L= 2.5 µm). Ag

NPs size is 37 nm. The inset image shows the highlighted region at a higher magnification. The scale bars represent 10 µm and 3 µm in the low and high magnification image, respectively.

3.2.3 SERS sensing platforms optimization

Optimization of the SERS sensing platforms was performed varying the size of TA stabilized Ag NPs and the number of LbL depositions on glass substrates, following the variation of the optical properties and the morphology by UV-Vis-NIR spectroscopy, SEM and AFM, as well as the SERS effect.

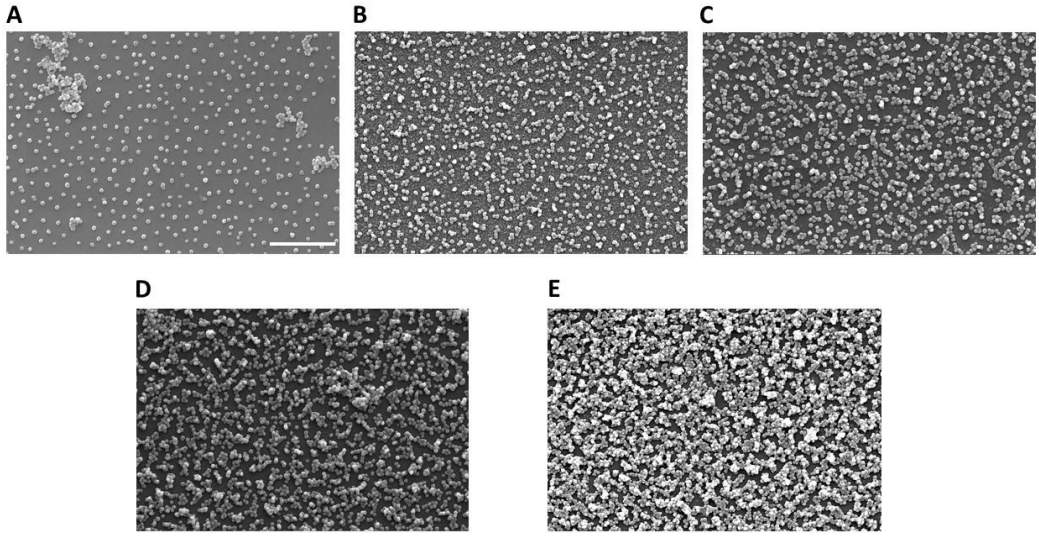

*Figure 3-10 SEM images of the plasmonic thin films obtained after **A)** one, **B)** two, **C)** three, **D)** four and **E)** five LbL depositions of PDDA and 37 nm Ag NP on glass substrates. The scale bar represents 1 µm.*

The SEM morphological characterization of the platforms shows that after one deposition of 37 nm Ag NPs the majority of the nanoparticles are isolated, while the formation of dimers and aggregates can be detected at higher NPs loadings (Figure 3-10A-E). In addition, it is possible to observe that five consecutive LbL depositions do not give rise to five layers of Ag NPs,

but instead more densely packed aggregates can be spotted on the substrate surface.

To confirm these observations, AFM characterization was performed on the SERS sensing platforms fabricated with one to four depositions of PDDA/Ag NPs on glass substrates. Figure 3-11A-D show isolated Ag NPs lying on the substrate surface when the first deposition is performed, while the degree of aggregation increases with the number of depositions, leading to a continuous interacting network of Ag NPs in Figure 3-11D. Moreover, analysing the line trace along the highlighted dashed lines for all the sensing platforms, it is clear that, increasing the number of depositions, the distance between adjacent Ag NPs on the substrate surface decreases, while after three depositions it is possible to observe height values of ~ 80 nm, ascribable to two NPs lying one on the other, as shown also in the insets. The surface roughness values of the plasmonic thin films are 12 ± 1 nm, 16 ± 1 nm, 18.5 ± 1.5 nm and 25.5 ± 1.5 nm when one to four depositions are performed.

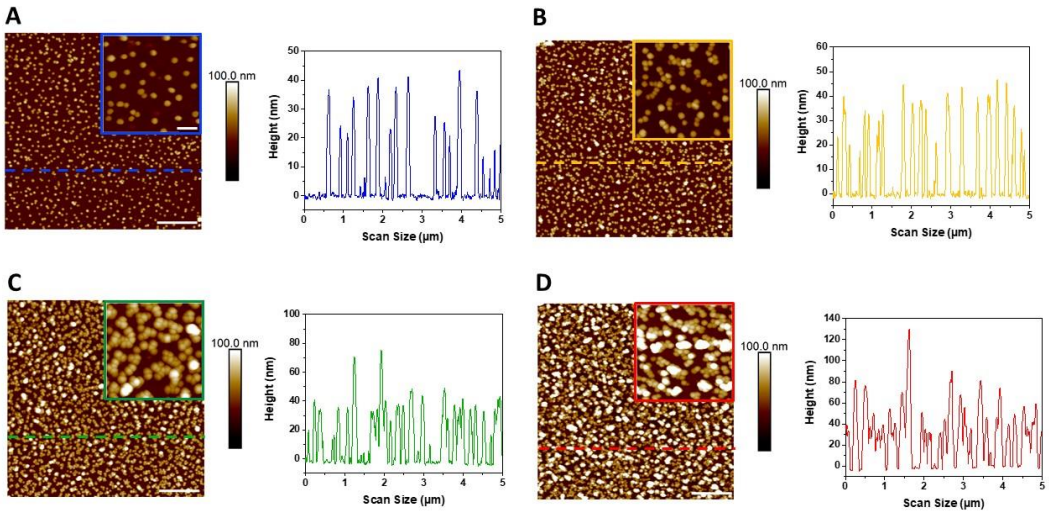

*Figure 3-11 AFM images (resolved by 512×512 pixels) and line trace along the dashed lines of the plasmonic thin films obtained after **A)** one, **B)** two, **C)** three and **D)** four LbL depositions of PDDA and 37 nm Ag NP on glass substrates. The insets are resolved by 1024x1024*

pixels. The scale bars represent 1 µm and 200 nm in the main images and the insets, respectively.

Moreover, when studying the optical properties on glass substrates, the plasmonic thin films exhibit the typical LSPR band for isolated Ag NPs at 382 nm, which is blue shifted compared to that for 37 nm TA stabilized Ag NPs dispersed in water (430 nm), as a consequence of the lower average refractive index of air compared to water, after their deposition on glass substrate.[147] In addition, increasing the loading of NPs on the substrate, a broad coupling band at lower energy (around 550 nm) appears (Figure 3-12A).

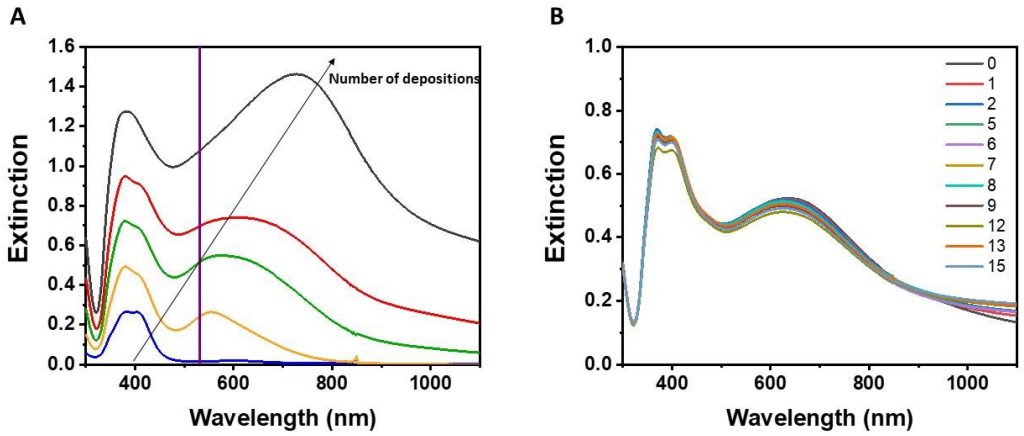

Figure 3-12 ***A)*** *UV-Vis-NIR extinction spectra of the plasmonic sensing platforms prepared by (blue) one, (yellow) two, (green) three, (red) four and (grey) five consecutive LbL depositions of PDDA and TA acid stabilized Ag NPs (37 nm diameter) on glass substrate. The position of the Raman laser line is highlighted in violet.* ***B)*** *Stability over 15 days of the UV-Vis-NIR extinction spectra of a plasmonic sensing platform prepared with three LbL depositions of PDDA and TA acid stabilized Ag NPs (37 nm diameter) on glass substrate, after $NaBH_4$ treatment.*

A similar behaviour was observed when the optical properties were studied as a function of the Ag NPs size (Appendix). Figure 3-12B shows the UV-Vis-NIR spectra of a plasmonic sensing platform prepared with 3 LbL depositions of PDDA and TA acid stabilized Ag NPs. The spectrum 0 was

recorded immediately after the treatment with $NaBH_4$ described in Section 3.1.7. Extinction spectra of the same sample were then acquired for 15 days and no evident variation of the optical properties was observed, thus suggesting a good stability of the plasmonic substrate in the considered period of time.

The SERS performance of the as-prepared plasmonic sensing platforms was studied as a function of Ag NPs loading and size, using 1-NAT. The latter is a small aromatic molecule containing a thiol group, which makes it suitable as a Raman reporter molecule with high affinity for noble metals, resulting in the formation of a monolayer on the substrate surface. The complete table of calculated vibrational bands maxima and their molecular vibration assignments are reported in the Appendix. The molecular structure of 1-NAT and its average SERS spectrum obtained on the surface of a plasmonic sensing platform prepared with three LbL depositions of PDDA and TA acid stabilized Ag NPs (37 nm diameter) on glass substrate is shown in Figure 3-13A. The SERS spectrum shows the characteristic SERS bands for 1-NAT: ring breathing at 821 cm^{-1}, C-H twisting at 964 cm^{-1}, C-H bending at 1024, 1064, 1133, 1198, 1252 and 1331 cm^{-1}, ring stretching at 1367, 1452, 1501, 1556, 1585 and 1618 cm^{-1}.[204] The highlighted ring stretching band at 1367 cm^{-1} was used to study the SERS intensity as a function of the size of TA stabilized Ag NPs. The histogram in Figure 3-13B clearly shows that, disregarding the NPs size, one deposition of Ag NPs does not give rise to a SERS effect, which instead becomes visible after two depositions. After three or four depositions of 15, 23 or 43 nm Ag NPs, the SERS intensity does not increase, while 37 nm Ag NPs give rise to the highest SERS intensity for the 1-NAT ring stretching band. The intensity of the latter was used to decode the SERS maps shown in Figure 3-13C-F, obtained after 3 LbL depositions of PDDA and TA stabilized Ag NPs with 15, 23, 37 and 43 nm diameters, respectively. The maps clearly show that the SERS intensity is highly uniform

and homogeneous in intensity over the whole area (40×40 μm^2) and that 37 nm Ag NPs give the highest SERS intensity (122.8 ± 35.7 kcts mW^{-1} s^{-1}). The SERS intensity decrease with the increasing Ag NPs size could be explained by the smaller surface area and huge radiation damping and dynamic depolarization, causing the adsorption of a smaller number of molecules on the particle's surface and a decrease in the field enhancement.[205, 206]

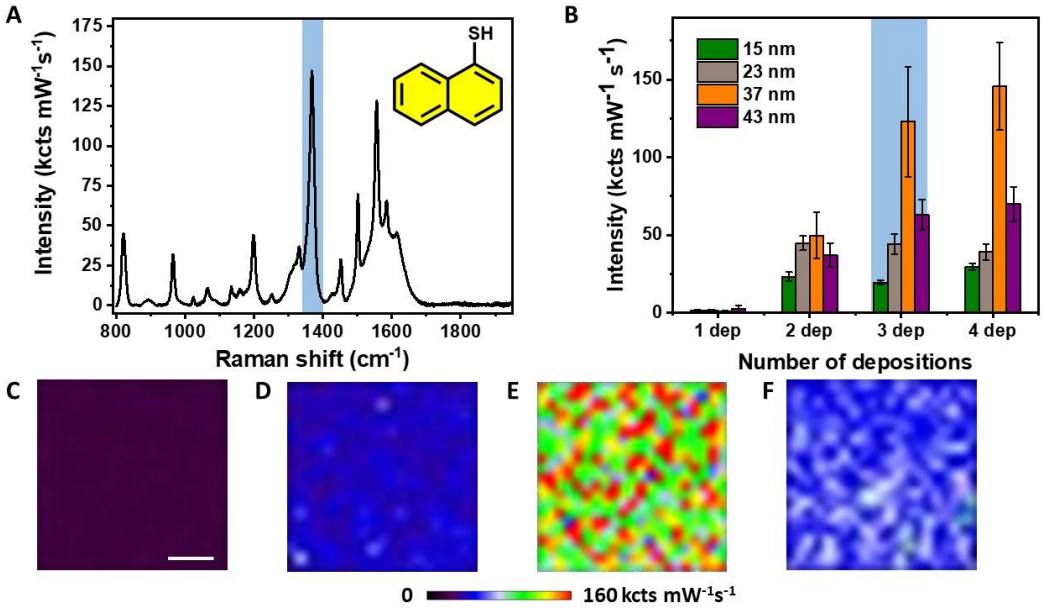

Figure 3-13 ***A)*** *Average SERS spectrum of 1-naphthalenthiol (1-NAT) adsorbed on a plasmonic sensing platform prepared by 3 LbL depositions of PDDA and 37 nm Ag NPs. The molecular structure of 1-NAT is shown in the inset.* ***B)*** *SERS intensity of the highlighted ring stretching band (1367 cm^{-1}) as a function of the Ag NPS size and number of depositions. SERS mappings of the SERS intensity of the 1367 cm^{-1} band on the plasmonic sensing platforms prepared by 3 LbL depositions of PDDA and Ag NPs with a diameter of* ***C)*** *15 nm,* ***D)*** *23 nm,* ***E)*** *37 nm and* ***F)*** *43 nm. The scale bar represents 10 μm, while the colour scale refers to the maximum SERS intensity obtained with 3 depositions of 37 nm Ag NPs.*

The SERS intensity variation as a function of the number of depositions was studied with 37 nm Ag NPs. Figure 3-14A shows that the SERS intensity increases with the number of depositions, but when the fourth bilayer is deposited, only a ~ 20% increase is obtained (122.8 ± 35.7 kcts mW^{-1} s^{-1} and

145.6 ± 28.2 kcts mW^{-1} s^{-1} for three and four depositions, respectively). Moreover, after five depositions, the SERS intensity decreases to 95.07 ±14.8 kcts mW^{-1} s^{-1}. Probably, the increased surface coverage shown in Figure 3-10E, induces a strong plasmon coupling between adjacent NPs with different orientations, leading to a hot-spot deactivation when a higher number of depositions is performed. In addition, the 532 nm laser line does not match the plasmon coupling band for the five depositions sample, which is characterized by a huge red shift, compared to the other samples (Figure 3-12A).

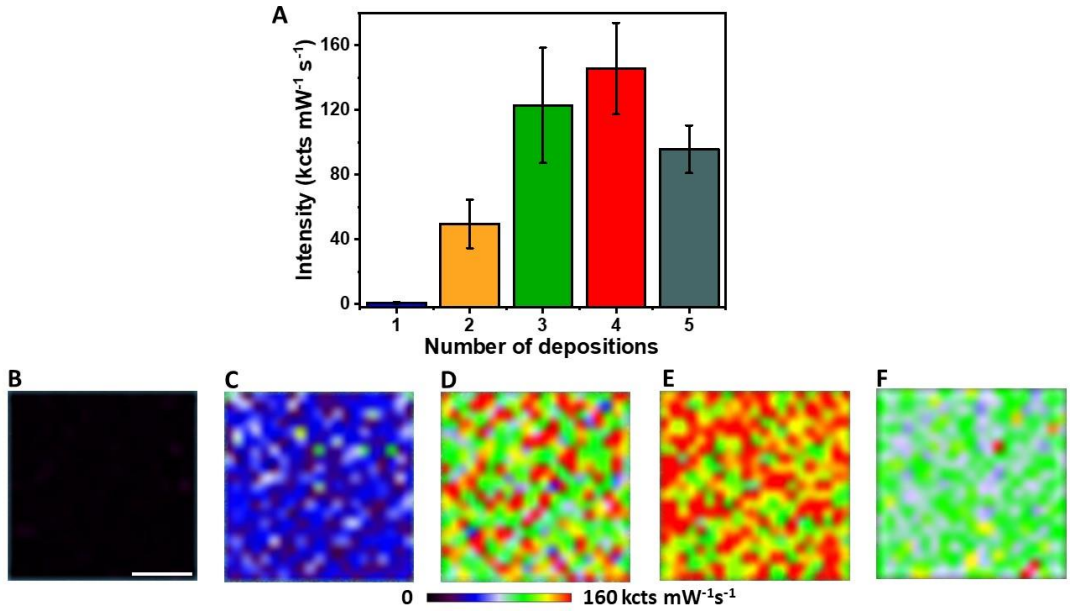

Figure 3-14 ***A)*** *SERS intensity of 1-NAT ring stretching band (1367 cm^{-1}) as a function of the number of depositions of 37 nm Ag NPs. SERS mappings obtained at 1367 cm^{-1} after* ***B)*** *one,* ***C)*** *two,* ***D)*** *three,* ***E)*** *four and* ***F)*** *five depositions of PDDA and 37 nm Ag NPs. The scale bar represents 10 µm, while the colour scale refers to the maximum SERS intensity obtained after 3 depositions.*

SERS sensing was then performed using sensing platforms prepared with three depositions of 37 nm Ag NPs.

3.2.4 Detection of Hg^{2+} ions in water

The sensing strategy relies on the redox reaction between Ag^0 and Hg^{2+}, with the standard reduction potentials of 0.851 V *vs* NHE for Hg^{2+}/Hg and 0.799 V *vs* NHE for bulk Ag^+/Ag.[207] A sufficient driving force for the reaction is probably resulting from the higher reactivity of silver at the nanoscale, since the reduction in size usually leads to a decrease in the reduction potential.[208] Ivanova *et al.* reported a redox potential of 0.627 V *vs* NHE for 42.9 ± 13.2 Ag NPs.[209] For this reason, the proposed fabrication method of plasmonic sensing platforms is extremely versatile, since, in the presence of the analyte, a SERS intensity turn-off and resistance increase can be both observed.

3.2.4.1 Hg^{2+} ions in water: chemiresistive detection and selectivity

The detection of Hg^{2+} ions was performed taking advantage of the resistance variation caused by the redox reaction between Ag^0 and Hg^{2+} taking place on the surface of the fabricated chemiresistive sensors. In Figure 3-15A, the red curve shows that the deposited Ag NPs based thin film is able to provide the electrical conductivity in the 2.5 µm electrodic channel, giving rise to a linear I-V correlation, in the investigated voltage range. Furthermore, the SEM image in Figure 3-15B clearly shows the film percolating in the channel. However, when the substrate is immersed for 30 min in 1 mM $Hg(NO_3)_2$ solution, a dramatic increase in resistance can be detected (black curve in Figure 3-15A): the huge decrease in size and number of Ag NPs in the electrodic channel (Figure 3-15C) makes the electron transfer along the device impossible. Interestingly, as far as the selectivity is concerned, the plasmonic thin film did not show any significant interaction with alkaline and alkaline earth metals, while a slight decrease in the resistance ratio (final resistance R_f / initial resistance R_i) is observed when the substrate is exposed

to transition and heavy metals (Figure 3-15D-E). Alkaline (Na, Li and K) and alkaline earth metals (Ca and Mg) are characterized by highly negative reduction potentials compared to the Ag^+/Ag redox couple, meaning that they are not prone to be reduced in the presence of Ag^0. On the contrary, exposing the chemiresistive platforms to Cd, Pb and Cu ions, the observed reduced resistance (Figure 3-15D inset) could be associated with the chemisorption of these metals on the NPs surface,[210] giving rise to a conductive shell. The process could be also driven by the ability of tannic acid to coordinate these metals, through its abundant hydroxyl functional groups.[211] The standard reduction potentials of the used cations are reported in the Appendix.

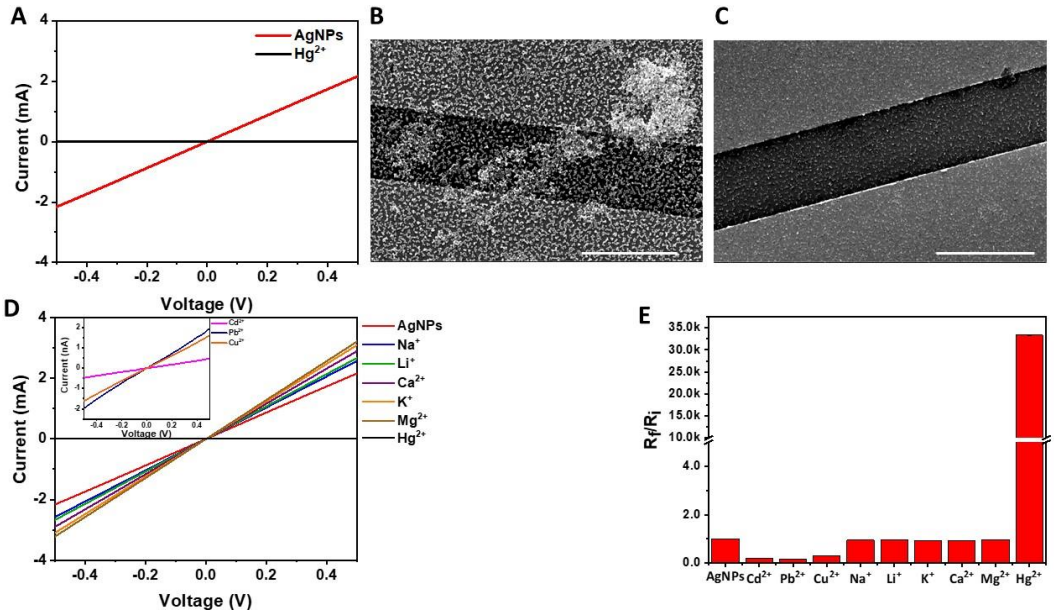

Figure 3-15 ***A)*** *Current-Voltage curves for the chemiresistive substrates functionalized with 3 LbL depositions of PDDA and 37 nm Ag NPs (red) before and (black) after the immersion in 1 mM $Hg(NO_3)_2$ solution for 30 min.* ***B-C)*** *SEM micrographs of the plasmonic thin films deposited on chemiresistive substrates* ***B)*** *before and* ***C)*** *after the immersion in 1 mM $Hg(NO_3)_2$ solution for 30 min. The electrodic channel length is 2.5 µm and the scale bars represent 3 µm.* ***D)*** *Current-Voltage curves for the chemiresistive substrates functionalized with 3 LbL depositions of PDDA and 37 nm Ag NPs before and after the immersion in 1 mM salt solutions for 30 min. The reported I-V curves are the average of four different acquisitions.* ***E)*** *Resistance ratio (final resistance Rf / initial resistance Ri) for the plasmon modified chemiresistive substrates extrapolated from the I-V curves as a function of the metal ions.*

3.2.4.2 Hg^{2+} ions in water: SERS detection

The SERS intensity turn-off method relies on the disruption of the interaction between the Ag NPs and the Raman reporter molecules, causing a decrease in SERS intensity, in the presence of the analyte.[212] The detection of Hg^{2+} ions was then performed following the lowering of the SERS signals of the Raman reporter molecule (TA stabilizing agent or 1-NAT) on the Ag NPs surface. The observed phenomenon is probably related to the displacement of the capping agent from the Ag NPs surface.

First of all, the actual interaction between Ag^0 and Hg^{2+} was proved studying the SERS intensity decrease of the C-O stretching band of TA phenols after the immersion of the plasmonic substrate in 1 mM $Hg(NO_3)_2$ solution for 30 min. In Figure 3-16A, it is possible to observe the characteristic Raman spectrum (in black) for TA, whose most defined band peaked at 1300 cm^{-1} is highlighted in blue. When the plasmonic substrate is immersed in 1 mM $Hg(NO_3)_2$ for 30 min, the SERS intensity of the entire spectrum dramatically decreases (green spectrum). The area of the C-O stretching band of TA (1250-1370 cm^{-1}) decreases from 762.425 ± 169.167 k to 0.4798 ± 0.1 k. This huge variation is even more clear when the SERS mappings for this Raman peak area are analysed (Figure 3-16B-C). Furthermore, the SERS maps demonstrate that the area of the Raman band is homogeneous over all the substrate surface, before and after the immersion in $Hg(NO_3)_2$ solution. When the Hg^{2+} concentration is lower (1 µM), the predominant effect is probably the amalgam formation subsequent to the chemisorption of reduced mercury on the NPs surface.[207] In the Appendix, the variation of the averaged SERS spectra for 1-NAT before and after the immersion of the plasmonic sensing platform in 1 µM Hg^{2+} solution for 1, 5 and 30 min is shown. The plot in Figure 3-16D highlights that the rate of Ag NPs oxidation

is extremely high: the SERS peak area ratio (final peak area/initial peak area, A_f/A_i) for 1-NAT ring stretching band (1367 cm^{-1}) undergoes a ~ 40% reduction after just 1 min from the immersion in $Hg(NO_3)_2$ 1 µM. SERS mappings demonstrate that the reduction of the peak area is significant over all the substrate surface after its immersion in $Hg(NO_3)_2$ 1 µM for 1 min Figure 3-16 E-F). Furthermore, when the immersion is prolonged for 5 and 30 min, A_f/A_i does not undergo any significant change, probably due to the chemisorption of reduced mercury on the Ag NPs surface.

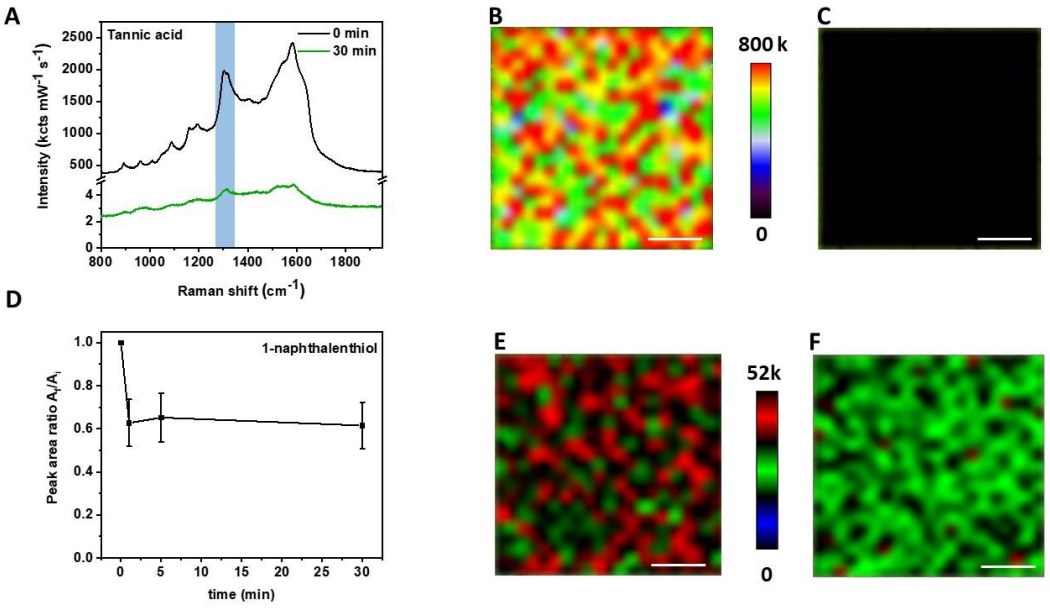

Figure 3-16 ***A)*** *Average SERS spectra of TA capping agent on 37 nm Ag NPs (black) before and (green) after the immersion in $Hg(NO_3)_2$ 1 mM for 30 min. The sensing platform was prepared by 3 LbL depositions of PDDA and 37 nm Ag NPs.* ***B-C)*** *SERS mappings obtained at 1300 cm^{-1}* ***B)*** *before and* ***C)*** *after the immersion of the sensing platform in $Hg(NO_3)_2$ 1 mM for 30 min.* ***D)*** *Variation of the 1-NAT 1367 cm^{-1} peak area ratio (Af/Ai) with the immersion in $Hg(NO_3)_2$ 1 µM for 1, 5 and 30 min.* ***E-F)*** *SERS mappings obtained at 1367 cm^{-1}* ***E)*** *before and* ***F)*** *after the immersion of the sensing platform in $Hg(NO_3)_2$ 1 µM for 1 min. The scale bars represent 10 µm.*

3.3 Conclusions

In summary, Ag NPs stabilized by tannic acid or citrate, Au NPs and Au@Ag core@shell NPs were successfully synthesized and characterized. Their deposition on glass and Si/SiO_2 exposing gold IDEs was performed and studied: it was demonstrated that the electrostatic LbL deposition with polyelectrolytes is more suitable than the cross-linking with dithiols for the deposition of tannic acid stabilized Ag NPs. For this reason, the plasmonic sensing platforms prepared with this method were fully characterized by UV-Vis-NIR spectroscopy, SEM and AFM microscopies and SERS spectroscopy. Besides, in spite of the well-known reactivity of Ag NPs arising from oxidation, the optical properties of the substrates revealed to be stable over 15 days. Using 1-NAT as a Raman reporter molecule, the analysis of the SERS performance of the plasmonic thin films as a function of Ag NPs size and loading shows that the highest SERS effect is obtained after three depositions of 37 nm Ag NPs. The same deposition procedure was used for the fabrication of chemiresistor devices and the prepared plasmonic thin film revealed to be able to provide the electrical conductivity in the electrodic channel. The as-fabricated plasmonic sensing substrates were used for the detection of mercury ions in water both by indirect SERS and chemiresistivity. The sensing strategy relies on the redox reaction occurring between Ag^0 and Hg^{2+}. Furthermore, the prepared sensing platforms revealed to be extremely selective for mercury ions over other alkaline, earth alkaline, transition and heavy metal ions. The preliminary study presented in this thesis shows that the prepared multiresponsive plasmonic substrates are promising candidates for the ultrasensitive detection of Hg^{2+} and there is still space for the investigation of the limit of detection even in real water samples, as well as the application for the detection of other analytes.

4 Appendix

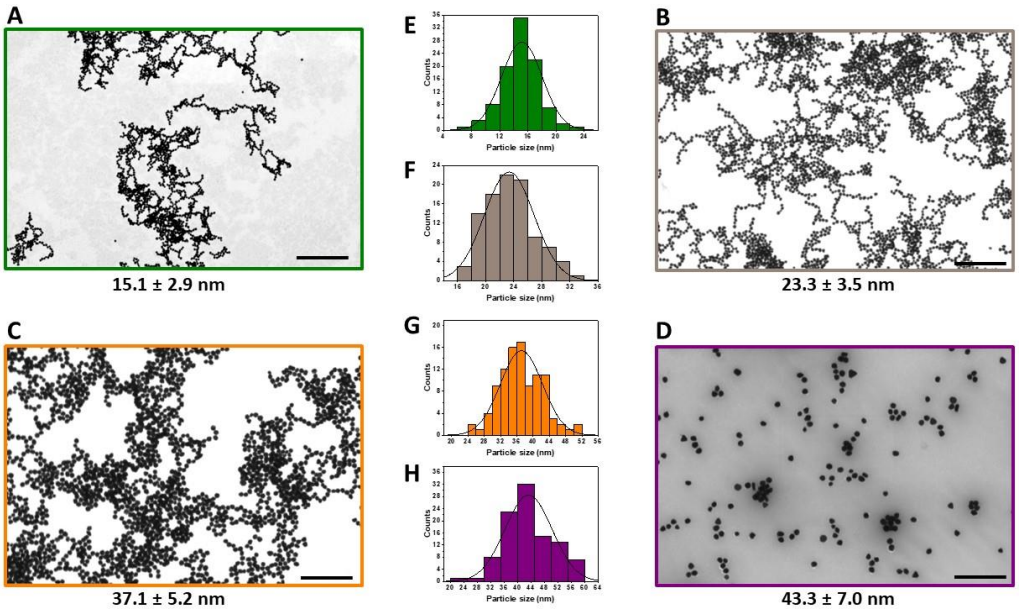

Figure 4-1 ***A-D)*** *STEM images of the synthesized tannic acid stabilized Ag NPs. The reported sizes were determined as an average of the diameter of 100 particles for each Ag NPs generation.* ***E-H)*** *Particle size distribution for every Ag NPs generation.*

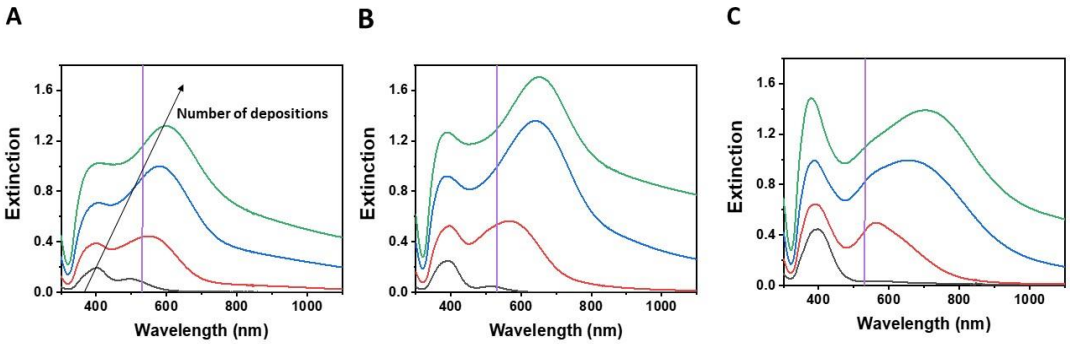

Figure 4-2 UV-Vis-NIR extinction spectra of the plasmonic sensing platforms prepared by (blue) one, (yellow) two, (green) three and (red) four LbL depositions of PDDA and TA acid stabilized Ag NPs with the following diameter: ***A)*** *15 nm,* ***B)*** *23 nm and* ***C)*** *43 nm on glass substrate. The position of the Raman laser line is highlighted in violet*

Table 4-1. Calculated vibrational bands maxima in cm^{-1} and their molecular vibration assignments for 1-naphthalenthiol, after minimization of the geometry using Gaussian '03 suite of programs with the 6–311G(p,d) basis set Adapted from Reference [204].

Calculated vibrational bands maxima (cm^{-1})	**Molecular vibration assignment**
75, 126	Ring torsion and S-H wagging
171	Ring butterfly
211	Ring twisting
231	Ring wagging
389	Ring deformation and C-S stretching
415	Ring wagging
424	Ring deformation
474	Ring twisting
518, 543	Ring deformation
546	Ring wagging
630	Ring twisting
675	Ring deformation
739, 781	C-H wagging
798	Ring deformation
799	C-H wagging
828	Ring breathing
863	C-H wagging
896	C-H twisting
942	S-H bending
961, 976	C-H twisting
990	Ring breathing

997	C-H twisting
1048, 1091, 1165, 1171, 1190, 1231, 1239, 1287	C-H bending
1367, 1388	Ring stretching
1415	C-H bending
1469, 1490, 1543, 1604, 1633, 1662	Ring stretching
2680	S-H stretching
3160, 3163, 3170, 3172, 3181, 3187, 3192	C-H stretching

Table 4-2. Standard reduction potentials for the analysed metal redox couple at 25°C.

Redox couple	**E^0 (V)**
Hg^{2+}/Hg	0.851
Hg_2^{2+}/Hg	0.80
Ag^{+}/Ag	0.799
Cd^{2+}/Cd	-0.400
Pb^{2+}/Pb	-0.126
Cu^{2+}/Cu	0.337
Na^{+}/Na	-2.71
Li^{+}/Li	-3.04
K^{+}/K	-2.92
Ca^{2+}/Ca	-2.76
Mg^{2+}/Mg	-2.38
Au^{3+}/Au	1.50

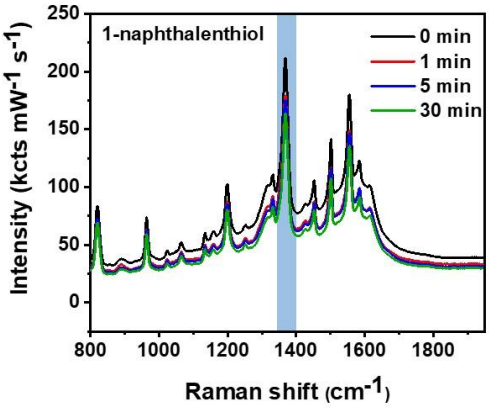

Figure 4-3 Average SERS spectra of 1-NAT adsorbed on a sensing platform was prepared by 3 LbL depositions of PDDA and 37 nm Ag NPs (black) before and after the immersion in in $Hg(NO_3)_2$ 1 µM for (red) 1 min, (blue) 5 min and (green) 30 min. The ring stretching band (1367 cm^{-1}) is highlighted in blue.

5 References

1. Liz-Marzán, L.M. Nanometals. *Materials Today*. (February), 26–31, doi: 10.1016/S1369-7021(04)00080-X (**2004**).

2. Homer Glaucus and Diomedes. *Iliad*. 120–130.

3. Nonnus of Panopolis No Title. *Dyonisiaca*. XX–XXI.

4. BARBER, D.J., FREESTONE, I.C. an Investigation of the Origin of the Colour of the Lycurgus Cup By Analytical Transmission Electron Microscopy. *Archaeometry*. 32 (1), 33–45, doi: 10.1111/j.1475-4754.1990.tb01079.x (**1990**).

5. Freestone, I., Meeks, N., Sax, M., Higgitt, C. The Lycurgus Cup - A Roman nanotechnology. *Gold Bulletin*. 40 (4), 270–277, doi: 10.1007/BF03215599 (**2007**).

6. Sciau, P., Mirguet, C., Roucau, C., Chabanne, D., Schvoerer, M. Double Nanoparticle Layer in a 12th Century Lustreware Decoration: Accident or Technological Mastery? *Journal of Nano Research*. 8, 133–139, doi: 10.4028/www.scientific.net/JNanoR.8.133 (**2009**).

7. Heiligtag, F.J., Niederberger, M. The fascinating world of nanoparticle research. *Materials Today*. 16 (7–8), 262–271, doi: 10.1016/j.mattod.2013.07.004 (**2013**).

8. Garcia, M.A. Surface plasmons in metallic nanoparticles: fundamentals and applications. *Journal of Physics D: Applied Physics*. 44 (28), 283001, doi: 10.1088/0022-3727/44/28/283001 (**2011**).

9. Amendola, V., Pilot, R., Frasconi, M., Maragò, O.M., Iatì, M.A. Surface plasmon resonance in gold nanoparticles: a review. *Journal of Physics: Condensed Matter*. 29 (20), 203002, doi: 10.1088/1361-648X/aa60f3 (**2017**).

10. Hutter, E., Fendler, J.H. Exploitation of Localized Surface Plasmon Resonance. *Advanced Materials*. 16 (19), 1685–1706, doi: 10.1002/adma.200400271 (**2004**).

11. Le Ru, E.C., Etchegoin, P.G. Introduction to plasmons and plasmonics.

Principles of Surface-Enhanced Raman Spectroscopy. 121–183, doi: 10.1016/b978-0-444-52779-0.00009-x (**2009**).

12. Valenti, M. *et al.* Hot Carrier Generation and Extraction of Plasmonic Alloy Nanoparticles. *ACS Photonics*. 4 (5), 1146–1152, doi: 10.1021/acsphotonics.6b01048 (**2017**).

13. Kumar, R. *et al.* Determination of the Aspect-ratio Distribution of Gold Nanorods in a Colloidal Solution using UV-visible absorption spectroscopy. *Scientific Reports*. 9 (1), 1–10, doi: 10.1038/s41598-019-53621-4 (**2019**).

14. Hornyak, G.L., Tibbals, H.F., Dutta, J., Moore, J.J. *Introduction to Nanoscience and Nanotechnology.* CRC Press. (2008).

15. Turkevich, J., Stevenson, P.C., Hillier, J. A study of the nucleation and growth processes in the synthesis of colloidal gold. *Discussions of the Faraday Society*. 11 (0), 55–75, doi: 10.1039/DF9511100055 (**1951**).

16. FRENS, G. Controlled Nucleation for the Regulation of the Particle Size in Monodisperse Gold Suspensions. *Nature Physical Science*. 241 (105), 20–22, doi: 10.1038/physci241020a0 (**1973**).

17. Ji, X., Song, X., Li, J., Bai, Y., Yang, W., Peng, X. Size control of gold nanocrystals in citrate reduction: The third role of citrate. *Journal of the American Chemical Society*. 129 (45), 13939–13948, doi: 10.1021/ja074447k (**2007**).

18. Zhao, P., Li, N., Astruc, D. State of the art in gold nanoparticle synthesis. *Coordination Chemistry Reviews*. 257 (3–4), 638–665, doi: 10.1016/j.ccr.2012.09.002 (**2013**).

19. Lee, P.C., Meisel, D. Adsorption and surface-enhanced Raman of dyes on silver and gold sols. *Journal of Physical Chemistry*. 86 (17), 3391–3395, doi: 10.1021/j100214a025 (**1982**).

20. Pillai, Z.S., Kamat, P. V. What factors control the size and shape of silver nanoparticles in the citrate ion reduction method? *Journal of Physical Chemistry B*. 108 (3), 945–951, doi: 10.1021/jp037018r

(**2004**).

21. Bastús, N.G., Comenge, J., Puntes, V. Kinetically controlled seeded growth synthesis of citrate-stabilized gold nanoparticles of up to 200 nm: Size focusing versus ostwald ripening. *Langmuir*. 27 (17), 11098–11105, doi: 10.1021/la201938u (**2011**).

22. Nakano, M., Fujiwara, T., Koga, N. Thermal Decomposition of Silver Acetate: Physico-Geometrical Kinetic Features and Formation of Silver Nanoparticles. *Journal of Physical Chemistry C*. 120 (16), 8841–8854, doi: 10.1021/acs.jpcc.6b02377 (**2016**).

23. Wang, R.-C., Gao, Y.-S., Chen, S.-J. Simple synthesis and size-dependent surface-enhanced Raman scattering of Ag nanostructures on TiO_2 by thermal decomposition of silver nitrate at low temperature. *Nanotechnology*. 20 (37), 375605, doi: 10.1088/0957-4484/20/37/375605 (**2009**).

24. Lan, Z., Wu, J., Lin, J., Huang, M. Morphology controllable fabrication of Pt counter electrodes for highly efficient dye-sensitized solar cells. *Journal of Materials Chemistry*. 22 (9), 3948–3954, doi: 10.1039/c2jm15019k (**2012**).

25. Amendola, V., Meneghetti, M. Laser ablation synthesis in solution and size manipulation of noble metal nanoparticles. *Physical Chemistry Chemical Physics*. 11 (20), 3805–3821, doi: 10.1039/b900654k (**2009**).

26. Zeng, H. *et al.* Nanomaterials via laser ablation/irradiation in liquid: A review. *Advanced Functional Materials*. 22 (7), 1333–1353, doi: 10.1002/adfm.201102295 (**2012**).

27. Tilaki, R.M., Zad, A.I., Mahdavi, S.M. Size, composition and optical properties of copper nanoparticles prepared by laser ablation in liquids. *Applied Physics A: Materials Science and Processing*. 88 (2), 415–419, doi: 10.1007/s00339-007-4000-2 (**2007**).

28. Mafuné, F., Kohno, J.Y., Takeda, Y., Kondow, T., Sawabe, H. Formation and size control of silver nanoparticles by laser ablation in aqueous solution. *Journal of Physical Chemistry B*. 104 (39), 9111–9117, doi: 10.1021/jp001336y (**2000**).

29. Intartaglia, R. *et al.* Laser synthesis of ligand-free bimetallic nanoparticles for plasmonic applications. *Physical Chemistry Chemical Physics*. 15 (9), 3075–3082, doi: 10.1039/c2cp42656k (**2013**).

30. Loza, K., Heggen, M., Epple, M. Synthesis, Structure, Properties, and Applications of Bimetallic Nanoparticles of Noble Metals. *Advanced Functional Materials*. 30 (21), 1909260, doi: 10.1002/adfm.201909260 (**2020**).

31. Li, G.R., Gao, X.P. Low-Cost Counter-Electrode Materials for Dye-Sensitized and Perovskite Solar Cells. *Advanced Materials*. 32 (3), 1–20, doi: 10.1002/adma.201806478 (**2020**).

32. Calogero, G., Bartolotta, A., Di Marco, G., Di Carlo, A., Bonaccorso, F. Vegetable-based dye-sensitized solar cells. *Chem. Soc. Rev.* 44 (10), 3244–3294, doi: 10.1039/C4CS00309H (**2015**).

33. O'Regan, B., Grätzel, M. A low-cost, high-efficiency solar cell based on dye-sensitized colloidal TiO2 films. *Nature*. 353 (6346), 737–740, doi: 10.1038/353737a0 (**1991**).

34. Snaith, H.J., Schmidt-Mende, L. Advances in liquid-electrolyte and solid-state dye-sensitized solar cells. *Advanced Materials*. 19 (20), 3187–3200, doi: 10.1002/adma.200602903 (**2007**).

35. Peter, L.M. Dye-sensitized nanocrystalline solar cells. *Physical Chemistry Chemical Physics*. 9 (21), 2630–2642, doi: 10.1039/b617073k (**2007**).

36. Gra, M. Hagfeldt, Grätzel - 2000 - Molecular Photovoltaics - Accounts of Chemical Research.pdf - Unknown.pdf - Unknown.pdf. 33 (5), 269–277 (**2000**).

37. Bisquert, J., Cahen, D., Hodes, G., Rühle, S., Zaban, A. Physical chemical principles of photovoltaic conversion with nanoparticulate, mesoporous dye-sensitized solar cells. *Journal of Physical Chemistry B*. 108 (24), 8106–8118, doi: 10.1021/jp0359283 (**2004**).

38. Kakiage, K., Aoyama, Y., Yano, T., Oya, K., Fujisawa, J.I., Hanaya, M.

Highly-efficient dye-sensitized solar cells with collaborative sensitization by silyl-anchor and carboxy-anchor dyes. *Chemical Communications*. 51 (88), 15894–15897, doi: 10.1039/c5cc06759f (**2015**).

39. Chang, J.A. *et al.* High-performance nanostructured inorganicâ-organic heterojunction solar cells. *Nano Letters*. 10 (7), 2609–2612, doi: 10.1021/nl101322h (**2010**).

40. Calogero, G., Bartolotta, A., Di Marco, G., Di Carlo, A., Bonaccorso, F. Vegetable-based dye-sensitized solar cells. *Chemical Society Reviews*. 44 (10), 3244–3294, doi: 10.1039/c4cs00309h (**2015**).

41. Kalyanasundaram, K. *Dye-sensitized Solar Cells*. doi: 10.1201/b16409. EPFL Press. (2010).

42. Hagfeldt, A., Boschloo, G., Sun, L., Kloo, L., Pettersson, H. Dye-sensitized solar cells. *Chemical Reviews*. 110 (11), 6595–6663, doi: 10.1021/cr900356p (**2010**).

43. Ji, J.M., Zhou, H., Kim, H.K. Rational design criteria for D-π-A structured organic and porphyrin sensitizers for highly efficient dye-sensitized solar cells. *Journal of Materials Chemistry A*. 6 (30), 14518–14545, doi: 10.1039/c8ta02281j (**2018**).

44. Zhang, J. *et al.* A promising anchor group for efficient organic dye sensitized solar cells with iodine-free redox shuttles: A theoretical evaluation. *Journal of Materials Chemistry A*. 1 (44), 14000–14007, doi: 10.1039/c3ta12311a (**2013**).

45. Hara, K., Arakawa, H. Dye-Sensitized Solar Cells. *Handbook of Photovoltaic Science and Engineering*. 663–700, doi: 10.1002/0470014008.ch15 (**2005**).

46. Halme, J., Vahermaa, P., Miettunen, K., Lund, P. Device Physics of Dye Solar Cells. *Advanced Materials*. 22 (35), E210–E234, doi: 10.1002/adma.201000726 (**2010**).

47. Kutlu, N. Investigation of electrical values of low-efficiency dye-sensitized solar cells (DSSCs). *Energy*. 199, 117222, doi: 10.1016/j.energy.2020.117222 (**2020**).

48. Qi, B., Wang, J. Fill factor in organic solar cells. *Physical Chemistry Chemical Physics*. 15 (23), 8972–8982, doi: 10.1039/c3cp51383a (**2013**).

49. Katoh, R., Furube, A. Electron injection efficiency in dye-sensitized solar cells. *Journal of Photochemistry and Photobiology C: Photochemistry Reviews*. 20 (1), 1–16, doi: 10.1016/j.jphotochemrev.2014.02.001 (**2014**).

50. Grätzel, M. Photoelectrochemical cells. *Nature*. 414 (6861), 338–344, doi: 10.1038/35104607 (**2001**).

51. Elumalai, N.K., Vijila, C., Jose, R., Uddin, A., Ramakrishna, S. Metal oxide semiconducting interfacial layers for photovoltaic and photocatalytic applications. *Materials for Renewable and Sustainable Energy*. 4 (3), 1–25, doi: 10.1007/s40243-015-0054-9 (**2015**).

52. Vittal, R., Ho, K.C. Zinc oxide based dye-sensitized solar cells: A review. *Renewable and Sustainable Energy Reviews*. 70, 920–935, doi: 10.1016/j.rser.2016.11.273 (**2017**).

53. Memarian, N., Concina, I., Braga, A., Rozati, S.M., Vomiero, A., Sberveglieri, G. Hierarchically Assembled ZnO Nanocrystallites for High-Efficiency Dye-Sensitized Solar Cells. *Angewandte Chemie International Edition*. 50 (51), 12321–12325, doi: 10.1002/anie.201104605 (**2011**).

54. Keis, K., Lindgren, J., Lindquist, S.E., Hagfeldt, A. Studies of the adsorption process of Ru complexes in nanoporous ZnO electrodes. *Langmuir*. 16 (10), 4688–4694, doi: 10.1021/la9912702 (**2000**).

55. Gubbala, S., Chakrapani, V., Kumar, V., Sunkara, M.K. Band-Edge Engineered Hybrid Structures for Dye-Sensitized Solar Cells Based on SnO $_2$ Nanowires. *Advanced Functional Materials*. 18 (16), 2411–2418, doi: 10.1002/adfm.200800099 (**2008**).

56. Wijeratne, K., Akilavasan, J., Thelakkat, M., Bandara, J. Enhancing the solar cell efficiency through pristine 1-dimentional SnO 2 nanostructures: Comparison of charge transport and carrier lifetime of SnO 2 particles vs. nanorods. *Electrochimica Acta*. 72, 192–198, doi:

10.1016/j.electacta.2012.04.016 (**2012**).

57. Gu, F., Huang, W., Wang, S., Cheng, X., Hu, Y., Li, C. Improved photoelectric conversion efficiency from titanium oxide-coupled tin oxide nanoparticles formed in flame. *Journal of Power Sources*. 268, 922–927, doi: 10.1016/j.jpowsour.2014.06.012 (**2014**).

58. Shakeel Ahmad, M., Pandey, A.K., Abd Rahim, N. Advancements in the development of TiO2 photoanodes and its fabrication methods for dye sensitized solar cell (DSSC) applications. A review. *Renewable and Sustainable Energy Reviews*. 77, 89–108, doi: 10.1016/j.rser.2017.03.129 (**2017**).

59. Qian, D., Li, Y., Zhang, Q., Shi, G., Wang, H. Anatase TiO2 sols derived from peroxotitanium acid and to form transparent TiO2 compact film for dye-sensitized solar cells. *Journal of Alloys and Compounds*. 509 (41), 10121–10126, doi: 10.1016/j.jallcom.2011.08.055 (**2011**).

60. Ito, S. *et al.* Control of dark current in photoelectrochemical (TiO2/I -- I3-) and dye-sensitized solar cells. *Chemical Communications*. (34), 4351–4353, doi: 10.1039/b505718c (**2005**).

61. Ito, S. *et al.* Fabrication of thin film dye sensitized solar cells with solar to electric power conversion efficiency over 10%. *Thin Solid Films*. 516 (14), 4613–4619, doi: 10.1016/j.tsf.2007.05.090 (**2008**).

62. Sommeling, P.M. *et al.* Influence of a TiCl4 post-treatment on nanocrystalline TiO 2 films in dye-sensitized solar cells. *Journal of Physical Chemistry B*. 110 (39), 19191–19197, doi: 10.1021/jp061346k (**2006**).

63. Hagfeldt, A., Grätzel, M. Molecular photovoltaics. *Accounts of Chemical Research*. 33 (5), 269–277, doi: 10.1021/ar980112j (**2000**).

64. Thavasi, V., Renugopalakrishnan, V., Jose, R., Ramakrishna, S. Controlled electron injection and transport at materials interfaces in dye sensitized solar cells. *Materials Science and Engineering R: Reports*. 63 (3), 81–99, doi: 10.1016/j.mser.2008.09.001 (**2009**).

65. Nazeeruddin, M.K., Humphry-Baker, R., Liska, P., Grätzel, M.

Investigation of sensitizer adsorption and the influence of protons on current and voltage of a dye-sensitized nanocrystalline TiO2 solar cell. *Journal of Physical Chemistry B*. 107 (34), 8981–8987, doi: 10.1021/jp022656f (**2003**).

66. Ning, Z., Tian, H. Improvement of dye-sensitized solar cells : what we know and what we need to know. 1170–1181, doi: 10.1039/c003841e (**2010**).

67. Grätzel, M. Conversion of sunlight to electric power by nanocrystalline dye-sensitized solar cells. *Journal of Photochemistry and Photobiology A: Chemistry*. 164 (1–3), 3–14, doi: 10.1016/j.jphotochem.2004.02.023 (**2004**).

68. Nath, N.C.D., Kim, J.C., Kim, K.P., Yim, S., Lee, J.J. Deprotonation of N3 adsorbed on TiO2 for high-performance dye-sensitized solar cells (DSSCs). *Journal of Materials Chemistry A*. 1 (43), 13439–13442, doi: 10.1039/c3ta12298k (**2013**).

69. Ning, Z., Fu, Y., Tian, H. Improvement of dye-sensitized solar cells: What we know and what we need to know. *Energy and Environmental Science*. 3 (9), 1170–1181, doi: 10.1039/c003841e (**2010**).

70. Nazeeruddin, M.K. *et al.* Conversion of Light to Electricity by cis-X2Bis (2,2′-bipyridyl-4,4′-dicarboxylate) ruthenium (II) Charge-Transfer Sensitizers (X = Cl−, Br−, I−, CN−, and SCN−) on Nanocrystalline TiO2 Electrodes. *Journal of the American Chemical Society*. 115 (14), 6382–6390, doi: 10.1021/ja00067a063 (**1993**).

71. Nazeeruddin, M.K. *et al.* Engineering of efficient panchromatic sensitizers for nanocrystalline TiO2-based solar cells. *Journal of the American Chemical Society*. 123 (8), 1613–1624, doi: 10.1021/ja003299u (**2001**).

72. Wang, P., Zakeeruddin, S.M., Moser, J.E., Nazeeruddin, M.K., Sekiguchi, T., Grätzel, M. A stable quasi-solid-state dye-sensitized solar cell with an amphiphilic ruthenium sensitizer and polymer gel electrolyte. *Nature Materials*. 2 (6), 402–407, doi: 10.1038/nmat904 (**2003**).

73. Gao, F. *et al.* Enhance the optical absorptivity of nanocrystalline TiO2 film with high molar extinction coefficient ruthenium sensitizers for high performance dye-sensitized solar cells. *Journal of the American Chemical Society*. 130 (32), 10720–10728, doi: 10.1021/ja801942j (**2008**).

74. Cao, Y. *et al.* Dye-sensitized solar cells with a high absorptivity ruthenium sensitizer featuring a 2-(hexylthio)thiophene conjugated bipyridine. *Journal of Physical Chemistry C*. 113 (15), 6290–6297, doi: 10.1021/jp9006872 (**2009**).

75. Zarate, X., Schott-Verdugo, S., Rodriguez-Serrano, A., Schott, E. The Nature of the Donor Motif in Acceptor-Bridge-Donor Dyes as an Influence in the Electron Photo-Injection Mechanism in DSSCs. *Journal of Physical Chemistry A*. 120 (9), 1613–1624, doi: 10.1021/acs.jpca.5b12215 (**2016**).

76. Feldt, S.M., Gibson, E.A., Gabrielsson, E., Sun, L., Boschloo, G., Hagfeldt, A. Design of organic dyes and cobalt polypyridine redox mediators for high-efficiency dye-sensitized solar cells. *Journal of the American Chemical Society*. 132 (46), 16714–16724, doi: 10.1021/ja1088869 (**2010**).

77. Hagberg, D.P. *et al.* Symmetric and unsymmetric donor functionalization. comparing structural and spectral benefits of chromophores for dye-sensitized solar cells. *Journal of Materials Chemistry*. 19 (39), 7232–7238, doi: 10.1039/b911397p (**2009**).

78. Gabrielsson, E. *et al.* Convergent/Divergent Synthesis of a Linker-Varied Series of Dyes for Dye-Sensitized Solar Cells Based on the D35 Donor. *Advanced Energy Materials*. 3 (12), 1647–1656, doi: 10.1002/aenm.201300367 (**2013**).

79. Yella, A. *et al.* Molecular engineering of a fluorene donor for dye-sensitized solar cells. *Chemistry of Materials*. 25 (13), 2733–2739, doi: 10.1021/cm401593b (**2013**).

80. Kakiage, K. *et al.* An achievement of over 12 percent efficiency in an organic dye-sensitized solar cell. *Chemical Communications*. 50 (48), 6379–6381, doi: 10.1039/c4cc02192d (**2014**).

81. Lu, J., Liu, S., Wang, M. Push-pull zinc porphyrins as light-harvesters for efficient dye-sensitized solar cells. *Frontiers in Chemistry*. 6 (NOV), 541, doi: 10.3389/fchem.2018.00541 (**2018**).

82. Urbani, M., Ragoussi, M.E., Nazeeruddin, M.K., Torres, T. Phthalocyanines for dye-sensitized solar cells. *Coordination Chemistry Reviews*. 381, 1–64, doi: 10.1016/j.ccr.2018.10.007 (**2019**).

83. Clifford, J.N., Martínez-Ferrero, E., Viterisi, A., Palomares, E. Sensitizer molecular structure-device efficiency relationship in dye sensitized solar cells. *Chemical Society Reviews*. 40 (3), 1635–1646, doi: 10.1039/b920664g (**2011**).

84. Shalini, S., Balasundara Prabhu, R., Prasanna, S., Mallick, T.K., Senthilarasu, S. Review on natural dye sensitized solar cells: Operation, materials and methods. *Renewable and Sustainable Energy Reviews*. 51, 1306–1325, doi: 10.1016/j.rser.2015.07.052 (**2015**).

85. Kumara, N.T.R.N., Lim, A., Lim, C.M., Petra, M.I., Ekanayake, P. Recent progress and utilization of natural pigments in dye sensitized solar cells: A review. *Renewable and Sustainable Energy Reviews*. 78, 301–317, doi: 10.1016/j.rser.2017.04.075 (**2017**).

86. Wu, J. *et al.* Electrolytes in dye-sensitized solar cells. *Chemical Reviews*. 115 (5), 2136–2173, doi: 10.1021/cr400675m (**2015**).

87. Sharma, K., Sharma, V., Sharma, S.S. Dye-Sensitized Solar Cells: Fundamentals and Current Status. *Nanoscale Research Letters*. 13, doi: 10.1186/s11671-018-2760-6 (**2018**).

88. Wang, Y. *et al.* Influence of 4-tert-butylpyridine/guanidinium thiocyanate co-additives on band edge shift and recombination of dye-sensitized solar cells: Experimental and theoretical aspects. *Electrochimica Acta*. 185, 69–75, doi: 10.1016/j.electacta.2015.10.103 (**2015**).

89. Bella, F., Sacco, A., Pugliese, D., Laurenti, M., Bianco, S. Additives and salts for dye-sensitized solar cells electrolytes: What is the best choice? *Journal of Power Sources*. 264, 333–343, doi:

10.1016/j.jpowsour.2014.04.088 (**2014**).

90. Yanagida*, K.J. and S. OPTIMIZATION OF REDOX MEDIATORS AND ELECTROLYTES. 137–164, doi: 10.1201/B16409-9 (**2010**).

91. Gao, J., Prajapati, G.K., Hao, Y., Kloo, L. Exploring Lewis-Base Effects to Improve the Efficiency of [Co(bpy)3]2+/3+-Mediated Dye-Sensitized Solar Cells. *ACS Applied Energy Materials*. doi: 10.1021/acsaem.0c00665 (**2020**).

92. Bella, F., Gerbaldi, C., Barolo, C., Grätzel, M. Aqueous dye-sensitized solar cells. *Chemical Society Reviews*. 44 (11), 3431–3473, doi: 10.1039/c4cs00456f (**2015**).

93. Iftikhar, H., Sonai, G.G., Hashmi, S.G., Nogueira, A.F., Lund, P.D. Progress on Electrolytes Development in Dye-Sensitized Solar Cells. *Materials*. 12 (12), 1998, doi: 10.3390/ma12121998 (**2019**).

94. Tian, H., Sun, L. Iodine-free redox couples for dye-sensitized solar cells. *Journal of Materials Chemistry*. 21 (29), 10592–10601, doi: 10.1039/c1jm10598a (**2011**).

95. Giribabu, L., Bolligarla, R., Panigrahi, M. Recent Advances of Cobalt(II/III) Redox Couples for Dye-Sensitized Solar Cell Applications. *The Chemical Record*. 15 (4), 760–788, doi: 10.1002/tcr.201402098 (**2015**).

96. Cao, Y. *et al.* 11% efficiency solid-state dye-sensitized solar cells with copper(II/I) hole transport materials. *Nature Communications*. 8 (1), 1–8, doi: 10.1038/ncomms15390 (**2017**).

97. Freitag, M. *et al.* High-efficiency dye-sensitized solar cells with molecular copper phenanthroline as solid hole conductor. *Energy and Environmental Science*. 8 (9), 2634–2637, doi: 10.1039/c5ee01204j (**2015**).

98. Feldt, S.M. *et al.* Regeneration and recombination kinetics in cobalt polypyridine based dye-sensitized solar cells, explained using Marcus theory. *Physical Chemistry Chemical Physics*. 15 (19), 7087–7097, doi: 10.1039/c3cp50997d (**2013**).

99. Giribabu, L., Bolligarla, R., Panigrahi, M. Recent Advances of Cobalt(II/III) Redox Couples for Dye-Sensitized Solar Cell Applications. *The Chemical Record*. 15 (4), 760–788, doi: 10.1002/tcr.201402098 (**2015**).

100. Yum, J.H. *et al.* A cobalt complex redox shuttle for dye-sensitized solar cells with high open-circuit potentials. *Nature Communications*. 3 (1), 1–8, doi: 10.1038/ncomms1655 (**2012**).

101. Wu, J. *et al.* Counter electrodes in dye-sensitized solar cells. *Chemical Society Reviews*. 46 (19), 5975–6023, doi: 10.1039/c6cs00752j (**2017**).

102. Thomas, S., Deepak, T.G., Anjusree, G.S., Arun, T.A., Nair, S. V., Nair, A.S. A review on counter electrode materials in dye-sensitized solar cells. *Journal of Materials Chemistry A*. 2 (13), 4474–4490, doi: 10.1039/c3ta13374e (**2014**).

103. Tang, Z., Wu, J., Zheng, M., Huo, J., Lan, Z. A microporous platinum counter electrode used in dye-sensitized solar cells. *Nano Energy*. 2 (5), 622–627, doi: 10.1016/j.nanoen.2013.07.014 (**2013**).

104. Yoon, C.H., R. Vittal, Lee, J., Chae, W.S., Kim, K.J. Enhanced performance of a dye-sensitized solar cell with an electrodeposited-platinum counter electrode. *Electrochimica Acta*. 53 (6), 2890–2896, doi: 10.1016/j.electacta.2007.10.074 (**2008**).

105. Song, M.Y. *et al.* High efficient Pt counter electrode prepared by homogeneous deposition method for dye-sensitized solar cell. *Applied Energy*. 100, 132–137, doi: 10.1016/j.apenergy.2012.06.017 (**2012**).

106. Moraes, R.S., Saito, E., Leite, D.M.G., Massi, M., Da Silva Sobrinho, A.S. Optical, electrical and electrochemical evaluation of sputtered platinum counter electrodes for dye sensitized solar cells. *Applied Surface Science*. 364, 229–234, doi: 10.1016/j.apsusc.2015.12.114 (**2016**).

107. Calogero, G., Calandra, P., Irrera, A., Sinopoli, A., Citro, I., Di Marco., G. A new type of transparent and low cost counter-electrode based on platinum nanoparticles for dye-sensitized solar cells. *Energy &*

Environmental Science. 4 (5), 1838, doi: 10.1039/c0ee00463d (**2011**).

108. Wu, M., Ma, T. Platinum-free catalysts as counter electrodes in dye-sensitized solar cells. *ChemSusChem*. 5 (8), 1343–1357, doi: 10.1002/cssc.201100676 (**2012**).

109. Yun, S., Hagfeldt, A., Ma, T. Pt-free counter electrode for dye-sensitized solar cells with high efficiency. *Advanced materials (Deerfield Beach, Fla.)*. 26 (36), 6210–6237, doi: 10.1002/adma.201402056 (**2014**).

110. Ahn, S.H., Manthiram, A. Edge-Oriented Tungsten Disulfide Catalyst Produced from Mesoporous WO 3 for Highly Efficient Dye-Sensitized Solar Cells. *Advanced Energy Materials*. 6 (3), 1501814, doi: 10.1002/aenm.201501814 (**2016**).

111. Kavan, L., Yum, J.H., Graetzel, M. Optically transparent cathode for Co(III/II) mediated dye-sensitized solar cells based on graphene oxide. *ACS Applied Materials and Interfaces*. 4 (12), 6999–7006, doi: 10.1021/am302253e (**2012**).

112. Tsao, H.N., Burschka, J., Yi, C., Kessler, F., Nazeeruddin, M.K., Grätzel, M. Influence of the interfacial charge-transfer resistance at the counter electrode in dye-sensitized solar cells employing cobalt redox shuttles. *Energy and Environmental Science*. 4 (12), 4921–4924, doi: 10.1039/c1ee02389f (**2011**).

113. Best Research-Cell Efficiency Chart | Photovoltaic Research | NREL. at <https://www.nrel.gov/pv/cell-efficiency.html>.

114. Yella, A. *et al.* Porphyrin-sensitized solar cells with cobalt (II/III)-based redox electrolyte exceed 12 percent efficiency. *Science*. 334 (6056), 629–634, doi: 10.1126/science.1209688 (**2011**).

115. Dang, X. *et al.* Tunable localized surface plasmon-enabled broadband light-harvesting enhancement for high-efficiency panchromatic dye-sensitized solar cells. *Nano Letters*. 13 (2), 637–642, doi: 10.1021/nl3043823 (**2013**).

116. Gangishetty, M.K., Lee, K.E., Scott, R.W.J., Kelly, T.L. Plasmonic enhancement of dye sensitized solar cells in the red-to-near-infrared

region using triangular core-shell Ag@SiO2 nanoparticles. *ACS Applied Materials and Interfaces*. 5 (21), 11044–11051, doi: 10.1021/am403280r (**2013**).

117. Dao, V.D. *et al.* AuNP/graphene nanohybrid prepared by dry plasma reduction as a low-cost counter electrode material for dye-sensitized solar cells. *Electrochimica Acta*. 156, 138–146, doi: 10.1016/j.electacta.2014.12.109 (**2015**).

118. Kim, J.S., Dao, V.D., Larina, L.L., Choi, H.S. Optimum alloying of bimetallic PtAu nanoparticles used as an efficient and robust counter electrode material of dye-sensitized solar cells. *Journal of Alloys and Compounds*. 682, 706–712, doi: 10.1016/j.jallcom.2016.05.030 (**2016**).

119. Mathew, S. *et al.* Dye-sensitized solar cells with 13% efficiency achieved through the molecular engineering of porphyrin sensitizers. *Nature Chemistry*. 6 (3), 242–247, doi: 10.1038/nchem.1861 (**2014**).

120. Yang, J. *et al.* Influence of the donor size in D-π-A organic dyes for dye-sensitized solar cells. *Journal of the American Chemical Society*. 136 (15), 5722–5730, doi: 10.1021/ja500280r (**2014**).

121. Raman, C. V., Krishnan, K.S. A new type of secondary radiation. *Nature*. 121 (3048), 501–502, doi: 10.1038/121501c0 (**1928**).

122. Smith, E., Dent, G. The Theory of Raman Spectroscopy. *Modern Raman Spectroscopy - A Practical Approach*. 71–92, doi: 10.1002/0470011831.ch3 (**2005**).

123. Le Ru, E.C., Etchegoin, P.G. Raman spectroscopy and related optical techniques. *Principles of Surface-Enhanced Raman Spectroscopy*. 29–120, doi: 10.1016/b978-0-444-52779-0.00008-8 (**2009**).

124. Smith, E., Dent, G. Resonance Raman Scattering. *Modern Raman Spectroscopy - A Practical Approach*. 93–112, doi: 10.1002/0470011831.ch4 (**2005**).

125. Aroca, R. Theory of Molecular Vibrations. The Origin of Infrared and

Raman Spectra. *Surface-Enhanced Vibrational Spectroscopy*. 1–33, doi: 10.1002/9780470035641.ch1 (**2007**).

126. Fleischmann, M., Hendra, P.J., McQuillan, A.J. Raman spectra of pyridine adsorbed at a silver electrode. *Chemical Physics Letters*. 26 (2), 163–166, doi: 10.1016/0009-2614(74)85388-1 (**1974**).

127. Jeanmaire, D.L., Van Duyne, R.P. Surface raman spectroelectrochemistry. Part I. Heterocyclic, aromatic, and aliphatic amines adsorbed on the anodized silver electrode. *Journal of Electroanalytical Chemistry*. 84 (1), 1–20, doi: 10.1016/S0022-0728(77)80224-6 (**1977**).

128. Albrecht, M.G., Creighton, J.A. Anomalously Intense Raman Spectra of Pyridine at a Silver Electrode. *Journal of the American Chemical Society*. 99 (15), 5215–5217, doi: 10.1021/ja00457a071 (**1977**).

129. Schatz, G.C., Young, M.A., Duyne, R.P. Electromagnetic Mechanism of SERS. *Surface-Enhanced Raman Scattering*. 19–45, doi: 10.1007/3-540-33567-6_2 (**2006**).

130. Lee, H.K. *et al.* Designing surface-enhanced Raman scattering (SERS) platforms beyond hotspot engineering: Emerging opportunities in analyte manipulations and hybrid materials. *Chemical Society Reviews*. 48 (3), 731–756, doi: 10.1039/c7cs00786h (**2019**).

131. Schlücker, S. SERS microscopy: Nanoparticle probes and biomedical applications. *ChemPhysChem*. 10 (9–10), 1344–1354, doi: 10.1002/cphc.200900119 (**2009**).

132. Langer, J. *et al.* Present and future of surface-enhanced Raman scattering. *ACS Nano*. 14 (1), 28–117, doi: 10.1021/acsnano.9b04224 (**2020**).

133. Schlücker, S. Surface-enhanced raman spectroscopy: Concepts and chemical applications. *Angewandte Chemie - International Edition*. 53 (19), 4756–4795, doi: 10.1002/anie.201205748 (**2014**).

134. Smith, E., Dent, G. Surface-Enhanced Raman Scattering and Surface-Enhanced Resonance Raman Scattering. *Modern Raman Spectroscopy - A Practical Approach*. 113–133, doi:

10.1002/0470011831.ch5 (**2005**).

135. Aroca, R. Chemical Effects and the SERS Spectrum. *Surface-Enhanced Vibrational Spectroscopy*. 107–132, doi: 10.1002/9780470035641.ch4 (**2007**).

136. Grasseschi, D., Toma, H.E. The SERS effect in coordination chemistry. *Coordination Chemistry Reviews*. 333, 108–131, doi: 10.1016/j.ccr.2016.11.019 (**2017**).

137. Nie, S., Emory, S.R. Probing single molecules and single nanoparticles by surface-enhanced Raman scattering. *Science*. 275 (5303), 1102–1106, doi: 10.1126/science.275.5303.1102 (**1997**).

138. Kneipp, K. *et al.* Single molecule detection using surface-enhanced raman scattering (SERS). *Physical Review Letters*. 78 (9), 1667–1670, doi: 10.1103/PhysRevLett.78.1667 (**1997**).

139. Brolo, A.G., Irish, D.E., Smith, B.D. Applications of surface enhanced Raman scattering to the study of metal-adsorbate interactions. *Journal of Molecular Structure*. 405 (1), 29–44, doi: 10.1016/S0022-2860(96)09426-4 (**1997**).

140. Shiohara, A., Wang, Y., Liz-Marzán, L.M. Recent approaches toward creation of hot spots for SERS detection. *Journal of Photochemistry and Photobiology C: Photochemistry Reviews*. 21, 2–25, doi: 10.1016/j.jphotochemrev.2014.09.001 (**2014**).

141. Tiwari, V.S., Oleg, T., Darbha, G.K., Hardy, W., Singh, J.P., Ray, P.C. Non-resonance SERS effects of silver colloids with different shapes. *Chemical Physics Letters*. 446 (1–3), 77–82, doi: 10.1016/j.cplett.2007.07.106 (**2007**).

142. Lee, C.H., Hankus, M.E., Tian, L., Pellegrino, P.M., Singamaneni, S. Highly sensitive surface enhanced raman scattering substrates based on filter paper loaded with plasmonic nanostructures. *Analytical Chemistry*. 83 (23), 8953–8958, doi: 10.1021/ac2016882 (**2011**).

143. Ling, X. *et al.* Raman enhancement effect on two-dimensional layered

materials: Graphene, h-BN and MoS2. *Nano Letters*. 14 (6), 3033–3040, doi: 10.1021/nl404610c (**2014**).

144. Singha, S.S. *et al.* Au nanoparticles functionalized 3D-MoS2 nanoflower: An efficient SERS matrix for biomolecule sensing. *Biosensors and Bioelectronics*. 119, 10–17, doi: 10.1016/j.bios.2018.07.061 (**2018**).

145. Gu, X., Trujillo, M.J., Olson, J.E., Camden, J.P. SERS Sensors: Recent Developments and a Generalized Classification Scheme Based on the Signal Origin. *Annual Review of Analytical Chemistry*. 11 (1), 147–169, doi: 10.1146/annurev-anchem-061417-125724 (**2018**).

146. Xu, J., Du, J., Jing, C., Zhang, Y., Cui, J. Facile detection of polycyclic aromatic hydrocarbons by a surface-enhanced raman scattering sensor based on the au coffee ring effect. *ACS Applied Materials and Interfaces*. 6 (9), 6891–6897, doi: 10.1021/am500705a (**2014**).

147. Montes-García, V. *et al.* Pillar[5]arene-Based Supramolecular Plasmonic Thin Films for Label-Free, Quantitative and Multiplex SERS Detection. *ACS Applied Materials and Interfaces*. 9 (31), 26372–26382, doi: 10.1021/acsami.7b08297 (**2017**).

148. Lenzi, E., Jimenez De Aberasturi, D., Liz-Marzán, L.M. Surface-Enhanced Raman Scattering Tags for Three-Dimensional Bioimaging and Biomarker Detection. *ACS Sensors*. 4 (5), 1126–1137, doi: 10.1021/acssensors.9b00321 (**2019**).

149. Zengin, A., Tamer, U., Caykara, T. Fabrication of a SERS based aptasensor for detection of ricin B toxin. *Journal of Materials Chemistry B*. 3 (2), 306–315, doi: 10.1039/c4tb00290c (**2015**).

150. Ibañez, F.J., Zamborini, F.P. Chemiresistive Sensing with Chemically Modified Metal and Alloy Nanoparticles. *Small*. 8 (2), 174–202, doi: 10.1002/smll.201002232 (**2012**).

151. Raguse, B., Chow, E., Barton, C.S., Wieczorek, L. Gold nanoparticle chemiresistor sensors: Direct sensing of organics in aqueous electrolyte solution. *Analytical Chemistry*. 79 (19), 7333–7339, doi: 10.1021/ac070887i (**2007**).

152. Franke, M.E., Koplin, T.J., Simon, U. Metal and metal oxide nanoparticles in chemiresistors: Does the nanoscale matter? *Small*. 2 (1), 36–50, doi: 10.1002/smll.200500261 (**2006**).

153. Seong, H.C., Kim, B.S., Frisbie, C.D. Electrical resistance of long conjugated molecular wires. *Science*. 320 (5882), 1482–1486, doi: 10.1126/science.1156538 (**2008**).

154. Ali, H., Khan, E. Bioaccumulation of non-essential hazardous heavy metals and metalloids in freshwater fish. Risk to human health. *Environmental Chemistry Letters*. 16 (3), 903–917, doi: 10.1007/s10311-018-0734-7 (**2018**).

155. Malik, L.A., Bashir, A., Qureashi, A., Pandith, A.H. Detection and removal of heavy metal ions: a review. *Environmental Chemistry Letters*. 17 (4), 1495–1521, doi: 10.1007/s10311-019-00891-z (**2019**).

156. Li, Y.-K., Yang, T., Chen, M.-L., Wang, J.-H. Recent Advances in Nanomaterials for Analysis of Trace Heavy Metals. *Critical Reviews in Analytical Chemistry*. 1–20, doi: 10.1080/10408347.2020.1736505 (**2020**).

157. Holmes, P., James, K.A.F., Levy, L.S. Science of the Total Environment Is low-level environmental mercury exposure of concern to human health ? *Science of the Total Environment, The*. 408 (2), 171–182, doi: 10.1016/j.scitotenv.2009.09.043 (**2009**).

158. Balk, S.J. *et al.* Technical report: Mercury in the environment: Implications for pediatricians. *Pediatrics*. 108 (1), 197–205, doi: 10.1542/peds.108.1.197 (**2001**).

159. US EPA, O. National Primary Drinking Water Regulations. at <https://www.epa.gov/ground-water-and-drinking-water/national-primary-drinking-water-regulations>.

160. Gullace, S., Nastasi, F., Puntoriero, F., Trusso, S., Calogero, G. A platinum-free nanostructured gold counter electrode for DSSCs prepared by pulsed laser ablation. *Applied Surface Science*. 506, 144690, doi: 10.1016/j.apsusc.2019.144690 (**2020**).

161. Calogero, G. *et al.* Electronic and charge transfer properties of bio-inspired flavylium ions for applications in TiO2-based dye-sensitized solar cells. *Photochemical and Photobiological Sciences*. 16 (9), 1400–1414, doi: 10.1039/c7pp00039a (**2017**).

162. Calogero, G., Yum, J.H., Sinopoli, A., Di Marco, G., Grätzel, M., Nazeeruddin, M.K. Anthocyanins and betalains as light-harvesting pigments for dye-sensitized solar cells. *Solar Energy*. 86 (5), 1563–1575, doi: 10.1016/j.solener.2012.02.018 (**2012**).

163. Calogero, G., Calandra, P., Irrera, A., Sinopoli, A., Citro, I., Di Marco, G. A new type of transparent and low cost counter-electrode based on platinum nanoparticles for dye-sensitized solar cells. *Energy and Environmental Science*. 4 (5), 1838–1844, doi: 10.1039/c0ee00463d (**2011**).

164. Otto, K., Oja Acik, I., Krunks, M., Tõnsuaadu, K., Mere, A. Thermal decomposition study of HAuCl4·3H2O and AgNO3 as precursors for plasmonic metal nanoparticles. *Journal of Thermal Analysis and Calorimetry*. 118 (2), 1065–1072, doi: 10.1007/s10973-014-3814-3 (**2014**).

165. Duong, T.-T., Choi, J.-S., Le, A.-T., Yoon, S.-G. Morphology Control of Pt Counter Electrodes Using a Pt Precursor Solution with H 2 PtCl 6 ·xH 2 O for Highly Efficient Dye-Sensitized Solar Cells . *Journal of The Electrochemical Society*. 161 (4), H166–H171, doi: 10.1149/2.020404jes (**2014**).

166. De La Garza, M., López, I., Gómez, I. Synthesis and Deposition of Gold Nanoparticles with Different Morphologies on Glass and ITO Substrate by Ultrasonic Spray Pyrolysis. *Advances in Materials Science and Engineering*. 2013, doi: 10.1155/2013/916908 (**2013**).

167. Chew, C.K.T., Salcianu, C., Bishop, P., Carmalt, C.J., Parkin, I.P. Functional thin film coatings incorporating gold nanoparticles in a transparent conducting fluorine doped tin oxide matrix. *Journal of Materials Chemistry C*. 3 (5), 1118–1125, doi: 10.1039/c4tc02275k (**2015**).

168. Bailini, A., Ossi, P.M., Rivolta, A. Plume propagation through a buffer gas and cluster size prediction. *Applied Surface Science*. 253 (19),

7682–7685, doi: 10.1016/j.apsusc.2007.02.038 (**2007**).

169. Ossi, P.M., Neri, F., Santo, N., Trusso, S. Noble metal nanoparticles produced by nanosecond laser ablation. *Applied Physics A: Materials Science and Processing*. 104 (3), 829–837, doi: 10.1007/s00339-011-6422-0 (**2011**).

170. Spadaro, M.C., Fazio, E., Neri, F., Ossi, P.M., Trusso, S. On the influence of the mass ablated by a laser pulse on thin film morphology and optical properties. *Applied Physics A: Materials Science and Processing*. 117 (1), 137–142, doi: 10.1007/s00339-014-8304-8 (**2014**).

171. Micali, N., Neri, F., Ossi, P.M., Trusso, S. Light scattering enhancement in nanostructured silver film composites. *Journal of Physical Chemistry C*. 117 (7), 3497–3502, doi: 10.1021/jp3125507 (**2013**).

172. Denuault, G., Sosna, M., Williams, K.J. Classical experiments. *Handbook of Electrochemistry*. 431–469, doi: 10.1016/B978-044451958-0.50024-0 (**2007**).

173. Thomas, F.G., Henze, G. *Introduction to Voltammetric Analysis*. *Introduction to Voltammetric Analysis*. doi: 10.1071/9780643101135. CSIRO Publishing. (2019).

174. Bard, A.J., Faulkner, L.R. *Electrochemical methods: Fundamentals and Applications*. at <https://www.wiley.com/en-it/Electrochemical+Methods:+Fundamentals+and+Applications,+2nd+Edition-p-9780471043720>. Wiley-VCH Verlag. New York. (2001).

175. Puntoriero, F., Serroni, S., Nastasi, F., Campagna, S. Redox-Active Metal-Polypyridine Dendrimers as Light-Harvesting Antennae. *Electrochemistry of Functional Supramolecular Systems*. 121–143, doi: 10.1002/9780470583463.ch5 (**2010**).

176. Yang, W., Vlachopoulos, N., Hao, Y., Hagfeldt, A., Boschloo, G. Efficient dye regeneration at low driving force achieved in triphenylamine dye LEG4 and TEMPO redox mediator based dye-sensitized solar cells. *Physical Chemistry Chemical Physics*. 17 (24),

15868–15875, doi: 10.1039/c5cp01880c (**2015**).

177. Kalyanasundaram, K., Grätzel, M. Applications of functionalized transition metal complexes in photonic and optoelectronic devices. *Coordination Chemistry Reviews*. 177 (1), 347–414, doi: 10.1016/s0010-8545(98)00189-1 (**1998**).

178. Feldt, S.M., Wang, G., Boschloo, G., Hagfeldt, A. Effects of driving forces for recombination and regeneration on the photovoltaic performance of dye-sensitized solar cells using cobalt polypyridine redox couples. *Journal of Physical Chemistry C*. 115 (43), 21500–21507, doi: 10.1021/jp2061392 (**2011**).

179. Li, J. *et al.* Efficient dye-sensitized solar cells with [copper(6,6′-dimethyl-2,2′-bipyridine)2]2+/1+ redox shuttle. *RSC Advances*. 7 (8), 4611–4615, doi: 10.1039/c6ra25676g (**2017**).

180. Sapp, S.A., Elliott, C.M., Contado, C., Caramori, S., Bignozzi, C.A. Substituted polypyridine complexes of cobalt(II/III) as efficient electron-transfer mediators in dye-sensitized solar cells. *Journal of the American Chemical Society*. 124 (37), 11215–11222, doi: 10.1021/ja027355y (**2002**).

181. Carli, S. *et al.* Comparative evaluation of catalytic counter electrodes for Co(III)/(II) electron shuttles in regenerative photoelectrochemical cells. *Journal of Physical Chemistry C*. 117 (10), 5142–5153, doi: 10.1021/jp312066n (**2013**).

182. Ye, M., Liu, Q., Iocozzia, J., Hong, X., Liu, X., Lin, Z. Polycomponent Electrocatalysts for I-Mediated Dye-Sensitized Solar Cells. *Counter Electrodes for Dye-sensitized and Perovskite Solar Cells*. 323–348, doi: 10.1002/9783527813636.ch13 (**2018**).

183. Wu, M. *et al.* Economical Pt-free catalysts for counter electrodes of dye-sensitized solar cells. *Journal of the American Chemical Society*. 134 (7), 3419–3428, doi: 10.1021/ja209657v (**2012**).

184. Cameron, P.J., Peter, L.M., Zakeeruddin, S.M., Grätzel, M. Electrochemical studies of the Co(III)/Co(II)(dbbip)2 redox couple as a mediator for dye-sensitized nanocrystalline solar cells. *Coordination Chemistry Reviews*. 248 (13–14), 1447–1453, doi:

10.1016/j.ccr.2004.02.010 (**2004**).

185. Chaitanya, K., Ju, X., Heron, B.M. RSC Advances Can elongation of the p -system in triarylamine derived sensitizers with either benzothiadiazole and / or ortho - fl uorophenyl moieties enrich their. (1), 3978–3998, doi: 10.1039/c4ra09914a (**2015**).

186. Dualeh, A. *et al.* Influence of donor groups of organic D-π-A dyes on open-circuit voltage in solid-state dye-sensitized solar cells. *Journal of Physical Chemistry C*. 116 (1), 1572–1578, doi: 10.1021/jp209691e (**2012**).

187. Grätzel, M. The advent of mesoscopic injection solar cells. *Progress in Photovoltaics: Research and Applications*. 14 (5), 429–442, doi: 10.1002/pip.712 (**2006**).

188. Chandiran, A.K., Zakeeruddin, S.M., Humphry-Baker, R., Nazeeruddin, M.K., Grätzel, M., Sauvage, F. Investigation on the Interface Modification of TiO 2 Surfaces by Functional Co-Adsorbents for High-Efficiency Dye-Sensitized Solar Cells. *ChemPhysChem*. 18 (19), 2724–2731, doi: 10.1002/cphc.201700486 (**2017**).

189. Harms, H.A., Tétreault, N., Gusak, V., Kasemo, B., Grätzel, M. In situ investigation of dye adsorption on TiO 2 films using a quartz crystal microbalance with a dissipation technique. *Physical Chemistry Chemical Physics*. 14 (25), 9037–9040, doi: 10.1039/c2cp41268c (**2012**).

190. Fu, Y., Ng, S.P., Qiu, G., Hung, T.F., Wu, C.M.L., Lee, C.S. A redox-controlled electrolyte for plasmonic enhanced dye-sensitized solar cells. *Nanoscale*. 9 (30), 10940–10947, doi: 10.1039/c7nr03506c (**2017**).

191. Chi, C.F., Su, S.C., Liu, I.P., Lai, C.W., Lee, Y.L. Charge transfer and performance enhancement of dye-sensitized solar cells by utilization of a tandem structure. *Journal of Physical Chemistry C*. 118 (31), 17446–17451, doi: 10.1021/jp504849f (**2014**).

192. Liu, W., Hu, L., Dai, S., Guo, L., Jiang, N., Kou, D. The effect of the series resistance in dye-sensitized solar cells explored by electron

transport and back reaction using electrical and optical modulation techniques. *Electrochimica Acta*. 55 (7), 2338–2343, doi: 10.1016/j.electacta.2009.11.065 (**2010**).

193. Brennan, M.P., Abramase, A.L., Andrews, R.W., Pearce, J.M. Effects of spectral albedo on solar photovoltaic devices. *Solar Energy Materials and Solar Cells*. 124, 111–116, doi: 10.1016/j.solmat.2014.01.046 (**2014**).

194. Russell, T.C.R., Saive, R., Augusto, A., Bowden, S.G., Atwater, H.A. The Influence of Spectral Albedo on Bifacial Solar Cells: A Theoretical and Experimental Study. *IEEE Journal of Photovoltaics*. 7 (6), 1611–1618, doi: 10.1109/JPHOTOV.2017.2756068 (**2017**).

195. Bastús, N.G., Merkoçi, F., Piella, J., Puntes, V. Synthesis of highly monodisperse citrate-stabilized silver nanoparticles of up to 200 nm: Kinetic control and catalytic properties. *Chemistry of Materials*. 26 (9), 2836–2846, doi: 10.1021/cm500316k (**2014**).

196. Agnihotri, S., Mukherji, S., Mukherji, S. Size-controlled silver nanoparticles synthesized over the range 5-100 nm using the same protocol and their antibacterial efficacy. *RSC Advances*. 4 (8), 3974–3983, doi: 10.1039/c3ra44507k (**2014**).

197. Samal, A.K., Polavarapu, L., Rodal-Cedeira, S., Liz-Marzán, L.M., Pérez-Juste, J., Pastoriza-Santos, I. Size tunable Au@Ag core-shell nanoparticles: Synthesis and surface-enhanced raman scattering properties. *Langmuir*. 29 (48), 15076–15082, doi: 10.1021/la403707j (**2013**).

198. Yi, Z. *et al.* Green, effective chemical route for the synthesis of silver nanoplates in tannic acid aqueous solution. *Colloids and Surfaces A: Physicochemical and Engineering Aspects*. 392 (1), 131–136, doi: 10.1016/j.colsurfa.2011.09.045 (**2011**).

199. Rodríguez-Fernández, J., Pérez-Juste, J., García De Abajo, F.J., Liz-Marzán, L.M. Seeded growth of submicron Au colloids with quadrupole plasmon resonance modes. *Langmuir*. 22 (16), 7007–7010, doi: 10.1021/la060990n (**2006**).

200. Rodríguez-Lorenzo, L., De La Rica, R., Álvarez-Puebla, R.A., Liz-

Marzán, L.M., Stevens, M.M. Plasmonic nanosensors with inverse sensitivity by means of enzyme-guided crystal growth. *Nature Materials*. 11 (7), 604–607, doi: 10.1038/nmat3337 (**2012**).

201. Kim, K.Y. *Plasmonics - Principles and Applications*. *Plasmonics - Principles and Applications*. doi: 10.5772/2633. InTech. (2012).

202. Squillaci, M.A., Stoeckel, M.A., Samorì, P. 3D hybrid networks of gold nanoparticles: Mechanoresponsive electrical humidity sensors with on-demand performances. *Nanoscale*. 11 (41), 19319–19326, doi: 10.1039/c9nr05336k (**2019**).

203. Jain, T., Westerlund, F., Johnson, E., Moth-Poulsen, K., Bjørnholm, T. Self-assembled nanogaps via seed-mediated growth of end-to-end linked Gold nanorods. *ACS Nano*. 3 (4), 828–834, doi: 10.1021/nn900066w (**2009**).

204. Alvarez-Puebla, R.A., Dos Santos, D.S., Aroca, R.F. Surface-enhanced Raman scattering for ultrasensitive chemical analysis of 1 and 2-naphthalenethiols. *Analyst*. 129 (12), 1251–1256, doi: 10.1039/b410488a (**2004**).

205. Serrano-Montes, A.B. *et al.* Gold Nanostar-Coated Polystyrene Beads as Multifunctional Nanoprobes for SERS Bioimaging. *Journal of Physical Chemistry C*. 120 (37), 20860–20868, doi: 10.1021/acs.jpcc.6b02282 (**2016**).

206. Stamplecoskie, K.G., Scaiano, J.C., Tiwari, V.S., Anis, H. Optimal size of silver nanoparticles for surface-enhanced raman spectroscopy. *Journal of Physical Chemistry C*. 115 (5), 1403–1409, doi: 10.1021/jp106666t (**2011**).

207. Ren, W., Zhu, C., Wang, E. Enhanced sensitivity of a direct SERS technique for Hg2+ detection based on the investigation of the interaction between silver nanoparticles and mercury ions. *Nanoscale*. 4 (19), 5902–5909, doi: 10.1039/c2nr31410j (**2012**).

208. Sumesh, E., Bootharaju, M.S., Anshup, Pradeep, T. A practical silver nanoparticle-based adsorbent for the removal of Hg2+ from water. *Journal of Hazardous Materials*. 189 (1–2), 450–457, doi:

10.1016/j.jhazmat.2011.02.061 (**2011**).

209. Ivanova, O.S., Zamborini, F.P. Size-dependent electrochemical oxidation of silver nanoparticles. *Journal of the American Chemical Society*. 132 (1), 70–72, doi: 10.1021/ja908780g (**2010**).

210. Henglein, A. Colloidal Silver Nanoparticles: Photochemical Preparation and Interaction with O2, CCl4, and Some Metal Ions. *Chemistry of Materials*. 10 (1), 444–450, doi: 10.1021/cm970613j (**1998**).

211. Zou, L. *et al.* Tannic acid-based adsorbent with superior selectivity for lead(II) capture: Adsorption site and selective mechanism. *Chemical Engineering Journal*. 364, 160–166, doi: 10.1016/j.cej.2019.01.160 (**2019**).

212. Gu, X., Trujillo, M.J., Olson, J.E., Camden, J.P. SERS Sensors: Recent Developments and a Generalized Classification Scheme Based on the Signal Origin. *Annual Review of Analytical Chemistry*. 11 (1), 147–169, doi: 10.1146/annurev-anchem-061417-125724 (**2018**).

6 Acknowledgments

First of all, I would like to express my deepest gratitude to my supervisor, Dr. Giuseppe Calogero, who has welcomed me with joy and enthusiasm in his lab. Working with him, I learnt the value of discussion, since a research work cannot be complete before being deeply discussed with co-workers. Furthermore, I wish to thank him for trusting and supporting me in every decision, letting me always free to express my ideas, both inside and outside the lab.

A word of gratitude must go to my co-tutor, Prof. Paolo Samorì, who gave me the chance to work in his lab as a visiting PhD student. I wish to thank him not only for the great opportunity to work in an international environment, surrounded by colleagues coming from different countries with very different research backgrounds, but also for trusting me and giving me the time to develop my ideas.

I would also like to thank the hosting institutions, the IPCF-CNR in Messina and the ISIS in Strasbourg, as well as the Research & Mobility 2017 project, for funding my research period in France.

It has been an enormous privilege to collaborate with Dr. Sebastiano Trusso, Prof. Francesco Nastasi, Prof. Fausto Puntoriero, Dr. Verónica Montes-García and Dr. Stefano Casalini and I wish to thank them for letting me learn from them and for the long and invaluable discussions.
Very special thanks must go to Prof. Fausto Puntoriero, who has been my guide since almost the beginning of my university journey. I really recognize him as my mentor, the “lighthouse” who is always ready to enlighten my “navigation”.

I cannot avoid mentioning all the present and past colleagues and friends for their help, but also for the great time spent together: Ambra, Antonio, Marco, Nunzio, Dario, Verónica, Nicholas, Luca, Stefano I., Pietro, Stefano C., Rafael, Chang-Bo, Dani, Matilde, Haixin, Enrico, Barbara, Salvatore, Artur, Corinne, Nicolas.

I wish to dedicate this thesis to my sister, who has always been on my side, encouraging me every day. She truly is my source of inspiration, an eclectic person, who is always ready to answer all my questions, but also to gift me lot of laughters.

7 Additional information

Research period abroad

Visiting PhD student at the Université de Strasbourg in the Laboratoire de Nanochimie at the Institut de Science et d'Ingénierie Supramoléculaires (ISIS) under the supervision of Prof. Paolo Samorì in the following periods: 03/04/2019 - 12/08/2019; 10/09/2019 - 20/12/2019; 14/01/2020 - 05/05/2020

Communications

- **Applied Nanotechnology and Nanoscience International Conference (ANNIC2019)** (18-20/11/2019-Paris, France). **Oral presentation**. "Highly sensitive SERS sensor based on Ag nanoparticles for heavy metals detection in water". S. Gullace, G. Calogero, V. Montes García, P. Samorì

- **Chemistry meets light and industry (CIS2019)** (28-30/08/2019-Salerno, Italy). **Oral presentation**. "Characterization of novel nanostructured gold counter electrodes for dye sensitized solar cells". S. Gullace, F. Nastasi, F. Puntoriero, S. Trusso, G. Calogero

- **AIV XXIV Conference** (7-10/05/2019-Giardini Naxos, Italy). **Oral presentation. "**Characterization of novel platinum-free nanostructured gold counter electrode for DSSCs prepared by pulsed laser ablation". S. Gullace, F. Nastasi, F. Puntoriero, S. Trusso and G. Calogero

- **Materials2018 Conference** (22-28/10/2019-Bologna, Italy). **Poster presentation.** "Novel nanostructured gold counter electrodes for DSSCs

prepared by pulsed laser ablation". S. Gullace, F. Nastasi, F. Puntoriero, S. Trusso, G. Calogero

• **Bologna International Summer School on NANOmaterials physics** (18-22/06/2018-Bologna, Italy). **Poster presentation. "**Transparent gold counter electrodes for DSSCs prepared by pulsed laser ablation". S. Gullace, S. Trusso, G. Calogero

• **School on Advanced Materials for Sustainable Energy Technologies (SAMSET18)** (11-15/06/2018-Lecce, Italy). **Poster presentation.** "Will natural dyes save the world?". S. Gullace

Member of committees

- UK-IT Joint Meeting on Photochemistry 2019 (June 24- 26 2019-Lipari, Italy)

Member of the local organizing committee

Prizes

- **Best poster award**. School on Advanced Materials for Sustainable Energy Technologies (SAMSET18)(11-15/06/2018-Lecce, Italy)
- **Best image award.** Scientific art exhibition 2019. 20/11/2019-Strasbourg, France

Publications

Gullace, S., Nastasi, F., Puntoriero, F., Trusso, S., Calogero, G. "A platinum-free nanostructured gold counter electrode for DSSCs prepared by pulsed

laser ablation". *Applied Surface Science*. 506, 144690, doi: 10.1016/j.apsusc.2019.144690 (**2020**).